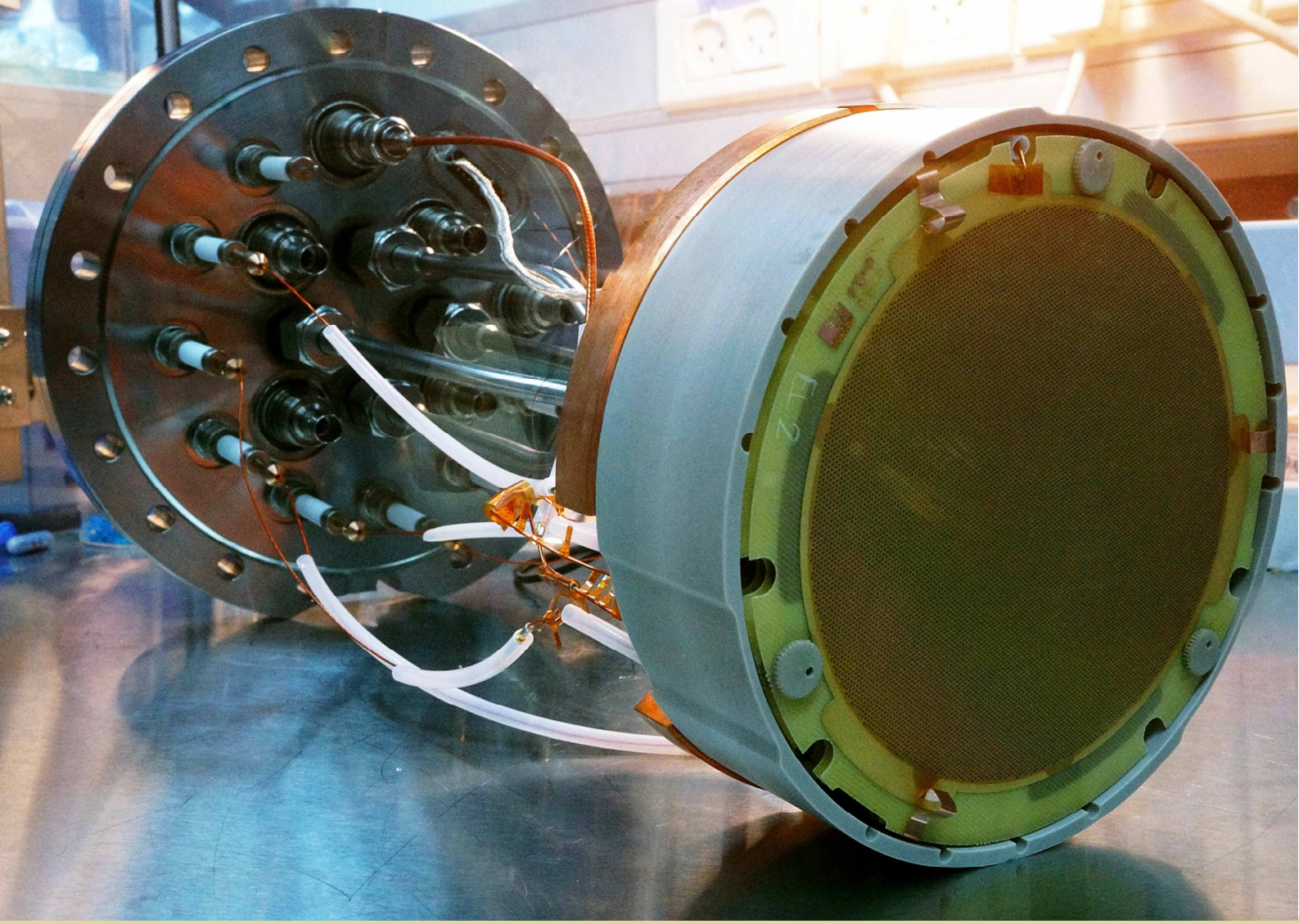

Artur Emanuel Cardoso Coimbra

Research on large area VUV-sensitive gaseous photomultipliers for cryogenic applications

Ph.D. thesis in Physics Engineering, in the field of Instrumentation, done under the scientific supervision of Prof. Dr. Joaquim Marques Ferreira dos Santos and Prof. Amos Breskin and presented to the Physics Department of the Faculty of Sciences and Technology of the University of Coimbra

September 2015

· U C ·

Universidade de Coimbra

Research on large area VUV-sensitive gaseous photomultipliers for cryogenic applications

Scientific Supervisor: Prof. Dr. Joaquim Marques Ferreira dos Santos

Scientific Co-Supervisor: Prof. Amos Breskin

A Thesis Presented for

The Doctor of Philosophy in Physics Engineering

Faculty of Sciences and Technology

University of Coimbra

Artur Emanuel Cardoso Coimbra

September 2015

Artur Emanuel Cardoso Coimbra

Research on large area VUV-sensitive gaseous photomultipliers for cryogenic applications

Dissertação de Doutoramento em Engenharia Física, especialidade de Instrumentação, orientada por Professor Doutor Joaquim Marques Ferreira dos Santos e Professor Amos Breskin e submetida à Faculdade de Ciências e Tecnologia da Universidade de Coimbra

FCTUC FACULDADE DE CIÊNCIAS E TECNOLOGIA
UNIVERSIDADE DE COIMBRA

2015

À minha família

À Lara

Acknowledgements

First and foremost, I would like to thank my supervisor Prof. Dr. Joaquim Marques Ferreira dos Santos for his encouragement and confidence, guidance and valuable input during all the stages that lead to the conclusion of this successful step. I am especially thankful for the opportunity provided to me for developing in so many levels. I am also deeply grateful to my co-supervisor Prof. Amos Breskin, who hosted me in his group for extended periods. The various discussions provided me with the chance to learn from his unmatched experimental knowledge and his deep theoretical grasp. His positive and straightforward leadership, patience and support in difficult moments provided me with an invaluable reference point.

I would like to thank Dr. Lior Arazi for all the productive discussions, patience and time shared in the laboratory and out of it, for his deep theoretical insight, and determined experimental drive; to Dr. David Varstky for his unmatched experience with electronics and phototubes and his willingness to discuss and explain the several subtleties related to them; to Sergei Shchemelinin for all his assistance in the effort put into the production and characterization of the photocathodes and all the lengthy discussions which solved the several “mysteries” related to them; to Michael Rappaport for his valuable suggestions and advices, rooted in his textbook experience, in many occasions and his friendliness; to Benny Pasmantirer for his impressive design work on the cryogenic system and GPM and his availability to share his experience in design software; to Moshe Klin and Yehuda for their willingness to share their year longs experience in the laboratory and patience and dedication in the workshop.

I would also like extend a warm thank you to my colleagues in Coimbra–GIAN, Dr. Fernando Amaro, Dr. Elisabete Freitas, Dr. Cristina Monteiro, Dr. Catalin Balan for all of their support and for giving a helpful hand when needed; and also to my colleagues in the Radiation Laboratory in WIS, M.Sc. Itamar Israelashvili, M.Sc. Eran Erdal, M.Sc. Luca Moleri, M.Sc. Adam Rubin, M.Sc. Michael Pitt for their valuable skills and for taking their time to transmit their knowledge. I would especially like to thank Dr. Hugo Natal da Luz, Dr. Carlos Azevedo and Dr. Marco Cortesi for, in the beginning, sharing their knowledge and providing helpful and motivational presence and discussions.

To everyone that helped me make this thesis come into being in one way or another I would like to give a heartfelt praise. To my friends, Miguel Pedro, Praxe, Gráçio, Ultrix, Capelas, Sobral, Zé, Nuno e Liliana, António, Pedro, Cristiana, Roberta, Ana Sofia, Martina, David Custódio, Ana, Andrêa, Marcos.

My most grateful acknowledgement goes to my family; to Chiara for supporting me in her own way, to my parents, Aurélio and Alice, for providing the backbone over which everything else rests, and to my aunts Emilia and Albino; and to Lara who brought a new and precious beacon guiding our lifes.

Abstract

Liquid noble gases are known to be excellent detection media due their characteristics of high density, high homogeneity and high scintillation yield. They provide both ionization and scintillation signals when transversed by ionizing particles and efficient background suppression due to self-shielding. They are transparent to their own scintillation light and allow expansion to large detector masses. Current noble liquid detectors employ either liquid argon or liquid xenon, in single-phase (liquid only) or double-phase (liquid and gas) configurations and the present application ranges from detection of rare scattering events like Dark Matter search or neutrino physics, to medical imaging like in gamma detectors for PET and LXe Compton Telescope for "3-γ imaging" in combination with PET, gamma/neutron imaging detectors for radionuclide security inspections and Compton Cameras for applications in astrophysics. Both configurations rely on measuring the scintillation light emitted from the liquid-phase or from the liquid and gas-phases with costly large arrays of vacuum photomultipliers.

This Ph.D. thesis is dedicated to the large-area cryogenic gas-avalanche photomultipliers (GPMs) prototypes developed within the Ph.D. program, envisioning their application as a complimentary scintillation detection method for current and future large scale experiments. The research and development efforts aimed for a potentially economic and efficient large-area GPM based on Thick Gas-Electron Multipliers – THGEMs – combining a high efficiency photocathode with a high-gain gas-avalanche electron multiplier, providing high single-photon sensitivity and the possibility for localization of the photons with sub-mm spatial resolution and few-ns temporal resolution. Unlike current vacuum devices, photon localization over large

areas can be made in a single device, using integrated electronics developed for particle tracking. The GPM consists on a cascade of THGEMs combined with a cesium iodide UV-photocathode and the cryogenic tests were performed coupling it to a double-phase liquid xenon detector (a Time Projection Chamber; TPC), in the recently developed Weizmann Institute Liquid Xenon – WILiX – cryogenic system.

Moreover, for the successful use of a cesium iodide photocathode, techniques for the production, characterization and transportation were developed and implemented which allowed systematically reproducing photocathodes whose quantum efficiency ranged from 24% to 30% for a wavelength of 175 nm, corresponding to the liquid xenon scintillation light, and assembling them to the GPM successfully.

Within the Ph.D. thesis it is shown that the maximum gain obtained at 0.7 bar and 180 K was ~8×10^5 for Ne/CH_4(5%) and ~3×10^5 for Ne/CH_4(20%), for single-photons. With Ne/CH_4(5%) at a gain of 1×10^5 and alpha particle-induced S2 signals at a rate of 40 Hz, the discharge probability was found to be of the order of 10^{-6}. Over a period of two months, operating in sealed mode at 0.7bar of Ne/CH_4(20%) at a temperature of ~190 K, gain measurements were consistent within 7–15%, showing no significant change both for the UV–lamp induced signals and alpha-induced S1 signals, indicating that there were no significant changes in either the gas composition or the CsI quantum efficiency. In terms of the time resolution of the GPM – defined as the temporal spread, or jitter, of the GPM response pulse to a scintillation signal – it was found that for scintillation signals producing ~170 – 200 photoelectrons the resolution was on the nanosecond scale, approaching ~1.2 – 1.3 ns at a gain of 3×10^5.

For position sensitive capability the GPM was equipped with position sensitive anodes. Their design was preceded by extensive and CPU–time intensive GEANT4 simulations and analysis that provided valuable information on the expected spatial resolution for different conditions. For the selected pixel size and geometry one can

expect a position resolution of ~5 mm for scintillation signals due to 10 electrons in a double–phase LXe TPC. The tests performed with a second GPM showed that for ~1.3×10^5 initial photoelectrons the calculated centers–of–gravity are in very good agreement (sub-millimeter) to the actual UV source positions.

Furthermore, following the promising studies performed in Coimbra with Gas Electron Multipliers with a micro-induction gap amplifying structure – GEM–MIGAS – an analogous configuration consisting of a THGEM coupled to a submillimetric induction gap was investigated to eventually obtain a GPM configuration capable of reaching higher gains with lower biasing voltages. The investigation combined extensive simulation work showing an interdependence of hole/induction region electric fields while experimental results showed that Ne-CH_4 mixtures, having a more effective UV quenching than Ne-CF_4 mixtures, allowed achieving higher charge gains in stable operating conditions.

Helium based mixtures were also tested in terms of charge–gain and photoelectron extraction efficiency, since they can present a good alternative to Ne-based mixtures for the potential higher gains, with lower applied voltages, similar photoelectron extraction efficiency and lower costs. A Single-THGEM detector was operated in He/CF_4 and He/CH_4 mixtures reaching effective charge-gains well above 10^5, measured in current mode, applying relatively low voltages, when compared to Ar mixtures.

Keywords: Radiation detectors, photon detectors, gas electron multipliers, MPGD, THGEM

Sumário

Desde cedo que a comunidade científica compreendeu que gases nobres em liquido são excelentes meios de detecção de radiação, combinando a sua elevada densidade, elevado grau de homogeneidade e de elevado rendimento de cintilação. Para além destas características inerentes, estes têm a potencialidade de fornecer ambos sinais de ionização – criando electrões livres – e cintilação em resposta à interacção com radiação ionizante e, tendo em vista a sua aplicação em experiências de eventos raros relacionados com física de neutrinos ou matéria–escura, a capacidade de autoblindagem garante a exclusão de eventos induzidos por radiação de fundo. O facto de não absorverem a sua própria luz, emergente dos eventos de cintilação, permite a expansão deste tipo de detectores até grandes volumes, sendo que as colaborações mais recentes propõem detectores com dezenas de toneladas de xénon em estado liquido.

As experiências actuais que usam gases nobres em estado líquido empregam xénon ou árgon numa só fase (estado líquido) ou em dupla-fase (estado líquido + gasoso) e as suas aplicações abrangem desde as já referidas experiências de procura de eventos raros, passando por imagiologia médica tais como detectores de radiação gama para PET ou câmaras Compton “3- γ” em combinação com PET, passando também por aplicações de segurança como sistemas de inspecção para detecção de material físsil e, finalmente, em câmaras Compton para aplicações de astrofísica. Em ambas as configurações a leitura dos sinais de cintilação é geralmente feita através de um grande número de dispendiosos fotomultiplicadores de vácuo agrupados.

A presente tese de doutoramento é dedicada aos fotomultiplicadores gasosos de grande área para aplicações criogénicas desenvolvidos no contexto do programa

doutoral, tendo em vista a sua eventual aplicação como um dispositivo complementar aos métodos existentes de detecção de cintilação, para aplicação em futuras experiências de grande escala. Esta pesquisa foi direccionada tendo em vista o desenvolvimento de eficientes fotomultiplicadores gasosos de grande área, potencialmente mais económicos por unidade de área, baseados em "Thick Gas-Electron Multipliers" (THGEMs). Combinando fotocátodos de alta eficiência com multiplicadores gasosos de electrões capazes de atingir elevado ganho em carga obteve-se assim um dispositivo com elevada sensibilidade para a detecção de fotões únicos, com a possibilidade de discriminação em posição com resolução espacial inferior a um milímetro e com resolução temporal da ordem de poucos nano segundos. Contrariamente ao que sucede com a tecnologia de vácuo actualmente, com este dispositivo a localização em posição de fotões em grandes áreas é feita num único dispositivo integrando electrónica habitualmente utilizada em experiências de rastreamento de partículas. Neste trabalho o fotomultiplicador gasoso desenvolvido consiste numa cadeia de THGEMs combinados com um fotocátodo de iodeto de césio (CsI) sensível ao ultravioleta enquanto que os testes criogénicos foram realizados na Time Projection Chamber (TPC) de dupla fase de xénon líquido recentemente desenvolvida no Weizmann Institute of Science (WILiX).

Relativamente ao GPM desenvolvido foram medidos ganhos máximos em carga de ~8×10^5 em misturas de Ne/CH_4(5%) e de ~3×10^5 em misturas de Ne/CH_4(20%), a uma pressão de 0.7 bar à temperatura de ~180 K, para fotões únicos. Foi obtida uma probabilidade de descarga com uma mistura de Ne/CH_4(5%) a um ganho em carga de 1×10^5 e com sinais de cintilação secundária S2, induzidos por partículas alfa, a uma taxa de 40 Hz de cerca 10^{-6}. Foram medidos desvios no ganho em carga de cerca de 7–15% durante um período de dois meses, operando em modo selado com 0.7 bar de Ne/CH_4(20%) a uma temperatura de ~190 K, não se registando mudanças significativas tanto para fotões únicos induzidos por uma lâmpada UV como para sinais de cintilação

primária S1 induzidos por partículas alfa, indicando a estabilidade da mistura em modo selado assim como para a estabilidade da eficiência quântica do fotocátodo de iodeto de césio. Para além disso foi obtido um valor de 1.2 – 1.3 ns para a resolução temporal do GPM em resposta a sinais de cintilação, induzindo cerca de 170–200 fotoelectrões iniciais no GPM.

Para a leitura em posição de eventos o GPM foi equipado com um ânodo segmentado em "pads" individuais, cujo desenho foi precedido por extensas simulações em GEANT4 que forneceram dados importantes para a optimização da geometria dos ânodos e qual a resolução espacial esperada para diferentes configurações. Das simulações pôde-se determinar que a resolução espacial esperada do GPM será ~5 mm para sinais de cintilação devido a 10 electrões numa TPC de xénon liquido de dupla fase. Nos testes realizados determinou-se que para ~1.3×10^5 fotoelectrões iniciais a posição calculada apresenta um desvio menor que um milímetro da posição real.

Os estudos iniciados em Coimbra combinando multiplicadores gasosos de electrões com regiões de indução micrométricas (GEM–MIGAS) fomentaram o desenvolvimento de um análogo com THGEMs e regiões de indução sub–milimétricas. Estes estudos envolveram simulações electrostáticas de forma a compreender a relação entre os campos eléctricos no interior de THGEMs e da região de indução enquanto que o trabalho experimental demonstrou que com misturas de Ne-CH_4, sendo mais eficientes em absorver a radiação UV das avalanches, permitem atingir ganhos mais elevados em condições estáveis.

Foram também testadas misturas à base de hélio uma vez que podem potencialmente apresentar uma boa alternativa para misturas à base de néon, devido ao ganho em carga elevado, aplicando tensões de operação mais reduzidas, semelhante eficiência de extracção de fotoelectrões e custos mais reduzidos. Em modo de corrente, um detector com um estágio apresentou ganhos superiores a 10^5.

Table of contents

List of figures

List of tables

List of abbreviations

MPGD – Micropattern Gaseous Detector

THGEM – Thick Gas Electron Multiplier

GPM – Gas Photomultiplier

WILiX – Weizmann Institute Liquid Xenon

CsI – Cesium Iodide

UV – Ultra Violet

VUV – Vacuum Ultra Violet

CERN – Conseil Européen pour la Recherche Nucléaire

PMT – Photomultiplier Tube

CsTe – Cesium Telluride

QE – Quantum Efficiency

SBA – Super Bialkali

UBA – Ultra Bialkali

APD – Avalanche Photodiode

GM–APD – Geiger Mode Avalanche Photodiode

SiPM – Silicon Photomultipler

QuPID – Quartz Photon Intensifying Detector

SiGHT – Silicon Geiger Hybrid Tubes

MWPC – Multi-Wire Proportional Chamber

PPAC – Parallel-Plate Avalanche Chamber

RPC – Resistive-Plate Chamber

GEM – Gas Electron Multiplier

MSHP – Micro-Hole-and-Strip Plate

LXe – Liquid Xenon

ER – Electron Recoil

NR – Nuclear Recoil

IVC – Inner Vacuum Chamber

OVC – Outer Vacuum Chamber

PTR – Pulse Tube Refrigerator

PRT – Platinum Resistance Thermometer

PID – Proportional Integral Derivative

UHV – Ultra High Vacuum

PEEK – Polyether Ether Ketone

CF – ConFlat

WIS – Weizmann Institute of Science

NIST – National Institute of Standards and Technology

OFHC – Oxygen-Free High Thermal Conductivity

PTFE – Polytetrafluoroethylene

BNC – Bayonet Naval Connector

SHV – Safe High Voltage

CNC – Computer Numerical Control

RF – Radio Frequency

MFC – Mass Flow Controller

MCA – Multi Channel Analyzer

NIM – Nuclear Instrumentation Module

TTL – Transistor – Transistor Logic

HV – High Voltage

TPC – Time Projection Chamber

CSP – Charge Sensitive Preamplifier

RMS – Root Mean Square

CFD – Constant Fraction Discriminator

TAC – Time to Amplitude Converter

COG – Center of Gravity

SRS – Scalable Readout System

PCB – Printed Circuit Board

GEM-MIGAS – Gas Electron Multiplier – Micro Induction Gap Amplification Structure

DHCAL – Digital Hadron Calorimeter

ILC – International Linear Collider

SNR – Signal to Noise Ratio

MIP – Minimum Ionizing Particle

RICH – Ring Imaging Cherenkov

Introduction and motivation

The work presented in this thesis encompasses the period from 2012 to June 2015, started in earnest shortly after finishing my MSc degree, to when I was enrolled in the PhD Program in Physics Engineering with specialization in Instrumentation of the Faculty of Sciences and Technology of the University of Coimbra. During this period Professor Doctor Joaquim dos Santos (UC) supervised the progress of my work while I provided regular updates to Professor Amos Breskin (WIS) who hosted my prolonged stays in Weizmann Institute of Science. During this time my research and development efforts were on micropattern gaseous detectors (MPGDs), more specifically the thick gas electron multiplier (THGEM), and their cryogenic applications in gas photomultipliers (GPMs).

The work in this thesis constitutes a novel expansion and deepening of previous technical and theoretical bodies of work of many people within, but not limited to, the gas detector community. In chapter one I give a brief overview of the state of the art and describe existing technologies of photon detectors broadly grouped in three categories namely vacuum, solid-state and gas detectors.

Noble liquids detectors, either in single-phase or more complex dual-phase (liquid/gas) devices are candidate for use in a large variety of detectors used in particle physics, nuclear medicine, astrophysics and for other large-scale rare-event experiments like Dark Matter searches and neutrino physics. Chapter two is dedicated to the characteristics and requirements related to the use of liquid noble gases as detection media. In this chapter the mechanisms of signal generation in liquid xenon – ionization signal and scintillation signal – will be described.

Over the course of my PhD I had the opportunity to learn the techniques and methods of designing, assembling and testing THGEM detectors. I also gained significant knowledge on cryogenics systems, especially on the rigid requirements for their successful implementation and operation which would prove to be essential to avoid the long down-times associated with the cooling and warming up of a large volume cryogenic system when the status of any of the many subsystems unexpectedly change. In chapter three I describe the methods and systems that were developed for the successful implementation of a THGEM-based gas photomultiplier for the detection of liquid xenon scintillation. Firstly I describe the experimental system used for small prototypes used for testing analogous conditions as the ones encountered in low temperatures and the feasibility of different detector configurations and gas mixtures. Secondly, I will elaborate on the cryogenic system developed and assembled in the Weizmann Institute of Science – the WILiX system – and its main features and characteristics which make of it a “playground” for detector development. Finally, the large area THGEM electrodes required a new method of testing their quality before being prepared for installation. I will present a novel optical method combined with nano-ampere current measurements that were applied to each candidate electrode in order to assess its potential.

The use of sensitive photocathodes in our gaseous detectors for photon detection imposed the need of being able to frequently produce, test and assemble each large area photocathode in a dry and inert atmosphere. The substance of choice as a photocathode for our applications is cesium iodide since it combines high efficiency and a relative easiness of fabrication by vacuum evaporation but it is also hygroscopic. In chapter four I will describe the techniques and methods developed that optimized their fabrication and eliminated the need to expose freshly fabricated photocathodes for installation in a gas photomultiplier. Moreover, eliminating the need to transport each photocathode to a

vacuum monochromator was an essential step to assess their quality. A technique was developed that permitted the evaluation of each photocathode in-situ, as evaporated, in the deposition chamber. The methods developed are currently standard procedures being employed and will continue to be used in future experiments making possible the safe handling, testing and assembly of excellent quality photocathodes.

The large area gas photomultiplier developed is presented in detail in the fifth chapter. Firstly I will provide a description of the design and of the constraints taken into account in terms of material selection, future plans for upgrades, and of the assembly techniques and discuss the preliminary testing and results from the gas photomultiplier at room temperature. Next the cryogenic characterization of the gas photomultiplier is discussed. The successful detection of radiation induced primary and, for the first time, of secondary scintillation in liquid xenon with a CsI GPM is shown and discussed in depth.

For the gas photomultiplier to be competitive with current technology a position sensitive capability was envisioned from the start of the project. In chapter six I will elaborate on the successful materialization of this capability starting from simulations of a large-volume double-phase liquid xenon time projection chamber that provided an order of magnitude for the expected position resolution for different conditions. These simulations, as well as the selected electronics and the detector geometrical constraints, set bounds for the pixel size which were taken into account for the readout I designed. Once the design had been manufactured into the first batch of position sensitive anodes I prepared a prototype for room temperature tests of the readout coupled to the actual electronics that are going to be used in the cryogenic experiment, which was tested successfully with several radioactive sources and gave the first images of alpha particle induced tracks and UV light imaging from a self-discharging UV lamp..

The last chapters are dedicated to new studies which seek alternatives to higher efficiency of detection, greater stability with increased gain and finally to new and cleaner materials from which to manufacture the THGEM electrodes. Firstly, in chapter seven, I explain and show how single-stage THGEM detectors coupled to submillimetric induction gaps provide comparable performance to double-stage detectors with an obvious advantage in terms of material budget, and space, by eliminating the last stage. I will discuss the importance of helium based gas mixtures for micropattern gaseous detectors and its relevance for gas photomultiplier in chapter eight, focusing on the results obtained with small gas photomultiplier prototype. Mixtures of helium with methane were also investigated with the large area electrodes coupled to the position sensitive readout and the CERN electronics to visualize particle tracks. Finally, in chapter nine the long search for alternative materials is briefly discussed. I will show why current materials are less suitable for application in current and future low radioactive background experiments and propose alternatives – from existing high performance materials to pure substances which can be turned into substrates for electrode manufacturing.

Chapter 1 – State of the art

For present day experiments relying on liquid noble-gases as a detection medium there are currently several options of photodetectors. The requirements imposed on such detectors are strict, namely they should operate under cryogenic conditions, withstand pressure differences of several bar, they should have high single–photon detection efficiency for the VUV wavelength associated with the emission spectrum of liquid noble gases and they should be radio–clean, meaning that their inherent radioactivity should be minimized by careful selection of materials, in view of their application in large scale rare-event experiments.

In this chapter some of the latest generation photodetectors in use or under development are described.

1.1 Vacuum photodetectors – Photomultiplier tubes

A photomultiplier tube is a vacuum device consisting of a transparent window coated on the inside with a semi-transparent photocathode, followed by focusing electrodes, several electron multiplication stages (dynodes), and finally a collection anode. A high potential difference is applied between the photocathode and anode, and every intermediate dynode being held at intermediate potentials by a resistor chain. Photons pass through the window and strike the photocathode. If the energy of the incident photon is greater than the photocathode's work function, ϕ^W, an electron will be ejected from the photocathode via the photoelectric effect with a maximum kinetic energy of:

$$E_k = h\nu - \phi^W$$

where h is the Planck constant, ν is the photon frequency.

The photocathode's work function, ϕ^W, can be defined as:

$$\phi^W = h\nu_0$$

where ν_0 corresponds to the minimum frequency required for a photon to eject an electron from the photocathode's surface – a photoelectron. The probability of extracting a photoelectron from the photocathode is designated as quantum efficiency (Q.E.) and varies as a function of the wavelength of the radiation. Most photocathodes are composed by compounds of alkali metals with a low work function. The most important materials used in PMTs are as follows:

- Cesium iodide (CsI) and cesium telluride (CsTe) photocathodes, used exclusively for vacuum ultraviolet detection are not sensitive to wavelengths longer than 200/300 nm, called "solar blind". They have a relatively good chemical stability when compared to other materials, albeit being hygroscopic, and are relatively easy to synthesize and deposit.
- Antimony-Cesium (Sb-Cs) photocathodes have sensitivity from the ultraviolet to the visible range.
- Bialkali photocathodes (Sb-Rb-Cs, Sb-K-Cs) employ two kinds of alkali metals and have a higher sensitivity and lower dark current then Sb-Cs photocathodes.
- Low-Temperature Bialkali photocathodes (LT-Bialkali) were developed to address the poor linearity at cryogenic temperatures. At such low temperatures, the sheet resistance of the photocathode becomes significant, increasing exponentially from 10^8-10^{10} Ω/square, leading to the accumulation of unpaired positive charges as electrons are emitted, thereby distorting the potential between the photocathode and

first dynode and dramatically decreasing its sensitivity at low temperatures [**1**]. A thin aluminum pattern is fabricated under the photocathode to divide a large photocathode into several smaller segments to supply enough current even at low temperature. In this case, sufficient current is supplied at liquid xenon temperature, but not enough at liquid argon temperature (-186 ºC). For use in liquid argon temperatures, a thin platinum underlay is used at the sacrifice of some quantum efficiency [**2**]. Adding trace amounts of bismuth decreased the resistivity, further improving linearity.

- Multialkali (Sb-Na-K-Cs) photocathodes use three or more kinds of alkali metals. They have a wide spectral response ranging from the ultraviolet to the near-infrared.

By improving the crystallinity of the photocathode its quantum efficiency is similarly improved. This lead to a new generation of “super-bialkali (SBA)” and “ultra-bialkali (UBA)” photocathodes with an improvement of QE by a factor of 2 relative to regular bialkali, reaching >30% at liquid xenon scintillation wavelength.

Specialized photomultiplier tubes (PMTs) have since been developed for integration in current cryogenic experiments, namely the Hamamatsu R8520 [**3**], the Hamamatsu R6041, the Hamamatsu R8778 [**4**] and the Hamamatsu R11410 [**5**] some of which are depicted in Figure 1.1.

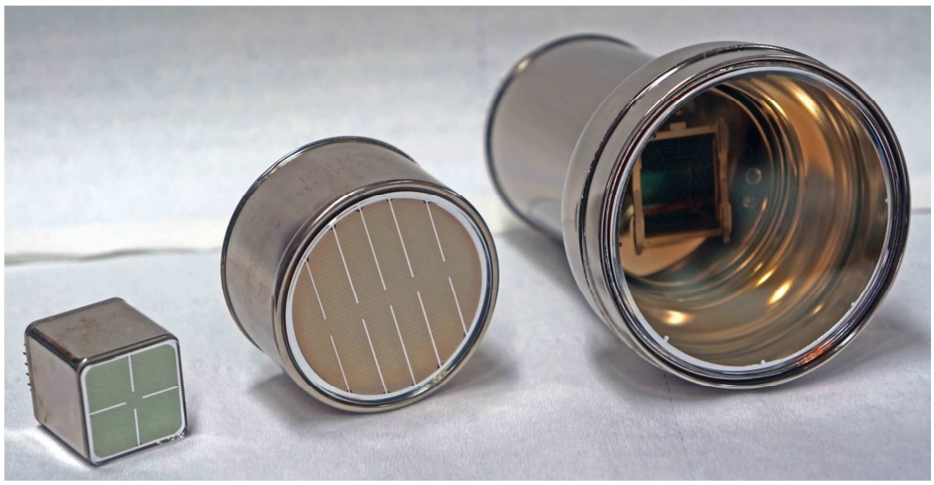

Figure 1.1 – Latest generation cryogenic photomultiplier tubes: R8520, R6041-06 and R11410-20/NG.

These devices are adapted for cryogenic operation and employ a type of bialkali photocathode for VUV-light to photoelectron conversion. The quantum efficiency of these devices usually ranges from 8% to 30% and the latest generation can achieve single photoelectron gains in the order of 10^6.

The price of such devices ranges from roughly 1000€ for the older R6041 to 7000€ for the latest R11410. Considering that around 250 three inch photomultiplier tubes are needed to cover the sensitive volume of the largest experiments, the total cost of the photo sensors alone is estimated to be around 1.7 million euros. In addition to the cost, the "material budget" in terms of mass and volume are also an issue. These factors imply large dead volumes filled with LXe and larger amounts of radioactive material inside of the TPC, close to the sensitive region. These issues are the main motivation for the R&D for alternative solutions for PMTs, as GPMs and solid state photosensors.

1.2 Solid state detectors

1.2.1 Avalanche and geiger-mode photodiodes – APDs and GM-APDs

The avalanche photodiodes, or APD's, as shown in Figure 1.2 [**6**], are monolithic semi-conductor detectors composed of a silicon P-N junction. Equilibrium is established in the junction – the so called depletion region – who is devoid of charge carriers. A reverse bias applied in this region separates the charge carriers (holes and electrons) created by the interaction of photons. With a sufficiently high electric field internal charge amplification is achieved due to ionizing collisions with the crystal lattice of the device. The multiplication in practical APDs is moderate, between 50 and a few hundred. A gain of 10^4 is in principle possible but at values higher than a few hundred, the environment needs to be highly regulated since the gain shows a strong dependence on temperature and bias voltage (a specific example is a 3% change in gain per one volt difference in bias supply and -2.2% change in gain per one degree temperature difference both at a nominal gain of 50) [**7**]. For this regime the APD has to be operated extremely close to the breakdown voltage. Moreover, these gains are considered insufficient for single-photon detection.

An advancement on the avalanche photodiodes is the Geiger-mode APD's, or GM–APD's which are characterized by operating them at a voltage slightly (10%–20%) above breakdown voltage. In this operation regime the absorption of a single photon or electron can generate a macroscopic current by triggering an avalanche multiplication where both electrons and holes actively participate in the multiplication process. A constant current then flows through the junction and by adding a high ohmic resistor in

series to the diode this current can be quenched within a few picoseconds after breakdown begins. Due to the nature of the multiplication process any information regarding the primary signal that initiated the breakdown is lost – essentially operating in a binary mode. The gain of these devices is typically in the range of 10^5 to 10^7.

The main drawback of these devices are the small areas currently available for production – the largest device, as of 2010, has an area of 25 mm^2 – this type of device has an important limitation since the areas cannot exceed a few cm^2 due to parasitic capacitance and increase of the dark counting rate. This limitation essentially excludes these devices as an option for large detection areas.

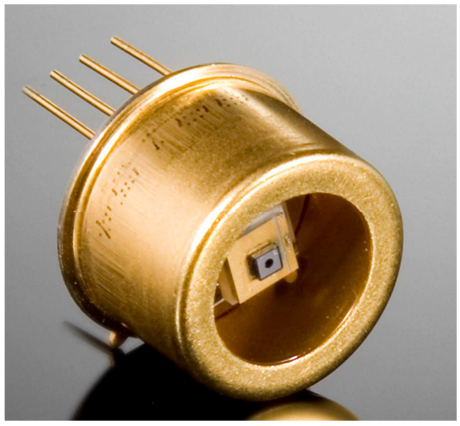

Figure 1.2 – Single module GM-APD.

1.2.2 Silicon photomultipliers – SiPM

The silicon photomultipliers are based on a matrix of densely packed avalanche photodiodes operating in Geiger mode, or in other words a multi-pixel GM-APD. The main drawback of these devices is the dark count rate. Besides single photons or electrons triggering an avalanche, thermally generated electron-hole pairs also contribute to spontaneous signals at a rate of ~10^8 /s*cm^2 at room temperature. Other

sources for dark counts are after-pulses, when trapped carriers during an avalanche are released within hundreds of nanoseconds after initial breakdown triggering further avalanches and optical cross-talk where an initial avalanche releases photons into adjacent sensitive cells triggering neighbor avalanches [**7**]. The typical dark count rate of one of these devices at room temperature is usually stated in ~MHz/mm^2 decreasing four orders of magnitude to about 3 Hz/mm^2 at liquid argon temperature, depending on applied overvoltage. Hence a SiPM array equivalent to a three inch PMT (3000 mm^2) would have a dark rate of about 10 kHz at the liquid argon temperature [**8**]. In Figure 1.3 is shown an advanced SiPM array as used in the previously referenced work.

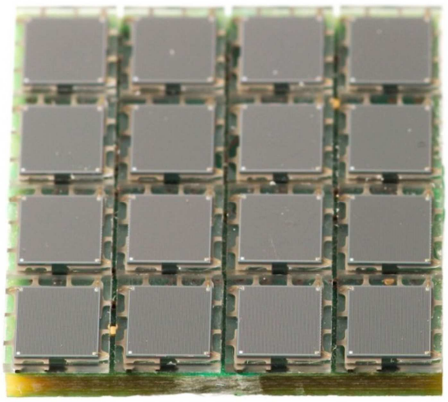

Figure 1.3 – Picture of a 16.6 x 16.6 mm^2 SensL SiPM array (ArrayC-30 035-16P-PCB) as used by S. Catalanotti et al. in liquid argon temperatures.

1.3 Hybrid–photon detectors

1.3.1 Quartz photon intensifying detectors – QuPID

The QUartz Photon Intensifying Detector (QuPID) [**9**] represented in Figure 1.4, is a type of hybrid-photo-detector (HPD) developed by the University of California, Los Angeles (UCLA) and by Hamamatsu Photonics, featuring a Low Temperature Bialkali (LT–Bialkali) photocathode considering the operation under extremely low temperature such as those found in liquid xenon, -108 ºC, an avalanche photodiode (APD) for electron multiplication, and a full quartz body for extremely low radioactivity.

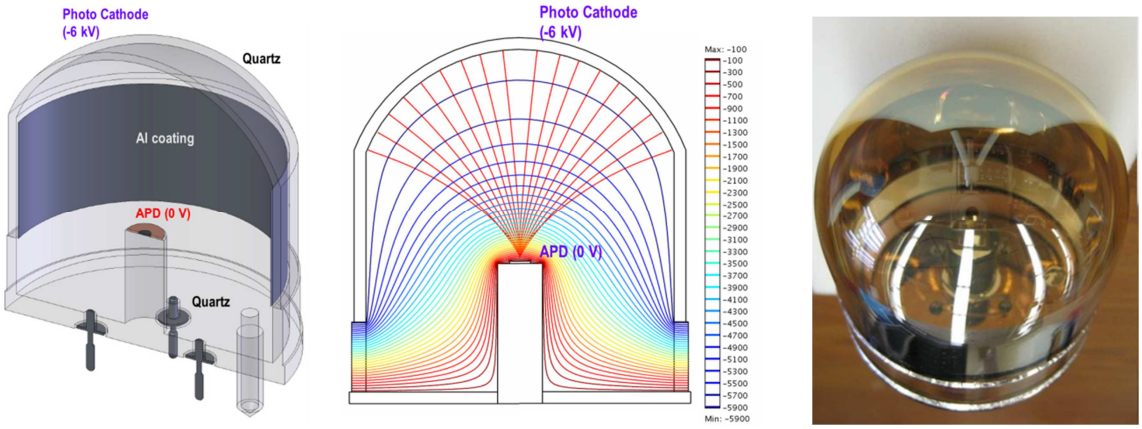

Figure 1.4 – Several views of a QuPID, from left to right: computer generated cross-section; electrical field and equipotential lines; photograph of a QuPID.

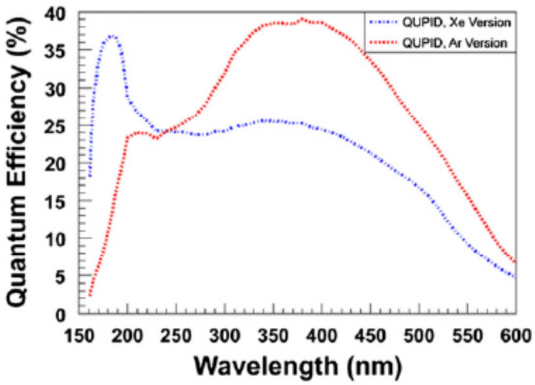

Figure 1.5 – Measured quantum efficiency of QuPIDs optimized for liquid xenon and liquid argon operation.

The QuPID has a semi-spherical window with an inner diameter of 65 mm, coated in the interior with the photocathode, defining the effective photosensitive area. The interior of the device is sealed in vacuum and in its center, supported by a quartz pillar, is located a 3 mm diameter APD receiving electrons from the photocathode. Electrons are emitted from the photocathode and are focused towards the APD by the application of an electric field between the photocathode and APD. The high voltage applied between the photocathode and APD, on the order of 6 kV, accelerates the electrons onto the APD where thousands of electron–hole pairs are created in the depletion layer providing the "electron bombardment gain" of around 700 [**10**]. Furthermore, the application of several hundred volts across the APD triggers the avalanche multiplication of each electron-hole pair providing a further "avalanche gain" of around 200. The total gain of the device is determined by the product of the two types of gain and its maximum value is about 10^5. The quantum efficiency of the LT–Bialkali photocathodes is typically >30%, see Figure 1.5, peaking around 178 nm for the liquid xenon version, while another version optimized for liquid argon peaks at around 400 nm for the wavelength shifted ~125 nm liquid argon scintillation.

The development of the QuPID has been recently stopped by Hamamatsu mainly due to low production yield and limited commercial application. Another important issue is the large amount of indium used for sealing, approximately 9 grams per device, which could have proven to be a limiting factor in terms of low radioactive background experiments, one of the main reasons for the QuPID development.

The termination of the QuPID development triggered a further effort within the hybrid detectors – the Silicon Geiger Hybrid Tubes described next.

1.3.2 Silicon Geiger hybrid tubes – SiGHT

The Silicon Geiger Hybrid Tubes or SiGHT is a recent joint development effort lead by researchers of UCLA in collaboration with researchers from Naples, INFN, and relying on the experience gained by the Detector Development Laboratory in the Weizmann Institute for the production of high quantum efficiency photocathodes.

Significant similarities between the SiGHT and the QuPID devices can be named: the quartz encapsulation, the semi-spherical window, the semi-transparent photocathode. The main element of differentiation is the use of a silicon photomultiplier (SiPM) instead of the avalanche photodiode (APD). By using SiPMs the operating voltage for electron bombardment gain is significantly reduced to ~2 kV. Nevertheless, SiGHT suffers from the same problems as QuPID, when concerning the yield and the vacuum sealing.

1.4 Gaseous Photomultipliers

In gaseous photomultipliers or GPMs employing solid photocathodes, the photoelectrons are emitted from the photocathode into a gas after which they are drifted to an electron multiplier electrode, or a series of cascaded electrodes, where they experience avalanche multiplication due to a high electric field. Unlike the previously described vacuum devices, the GPMs can operate under high magnetic fields [**11**] while operating at atmospheric gas pressure allows constructing large, flat and thin detectors to cover large sensitive areas.

A significant part of the R&D effort on gaseous photomultipliers has been concentrated on the so called “closed geometry” electron multipliers, more specifically the hole-type micro-patterned structures. As opposed to previous generations of electron multipliers relying on multi-wire proportional chambers (MWPCs) [**12**], parallel-plate avalanche chambers (PPACs) [**13**] or resistive-plate chambers (RPCs) [**14**], in which the electron avalanches occur in an “open geometry”, resulting in photon- and ion-mediated secondary avalanches in different regions of the detector limiting gain, efficiency and position discrimination ability [**15**], hole-type electron multipliers, like the GEM [**16**] [**17**], the THGEM [**18**] [**19**], the Micro-Hole-and-Strip Plate (MSHP) [**20**] [**21**] or the hybrid Thick –COBRA [**22**] aim at reducing the photon- and ion–feedback probabilities by screening and confining the multiplication stages. In **Error! Reference source not found.** several electron multiplying structures are represented, along with dimensions: the GEM, the THGEM and the Thick-COBRA, coupled to a solid photocathode for UV photon conversion. Also visible are the multiplication regions: in the case of the GEM and THGEM these occur in the holes while in the TH-COBRA multiplication also occurs between cathode and anode strips.

In Fig.1.7 the principle of operation of a GPM based on GEMs, THGEMs and TH-COBRA is depicted: a reflective photocathode is deposited in the top electrode of the first element of the electron multiplier cascade, the photoelectrons are focused into the holes where charge multiplication occur and the avalanche electrons are drift towards the next multiplier element, being collected in the induction electrode, which can be pixelized for 2D-position readout.

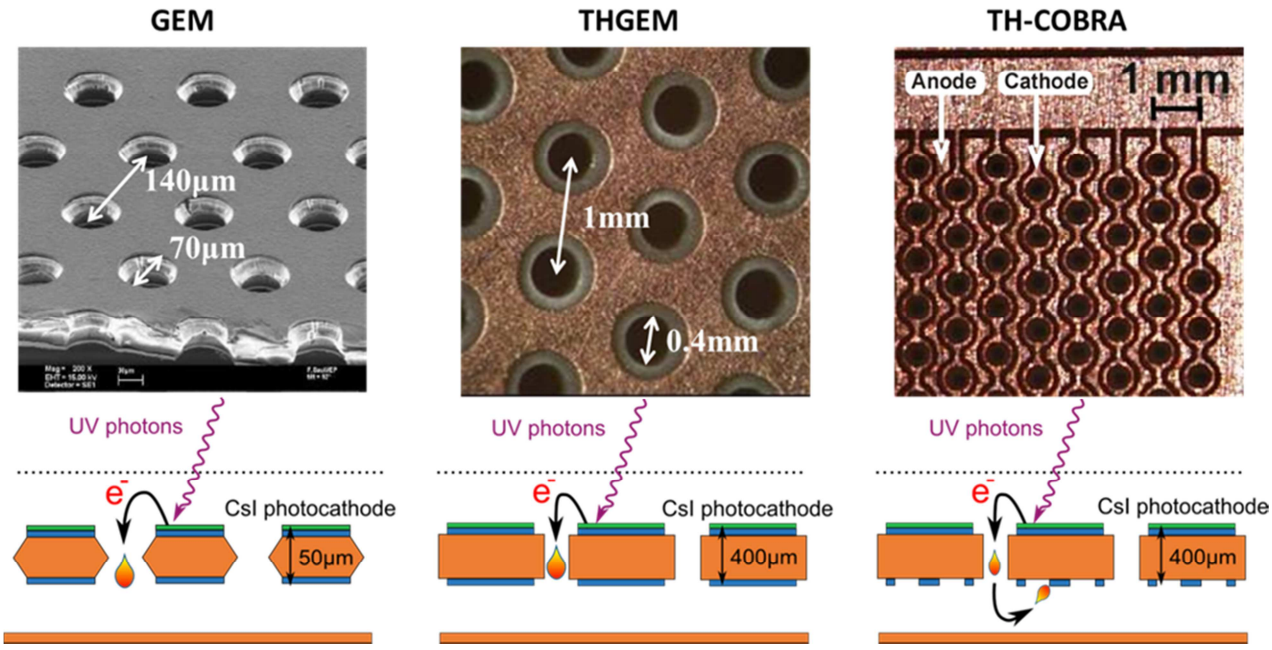

Figure 1.6 – From left to right: representation of the GEM, the THGEM and the TH-COBRA with a CsI photocathode for UV photon conversion. Avalanche regions are visible.

1.4.1 Gas Electron Multipliers

In gas electron multipliers, or GEMs, the charge multiplication occurs within micro etched holes (usually 50 μm in diameter) on a thin double-sided metal-clad insulator (typically 50 μm polyimide), due to a high electric field between both sides of the GEM. Typically these structures are arranged in a stacked configuration where on the first stage is deposited a reflective CsI photocathode and these GPMs can be operated in a single photo-electron sensitivity regime (gains $>10^5$) [**23**], [**15**] and references therein.

1.4.2 Thick Gas Electron Multipliers

The thick gas electron multipliers, or THGEMs, were introduced by Prof. Amos Breskin and are quite similar to the GEMs but with a 10-fold expanded dimensions: they have an hexagonal array of sub-millimeter holes drilled, instead of etched as is the case with GEMs through printed-board-like material double-sided clad in copper, after which a small rim is etched from the copper around each hole to reduce discharge probability. The holes are typically 0.4 mm in diameter and the thickness of the PCB-like material is 0.4 or 0.8 mm. Their operation principle is very much similar to that of the GEMs, in which a high electric potential applied between both faces the electrode creates a strong electric field within the holes, amplifying by electron avalanche multiplication the electrons that are drifted towards them. They are very robust, either electrically and mechanically, due to their enlarged dimensions and can be made in a relatively low-cost way to quite large areas of 1 m by 1 m.

A THGEM-based gas photomultiplier can be employed by coupling a cascade of THGEMs to a solid photocathode and are presently being intensively researched by numerous groups for applications in cryogenic conditions [**24**] [**25**] [**26**] [**27**].

1.4.3 Micro-Hole-and-Strip Plate and Thick-COBRA

Another development introduced by Prof. Veloso and Prof. dos Santos was the Micro-Hole –And-Strip Plate [**20**], or MSHP. It consists of a thin GEM-like hole type electrode with a pattern of thin anode and cathode strips etched on one side. The electrons are drifted towards the holes where they are multiplied by electron impact ionization and they are further multiplied in the vicinity of the anode strips, due to an applied electric bias between the cathode and anode strips. This second multiplication stage in the same element deviates a portion of the avalanche produced ions into the cathode strips, preventing them from flowing back into the solid photocathode.

By combining the MSHP and THGEM concepts, the Thick-COBRA introduced by Dr. Amaro [**22**] aims at merging the advantages of both structures: a robust electron multiplier with ion blocking abilities a two stage multiplication in the same structure.

1.5 Cryogenic gas electron multipliers

In recent years the application of the gas electron multipliers has been intensively studied envisioning their application for the detection of noble-gas liquid scintillation. Current prototypes have been small in size and served so far as a proof of concept that such devices can be applied for liquid argon or liquid xenon scintillation. The works of

A. Bondar et al [**28**] [**24**], S. Duval et al [**29**] [**30**] and W. Xie et al [**26**] represent the most recent experiments with cryogenic GPMs.

Chapter 2 – Liquid xenon as a detection medium

Liquid noble gases are known to be excellent detection media due their characteristics of high density, high homogeneity and high scintillation yield. They are transparent to their own scintillation light, easily expanded to large detector masses and they provide both ionization and scintillation signals when transversed by ionizing particles. Liquid xenon in particular shares with the other liquid noble gases most of these characteristics but coupled to the fact that it presents no long lived isotopes and it has the highest boiling point, make it the one of the preferred detection medium. The main characteristics of the liquid noble gases are shown in table 1. This table is meant to serve as a general guideline only.

One of the main issues associated with the use of liquid xenon as a detector medium is the inevitable cryogenic systems necessary to reach the temperature for its liquefaction, namely 165 K at a pressure of 1atm. Its inherent characteristics as a detection medium clearly make up for the price to pay for the cryogenic systems.

	Z (A)	**BP at 1 atm [K]**	**Liquid Density at BP [g/cm^3]**	**Ionization Yield [electron/keV]**	**Scintillation Yield [photons/keV]**	**Scintillation Wavelength [nm]**
He	2 (4)	4.2	0.13	39	15	
Ne	10 (20)	27.1	1.21	46	74	78 – 85
Ar	18 (40)	87.3	1.4	42	40	125
Kr	36 (84)	119.8	2.41	49	25	145
Xe	54 (131)	165	3.06	64	46	178

Table 1 – Main characteristics of most of the noble gases in their liquid state: atomic number, boiling point at 1atm, liquid density at boiling point, ionization yield, scintillation yield and scintillation wavelength.

It can be seen from Table 1 that liquid xenon has the highest atomic number and density, which gives it a very high stopping power for ionizing particles. It also possesses the highest ionization and scintillation yields of all important noble liquids. It is also an excellent electrical insulator and, in its liquid form, has a band structure analogous to semi-conductors, with a band gap – the energy between the valence band and conduction band – of 9.22 eV, corresponding to its ionization potential [**31**]. When energy is deposited in the medium by interaction with an ionizing particle, the electrons of the valence band will cross the band gap to the conduction band consequently producing a detectable signal. All of these features make this noble liquid a prime candidate for use as a detection medium in a large variety of detectors used in particle physics, nuclear medicine, astrophysics and for the detection of direct interaction with dark matter. In this chapter the mechanisms of signal generation in liquid xenon – ionization signal and excitation signal – will be described.

2.1 Thermodynamic properties of xenon

In Figure 2.1 is shown the phase diagram of xenon. One can see that xenon is in liquid state at a relatively small temperature interval for pressures below 2 bar (~18 ºC, from 180 K to 162 K, at 2 bar and ~4ºC, from 166 K to 162 K, at 1 bar). Higher pressures are not practical since certain safety requirements need to be met in our application – fused silica and quartz windows in the PMTs and for the GPM have a limited mechanical resistance.

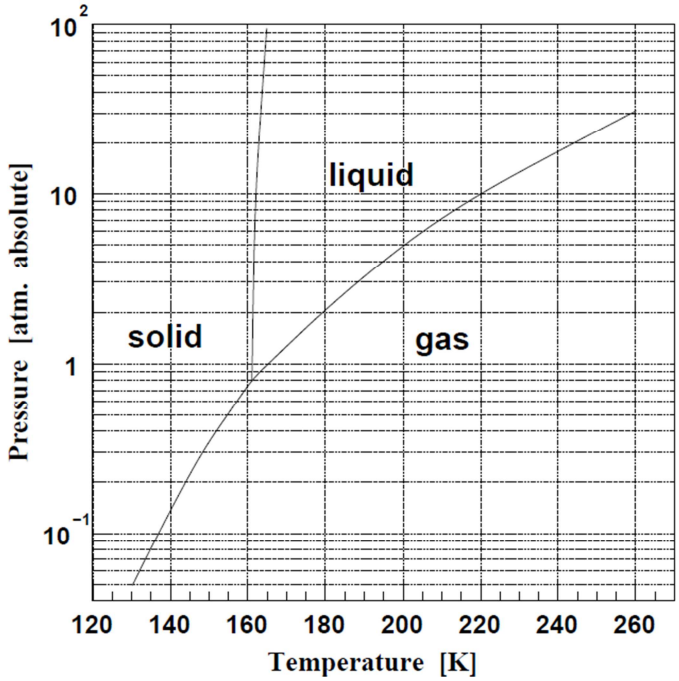

Figure 2.1 – Phase diagram for xenon.

2.2 Interaction modes of radiation with liquid xenon

When a charged particle enters the volume of liquid xenon it interacts with the electrons and nucleus of the xenon atoms via electromagnetic coupling. For incident alpha particles, protons or electrons this translates to an electronic and nuclear stopping power, respectively, and these quantities are represented in Figure 2.2. Also shown the figure is the contribution of the electronic and nuclear stopping power, for alphas and protons, and collisional and radiative stopping power for electrons [**32**]. For high energies and for electrons the nuclear stopping power can be neglected when compared to the electronic stopping power. For incident electrons interactions with the medium resulting in the emission of bremsstrahlung radiation can be important when compared to the electronic stopping power. The incident charged particle will then transfer its energy mainly to the electrons of the xenon atoms inducing two types of interaction: either ionization or excitation of the xenon atoms. In Figure 2.3 is represented the range of alpha particles, protons and electrons, as a function of the energy of the particle, in xenon. The range is rather short especially for alpha particles – considering a ^{241}Am radioactive source emitting 5.5 MeV alphas, like the one that was later used, it can be calculated that their average range in liquid xenon (considering a liquid density of 2.94 g/cm^3) is ~40 μm.

Differently from charged particles, photons like x-rays or gamma-rays interact with matter either by photoelectric effect, by Compton Effect, by pair creation or by Rayleigh effect. The contribution to the overall interaction probability of the photons with the xenon atoms due to each of these mechanisms is strongly dependent on the energy of the photon, as can be seen in Figure 2.4.

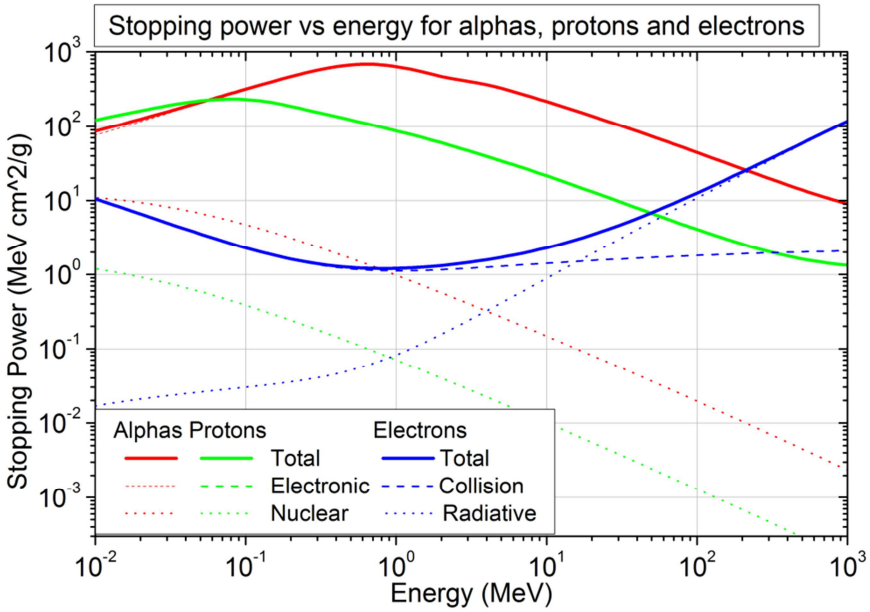

Figure 2.2 – Total stopping power (in MeV.cm^2/g) for alpha particles, protons and electrons in xenon versus energy.

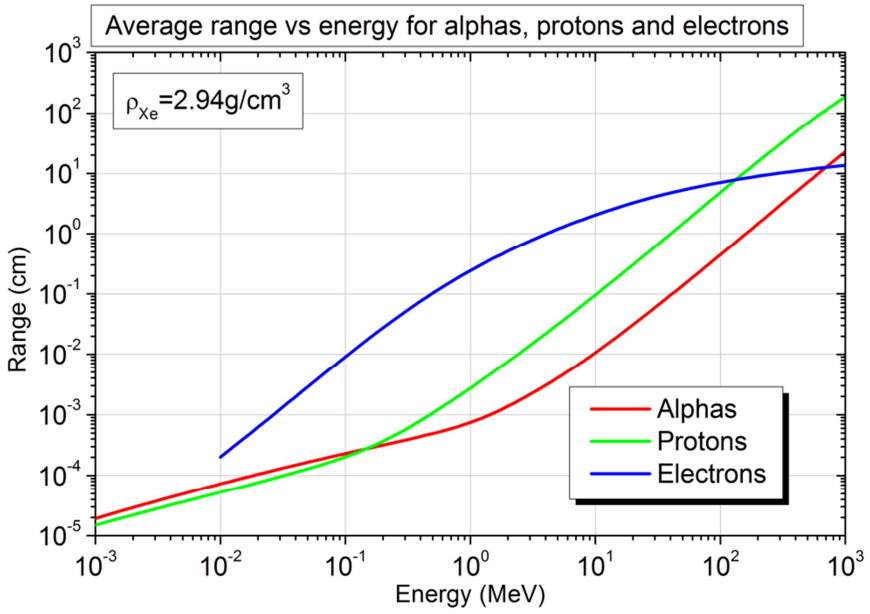

Figure 2.3 –Range (in cm) for alpha particles, protons and electrons in liquid xenon for a liquid density of 2.94 g/cm^3 versus particle energy [**32**].

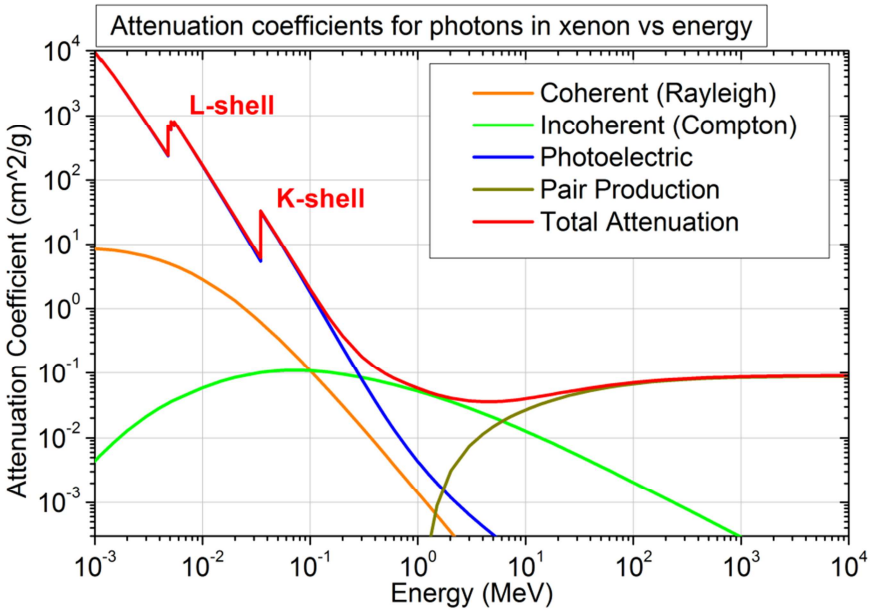

Figure 2.4 – Attenuation coefficients of photons in xenon as a function of the energy for the various interactions mechanisms [**33**].

The photoelectric effect is the total absorption of the incoming photon by an electron of the xenon atom. The result of this interaction is the ejection of an electron from the atom, with a kinetic energy equal to the energy difference between the energy of the incoming photon and the electron bonding energy, leaving the atom ionized. For low photon energies this effect is dominant.

The interaction by Compton Effect is the inelastic, incoherent, scattering between the incident photon and a weakly bound electron of a xenon atom. The electron absorbs a certain amount of energy from the photon and is ejected from the atom. The photon is then scattered in a different angle with a lower energy obeying the following relation:

$$\Delta\lambda = \frac{h}{m_e c}(1 - cos\theta)$$

The interaction by pair or triplet production in xenon is dominant only for energies above ~7 MeV. It involves the creation of an electron–positron pair or an electron–electron–positron triplet in the vicinity of an atomic nucleus or electron, respectively. The energy threshold for pair production is at least twice the electron's rest mass, or 1.022 MeV, while the energy threshold for triplet production is at least four times the electron's rest mass or 2.044 MeV.

In Figure 2.5 is shown the photon mean free path in liquid xenon for a liquid density of 2.94 g/cm^3 corresponding to a temperature of 165 K. As an example, for a photon energy of ~60 keV, corresponding to the main gamma emission of a ^{241}Am radioactive source which will be used for following studies, the attenuation length is ~430 μm.

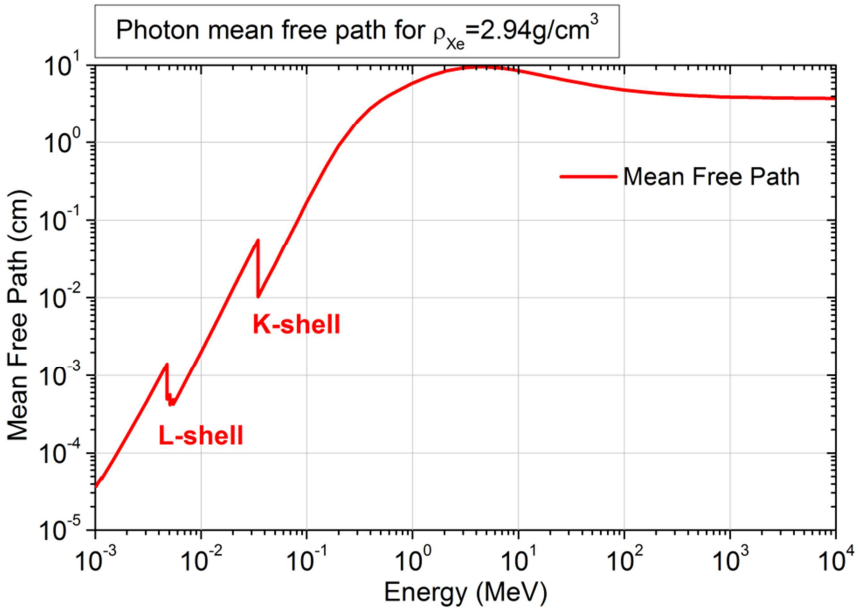

Figure 2.5 – Photon mean free path in liquid xenon for liquid density of 2.94 g/cm^3 as a function of the photon energy.

Lastly, considering the interaction of neutrons with xenon atoms in liquid xenon, we have that in general there are two main modes of interactions of the neutrons with

matter, referring specifically to the interactions of the neutrons with the nucleus of the elements that compose the target and they can be one of two major types: 1) scattering or, 2) absorption.

Neutron scattering (elastic or inelastic) by an atomic nucleus involves the change of speed and direction of the neutron while the nucleus is left with the same number of protons and neutrons – from this interaction the nucleus may recoil and it may be left in an excited state, leading to a later emission of radiation. In elastic scattering the total kinetic energy of the neutron and nucleus is unchanged by the interaction but a fraction of the energy of the neutrons is transferred to the nucleus, in a process named "neutron moderation". This average energy loss of the neutrons is, for a given neutron energy *E*, proportional to:

$$2 * E * A/(A+1)^2$$

where *A* is the targets atomic weight. From this expression it can be inferred that, in general, low mass elements like hydrogen or helium, are more efficient at moderating neutrons. In inelastic scattering the nucleus undergoes an internal rearrangement into an excited state from which it eventually decays releasing radiation. The total kinetic energy of the neutron and nucleus is less than the kinetic energy of the incoming neutron.

On the other hand, instead of being scattered by a nucleus, the neutron may be absorbed or captured. The nucleus will rearrange its internal structure by emitting other particles: one or more gamma rays, protons or alpha particles. The nucleus may also emit excess one, two or three excess neutrons and finally a fission event may occur creating two or more fission fragments and more neutrons [**34**].

In Figure 2.6 the macroscopic neutron cross sections for natural liquid xenon (considering the natural abundances of each of the main xenon isotopes: 1.91% ^{128}Xe,

26.4% ^{129}Xe, 4.07% ^{130}Xe, 21.2% ^{131}Xe, 26.9% ^{132}Xe, 10.4% ^{134}Xe and 8.86% ^{136}Xe) are represented. The neutron energies range from 0 to 20 MeV and for each of the previously described interaction modes, designating them by their specific cross section notation: "n, tot" – total cross section, "n, el" and "n, inl" – elastic and inelastic scattering cross sections, respectively, "n, 2n" and "n, 3n"– cross section for production of two and three neutrons, respectively. Only reactions with a macroscopic cross section larger than 10^{-3}cm^{-1} are represented.

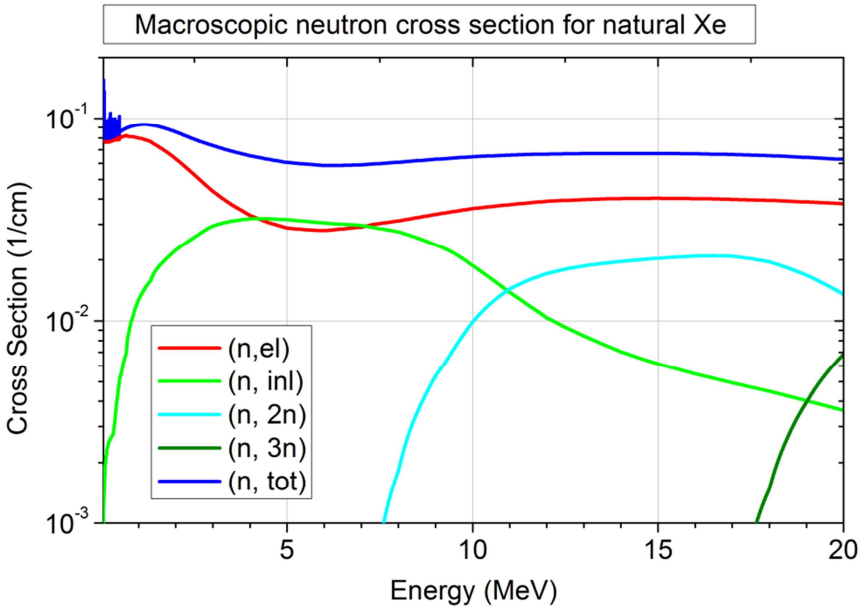

Figure 2.6 – Macroscopic neutron cross sections for natural liquid xenon [**35**]. See text for explanation.

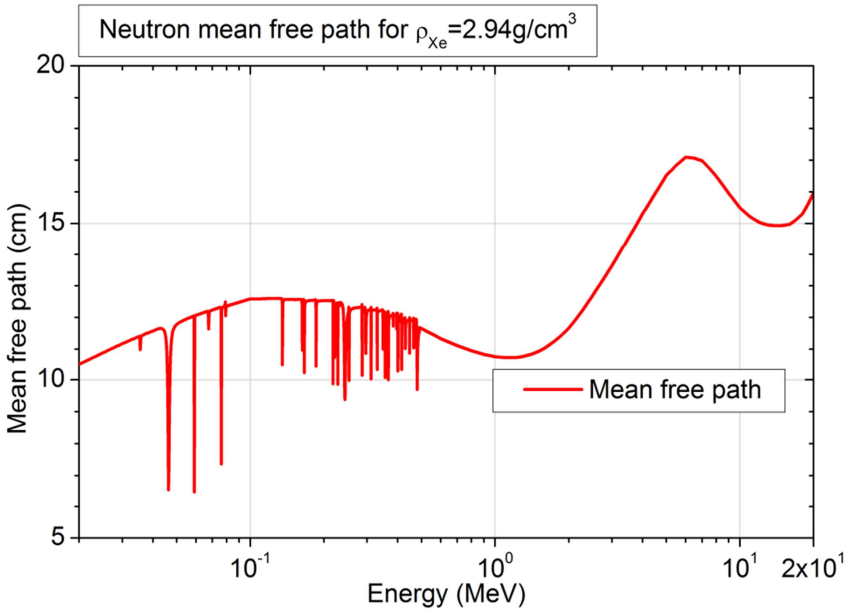

Figure 2.7 – Mean free path of neutrons in liquid xenon versus neutron energy.

In Figure 2.7 the neutron mean free path in liquid xenon, given by the reciprocal of the total macroscopic cross section, as a function of neutron energy, is represented. In order to highlight the neutron resonances at low energies the energy axis is represented in logarithmic scale. Resonances occur at neutron energies with an enhanced cross section for interaction with the nucleus and will occur if the energy of the incident neutron is close to the energy of an excited state of the compound nucleus [**34**].

2.2.1 Ionization and excitation

The average energy required for creating an electron – ion pair in liquid xenon is higher than its ionization potential, I, of 9.22 eV. Considering E_0 as the energy transferred to the xenon by the incident particle and N_i as the average number of electron – ion pairs created, the average energy W required for creation of one such pairs can be defined as:

$$W = \frac{E_0}{N_i}$$

The difference between *W* and *I*, can be explained due to the different modes of energy transfer to the medium, namely an ionization, an excitation and heat transfer mode. For the case of incident electrons this can be expressed by the following expression [**36**]:

$$E_0 = N_i\langle E_i\rangle + N_{ex}\langle E_{ex}\rangle + N_i\langle\varepsilon\rangle$$

where $\langle E_i\rangle$ is the average energy required to ionize an atom, N_i is the average number of ionized atoms, $\langle E_{ex}\rangle$ is the average energy required to excite an atom, N_{ex} is the average number of excited atoms and $\langle\varepsilon\rangle$ is the average energy of sub – excitation, below which the incident electrons interact only through elastic collisions with the atoms, transferring part of their kinetic energy. Combining both previous expressions we have for the average energy required to create an electron – ion pair:

$$W = \langle E_i\rangle + \frac{N_{ex}}{N_i}\langle E_{ex}\rangle + \langle\varepsilon\rangle$$

The value of *W* was determined to be 15.6eV [**37**] [**38**] for LXe. Nevertheless, the actual number of electron – ion pairs created per unit energy deposited in the medium is dependent on the type of ionizing particle and its energy and is different for gaseous and LXe.

2.2.2 Scintillation – recombination and de-excitation

The process of luminescence in liquid xenon due to the passage of radiation involves the formation of diatomic excited molecules formed primarily by two channels.

The first channel is through the excitation of xenon atoms by the primary particle or secondary electrons, forming weakly bound diatomic molecules in the excited state or "excimers":

$$particle + Xe \rightarrow Xe^{*} + e^{-}$$
$$Xe^{*} + Xe\ +\ Xe \rightarrow Xe_2^{*,v}(excimer) +\ Xe$$
$$Xe_2^{*,v} + Xe \rightarrow Xe_2^{*} + Xe$$
$$Xe_2^{*} \rightarrow Xe + Xe + h\nu\ \ (VUV\ emission)$$

The other channel for VUV luminescence is through the ionization of the xenon atoms, induced by the primary particles or secondary electrons, followed by recombination of the positive xenon ions as described by the following equations:

$$particle + Xe \rightarrow Xe^{+} +\ e^{-}$$
$$Xe^{+} + Xe + Xe \rightarrow Xe_2^{+}\ (ionized\ excimer) + Xe$$
$$Xe_2^{+} + e^{-}\ (recombination) \rightarrow Xe^{**} + Xe$$
$$Xe^{**} + Xe \rightarrow Xe^{*} + Xe + heat$$
$$Xe^{*} + Xe\ +\ Xe \rightarrow Xe_2^{*,v}(excimer) +\ Xe$$
$$Xe_2^{*,v} + Xe \rightarrow Xe_2^{*} + Xe$$
$$Xe_2^{*} \rightarrow Xe + Xe + h\nu\ (VUV\ emission)$$

The excimers formed in both processes emit VUV light of the same wavelength. After recombination the formed excimer is left in either one of the $^3\Sigma_u^+$ or $^1\Sigma_u^+$ excited states and the emitted scintillation photons are due to the transitions from one of the two lowest electronic excited states $^3\Sigma_u^+$ or $^1\Sigma_u^+$, to the repulsive ground state $^1\Sigma_g^+$. These two transitions ($^3\Sigma_u^+$ to $^1\Sigma_g^+$ and $^1\Sigma_u^+$ to $^1\Sigma_g^+$) are spectroscopically indistinguishable but their decay times are significantly different as explained in the following section.

The emission spectrum of liquid xenon is centered around λ=178 nm, corresponding to a photon energy of 7eV, with a full-width-half-height (FWHM) value of ±2 nm [**39**] [**40**].

2.2.3 Temporal components of scintillation

The recombination process, with associated photon emission, occurs within few picoseconds after ionization/excitation of the atoms of the liquid. Each of the $^3\Sigma_u^+$ or $^1\Sigma_u^+$ excited states has a different decay time to the ground state, making it possible to distinguish several components of the scintillation events:

- A fast component due to de–excitation of the $^1\Sigma_u^+$ state, with decay time τ_f.
- A slow component due to the de-excitation of the $^3\Sigma_u^+$ state, with decay time τ_s.
- And a component owing to the slower (when compared to the excimer de-excitation times) recombination process, with a time constant of τ_r.

The value taken for the several decay times are summarized in table 2 for incident alpha particles and electrons:

Incident Particle	τ_f (ns)	τ_s (ns)	τ_r (ns)
Electrons (0.5MeV<E<1MeV)	2.2	27	34
Alphas	4.3	22	
Fission fragments	4.3	21	

Table 2 – Summary of scintillation time constants of liquid xenon induced by fast electrons, by alpha particles and by fission fragments. τ_f, τ_s and τ_r are the decay times of the fast, slow and recombination components, respectively.

The direct transition from the ${}^3\Sigma_u^+$ excited state to the ground state is forbidden but becomes possible owing to the spin–orbital coupling with state ${}^1\Pi_u^+$. This leads to rather long decay times of the order the ~20 ns. For the case of incident alpha particles the density of the ionized and excited species along the particle track is much higher than with fast electrons, leading to much faster recombination. Experimentally no ~30 ns recombination component of scintillation has been observed in liquid xenon with alpha particles. In Figure 2.8A we depict the scintillation light decay curves in liquid xenon with an applied electric field and without, explained in the next chapter [**41**], while in Figure 2.8B the scintillation light decay curves in liquid xenon induced by electrons (●), alpha particles (▲) and fission fragments (■) is shown [**42**]. It is evident the strong dependence of the decay of the scintillation light with the type of particle imping on the liquid xenon, making it possible to discriminate the particle type by pulse shape analysis.

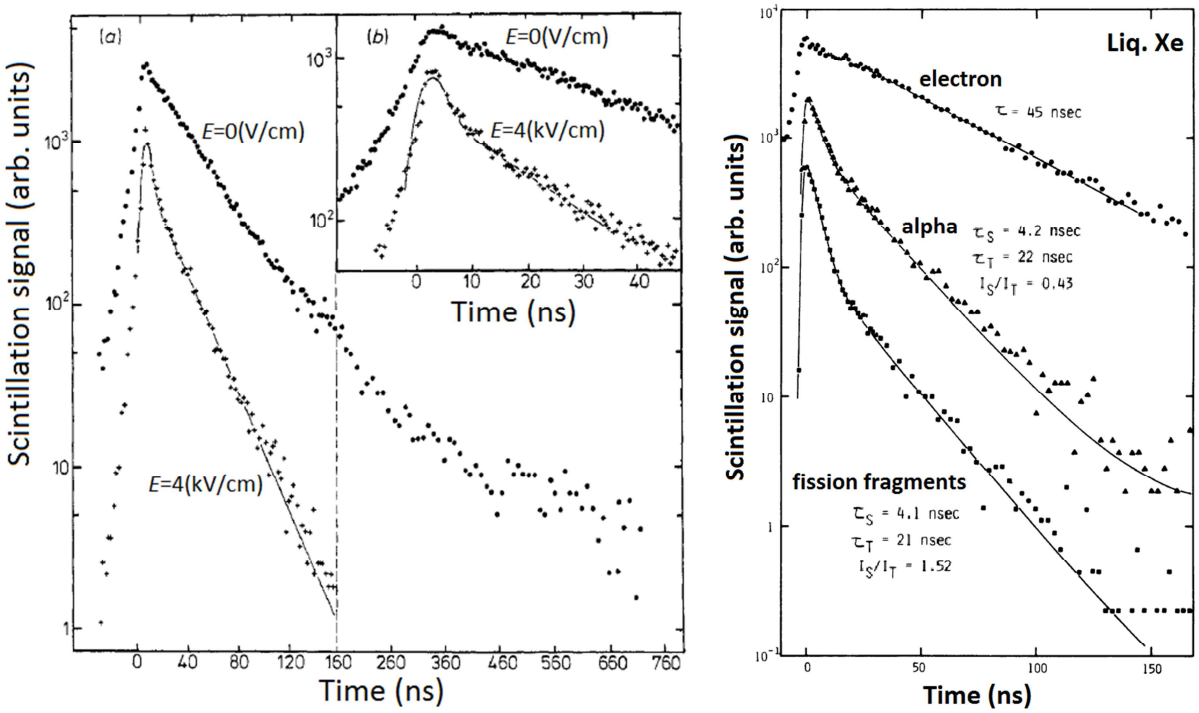

Figure 2.8 – Liquid xenon scintillation light decay curves induced by electrons A) with and without applied electric field and B) by electrons, alpha particles and fission fragments, without applied electric field.

2.2.4 Scintillation and ionization yield

Several effects change the production characteristics and amount of scintillation photons created by the interaction of ionizing radiation with the xenon atoms. Effectively, as it was previously shown, see Figure 2.8, different types of radiation yield a dramatically different number of photons. Moreover, it is known that the application of an electric field changes the scintillation and ionization yields for LXe. In Figure 2.9 is shown the scintillation and ionization yield of liquid xenon induced by alpha particles (5.5 MeV

from ^{241}Am)., electron recoils (122 keV gamma rays from ^{57}Co) and nuclear recoils (56.5 keV) versus the applied electric field [**43**].

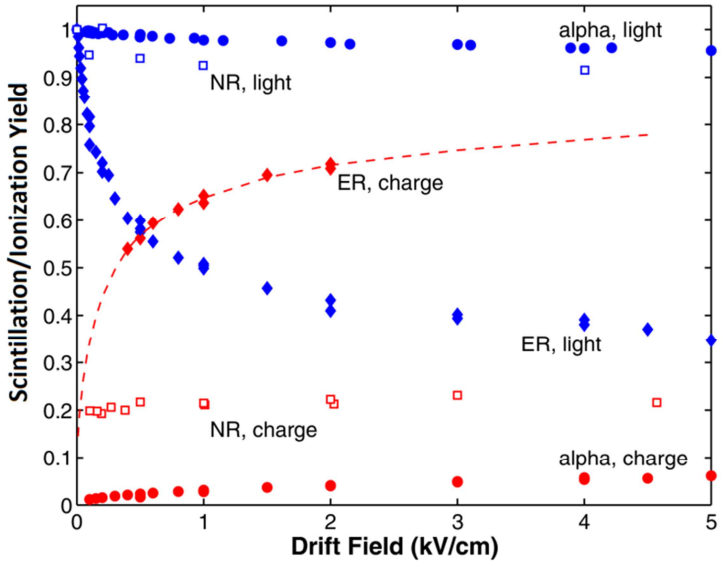

Figure 2.9 – Variation of the scintillation and ionization yields versus the applied electric field in LXe, for 122 keV electron recoils (ER), 56.5 keV nuclear recoils (NR) and 5.5 MeV alphas.

Scintillation yield and ionization yield are denoted as “light” and “charge” in the figure. For a given particle type it is shown that the scintillation and ionization yields are anti-correlated with the field. This effect is clearly distinct when comparing the case for alpha particles and electron recoils – the charge and light products for electron recoils are much strongly dependent on the field than for alpha particles. This may be explained by the different rates of recombination depending on the applied electric field and also on the ionization density along the particle’s track, with stronger recombination at low electric fields and in denser ionization track like from alphas and nuclear recoils.

2.2.5 Electron transport parameters

In liquid xenon electrons are excited to the conduction band from the valence band by absorbing some of the energy from the incoming radiation and becoming free electrons. By applying an electric field the free electrons can escape recombination and the motion of these free electrons has been extensively studied as function of the concentration of impurities in the liquid [**44**], as a function of the liquid temperature [**45**] and very importantly as a function of the applied electric field on the liquid [**46**]. In Figure 2.10 is represented the electron drift velocity in liquid and solid xenon as a function of the applied electric field.

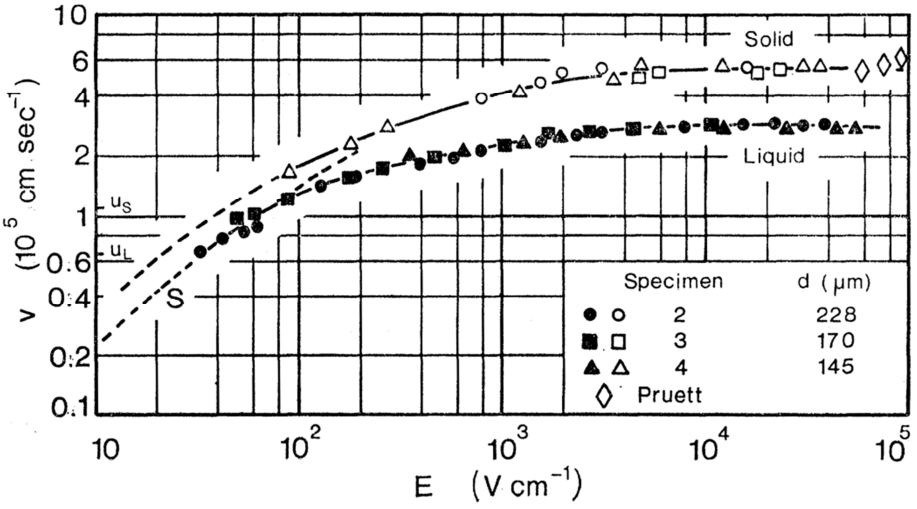

Figure 2.10 – Electron drift velocity as a function of the applied electric field in solid xenon (157 K) and in liquid xenon (163 K). Curve S is the theoretical Shockley hot-electron curve, μ_S and μ_L are the speed of sound in the solid and liquid, respectively.

At relatively low fields (<1 kV/cm) the electron drift velocity, v_D, varies almost proportionally with the field strength, E, according to the expression:

$$v_D = \mu E$$

where μ is the electron mobility. On the other hand, at high electric fields (>1 kV/cm) the electron velocity saturates at a value of 2.5 – 3 mm/μs, being independent of the electric field. An explanation of this phenomenon was developed by Cohen and Lekner [**47**] which distinguished two electron mean free paths: one describing the interaction between the electrons and acoustic phonons of the medium, which is independent of the structure of the medium, and another related to the momentum transfer of the electrons to the structure itself. At high electric fields the effect of the structure becomes substantial in the treatment of liquids and solids, translating to an increase of the scattering cross section, thus saturating the electron drift velocity.

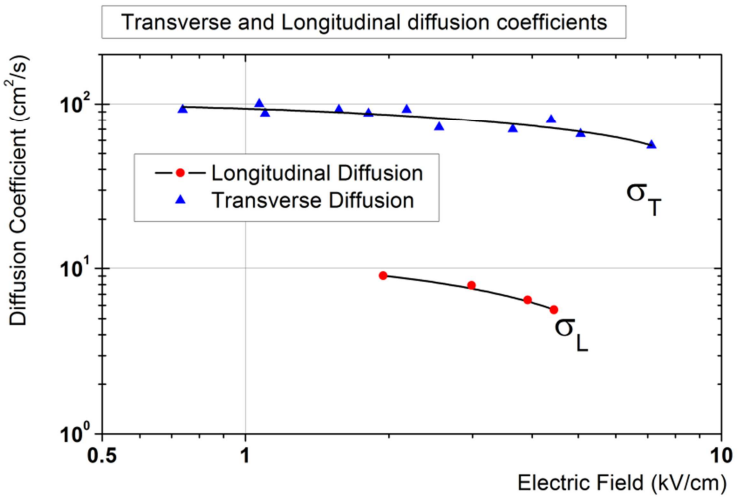

Figure 2.11 – Transverse and longitudinal diffusion coefficients for electrons in LXe as a function of electric field, adapted from [**48**].

The spread of an electron cloud created in liquid xenon due to the interaction with radiation is determined by the diffusion rate, which is a natural intrinsic limit to the position resolution of any time projection chamber employing liquid xenon. Applying

an electric drift field determines a preferential direction of diffusion, or longitudinal diffusion σ_L, and a secondary transverse diffusion σ_T, relative to field direction. In Figure 2.11 are represented the experimental results for the longitudinal and transverse diffusion coefficients in liquid xenon.

It was determined experimentally that the longitudinal diffusion σ_L is roughly one order of magnitude smaller than the transverse diffusion σ_T.

Chapter 3 – Experimental apparatuses and methods

3.1 Room temperature detector

In Coimbra an experimental system was developed for room temperature tests and measurements. This system allows for testing different detector geometries, different gas mixtures, photocathode characterization and optimization and will be used for the development of a two-dimensional readout that will be used in the cryogenic GPM. In this chapter a brief description of the sub-systems that compose the larger experimental system will be given.

3.1.1 Vacuum chamber

The vacuum chamber consists in a cylindrical stainless steel vessel (~150 mm diameter, ~2 liter) with provisions for UV or soft x-ray irradiation, as represented in Figure 3.1. For this purpose the chamber has two windows, visible in Figure 3.2: a 75 μm thick, 5 mm in diameter, Kapton window and a 5 mm diameter UV-transparent 1 mm thick quartz window, both glued with TRA-BOND low vapor-pressure epoxy to its top flange.

The chamber can be evacuated down to 10^{-5} mbar and then filled with the gas mixtures desired (namely, mixtures of Ne (N40, 99.99%), Ar (5.0, 99.999%), and He with CH_4 (4.5, 99.995%) or CF_4 (R14, purity of 99.8%) were used). The gases can be introduced up to a pressure up to at least 3 bar, through a liquid–nitrogen trap to reduce residual contaminants. After filling, the chamber is sealed off and the gas is continuously purified by circulation via convection through SAES St707 non evaporable getters, heated to ~150 ºC.

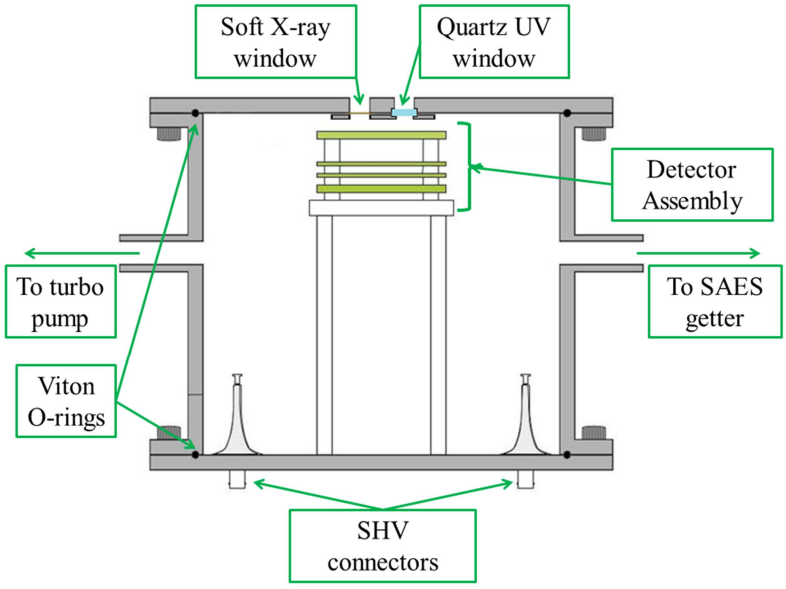

Figure 3.1 – Vacuum chamber cross-section, highlighting the soft X-ray and quartz UV windows, the detector assembly and SHV connectors.

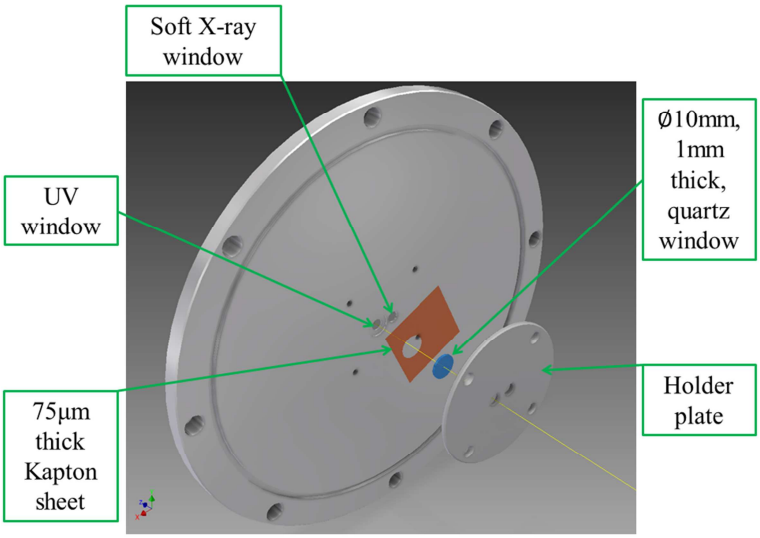

Figure 3.2 – Detail of the top flange, highlighting the soft X-ray and quartz UV window.

Several detector configurations and gas mixtures have already been successfully tested with either soft X-rays or UV light from an Oriel Hg(Ar) UV lamp, namely Single and Double-THGEM detectors in high pressure Ne/CF_4 mixtures [**49**], study of THGEMs coupled to submillimetric induction gaps in Ne/CF_4 mixtures [**50**] and the study of He/CF_4 and He/CH_4 mixtures [to submit to JINST].

3.1.2 Gas filling and purification system

The room temperature detector is composed of a gas system that allows different gas mixtures compositions – different gases or different ratios of gases that compose the mixture – to be introduced in the detector and their respective purification. In Figure 3.3 is represented the schematic of the gas system, highlighting the gas filling line, the chamber and the SAES getter based gas purification system.

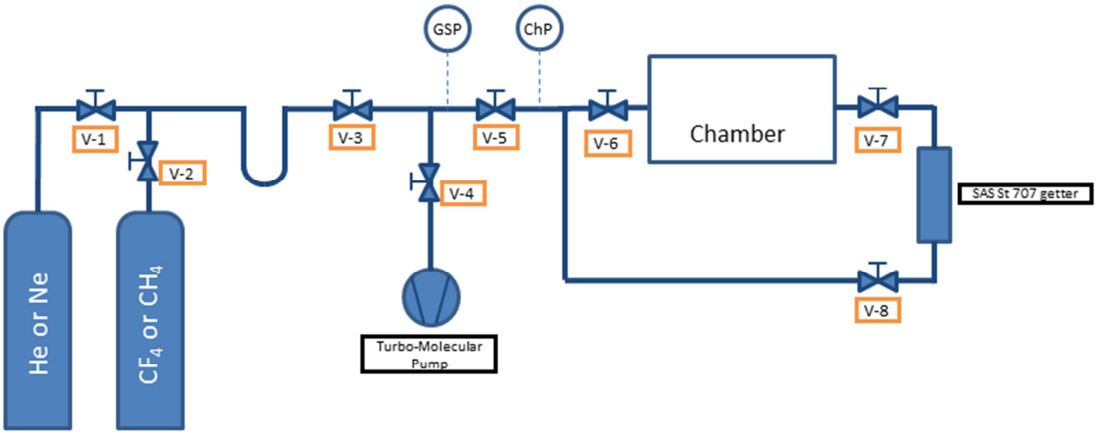

Figure 3.3 – Gas filling and purification system used in Coimbra.

To remove impurities from the gas mixtures, non-evaporable washers are used as getters, placed inside of an annex tube. Impurity levels for H_2O, O_2, H_2, CO, CO_2, and N_2 are significantly reduced. The non-evaporable getter is an alloy composed of zirconium, vanadium and iron which are melted together according to a particular vacuum metallurgic procedure and then crushed and ground to a fine powder. This powder can then be pressed in several shapes like washers, sheets or pills. Once activated and in operation at around 200 to 400 ºC the getter material captures and chemisorbs into its bulk the impurities already referred. Only noble gas atoms are not affected and if the temperature is low enough, molecular gases like CH_4 and CF_4 are also not absorbed. The high temperature applied for activation and reactivation of the getters, 350ºC – 400 ºC allows the efficient diffusion of the impurities into the bulk of the material, maintaining the porous surface free to absorb more impurities.

To activate and maintain the high temperatures required for optimal getter operation a temperature control system is implemented by a temperature controller, which regulates the power to a heating tape surrounding the tube in which the getter pellets are introduced. A thermocouple type K sensor in contact with the annex tube and

connected to the temperature controller provides temperature sensing capacity for temperature set-point regulation.

Two pressure sensors, represented in Figure 3.3 as GSP (for Gas System Pressure) and ChP (for Chamber Pressure), allow filling the vacuum chamber with the desired percentage of each gas composing the desired gas mixtures to within ~0.6%.

After filling, the chamber is sealed off and the gas is continuously purified by circulation via convection through SAES St707 non–evaporable getters, heated to a temperature below 150 ºC.

3.2 Photocathode production facilities

For room temperature studies using CsI photocathodes, an evaporation chamber is currently operational in Coimbra. This facility allows the vacuum evaporation of several materials on different substrates: of high purity cesium iodide on gold plated THGEMs or high purity aluminum films on stainless steel followed by cesium iodide deposition.

The evaporation chamber can be vacuum pumped down to ~10^{-6} torr by a diffusion vacuum pump in series with a rotary vacuum pump. The deposition rate of different materials is monitored (down to several angstroms per second) by a Thickness/Rate Monitor.

For photocathode production the THGEMs are previously thoroughly cleaned with acetone followed by alcohol and baked for approximately one hour. They are then transferred to the evaporation chamber and high purity (>99.9%) cesium iodide is deposited at a rate of 1 to 10 Å/s. After evaporation the chamber is filled with dry N_2 and opened under constant N_2 flow to minimize exposure to air moisture. The THGEM

is then placed in a transfer box filled with N_2 and installed in the room temperature detector chamber.

3.3 Weizmann institute of science liquid xenon system – WILiX

The experimental system recently developed and assembled in the Weizmann Institute of Science, which is represented in Figure 3.4 and Figure 3.5, allows reaching stable cryogenic experimental conditions in a cryostat which are necessary for xenon liquefaction. In this chapter the main elements will be described, namely the cryogenic equipment used for liquefaction and temperature control system, the circulation and purification systems, the heat exchanger and the safety devices implemented.

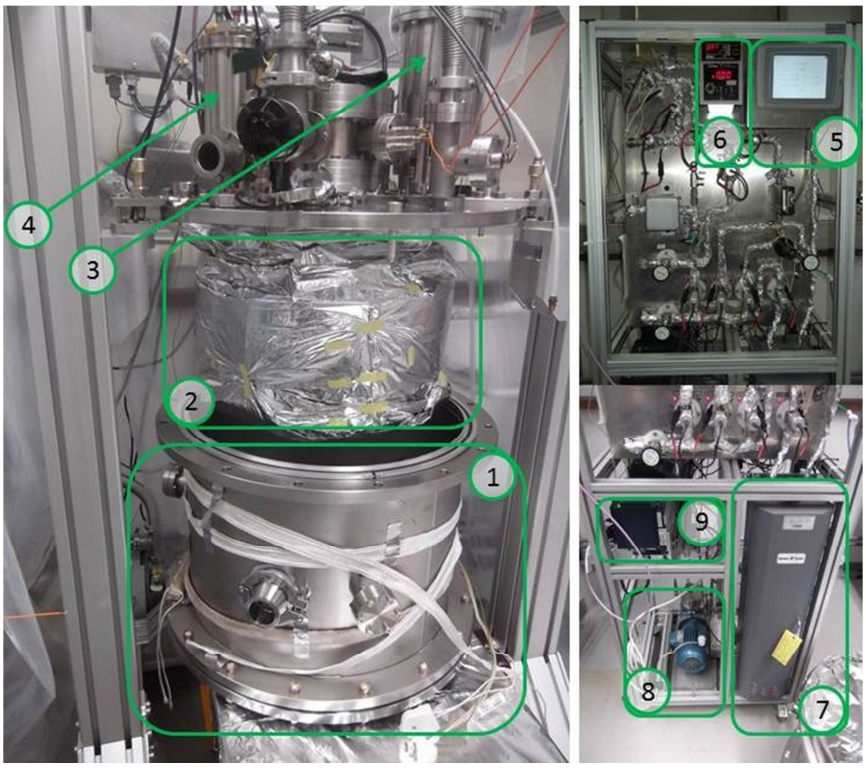

Figure 3.4 – 1) Outer Vacuum Chamber, 2) Inner Vacuum Chamber wrapped in several layers of aluminized Mylar, 3) Heat Exchanger, 4) PCC cold end housing, 5) Gas system control touch screen, 6) OVC, IVC pressure gauges and xenon flow regulator, 7) xenon gas purification system (SAES MonoTorr Purifier), 8) KNF double diaphragm circulation pump and 9) process variable acquisition and control rack.

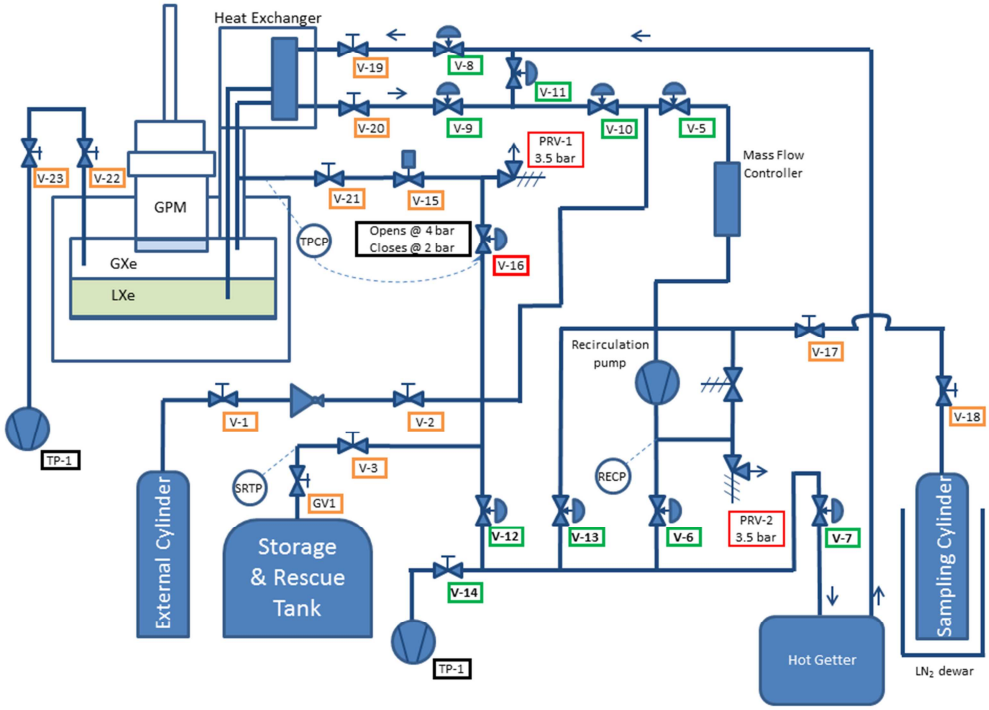

Figure 3.5 – Piping and instrumentation diagram of the Xe circulation system.

3.3.1 Xenon liquefaction and temperature control system

The xenon liquefaction and temperature control system is composed by a Brooks Automation, Inc. Polycold PCC Cryotiger and a Cryogenic Control Systems (Cryo-con), Inc. Model 24C Cryogenic Temperature Controller with associated temperature sensors and heater.

The Polycold PCC Cryotiger

The Brooks Automation, Inc Polycold PCC Cryotiger is represented in Figure 3.6. With this off-the-shelf equipment sufficient cooling power is delivered to a cryocooler which

is cooled to roughly 130 K and, through a copper cooling rod, to a set of specially designed oxygen-free copper fins inside the Inner Vacuum Chamber (IVC) where xenon is liquefied. Out of other methods available for reaching and maintaining the temperatures required for xenon liquefaction, such as using liquid nitrogen baths, preferred for the first generation prototypes of cryogenic chambers, or using pulse tube refrigerators (PTR's), used in some of the latest cryogenic experiments, the Polycold PCC Cryotiger was selected for its quietness, stability and simplicity of operation. The elements that compose the Polycold PCC Cryotiger are the compressor, the supply and return lines of the refrigerant and the cryocooler.

One of the main advantages in using this device is that the cryocooler can be physically distant from the compressor, which is main source of vibration and noise. This feature provides a stable and very quiet cooling element directly in the cryogenic chamber. When in operation the compressor receives low-pressure refrigerant from the cryocooler installed in the cryostat through the system gas return line. It compresses, cools and cleans the refrigerant gas and delivers it through the system gas supply line to the cryocooler. The cryocooler receives the high pressure, room-temperature refrigerant from the supply line and in its built-in heat-exchanger the supply refrigerant is cooled by the gas returning to the compressor. Before reaching the cold tip of the cryocooler the refrigerant is mostly liquid and very close to the final refrigeration temperature. A "throttle device" in the cryocooler allows the liquid refrigerant to expand to low pressure and enter the cold tip. The heat load on the cold tip is then absorbed by the refrigerant – this heat transfer causes some of the refrigerant to evaporate and slightly raises the fluid temperature.

Figure 3.6 – Brooks Automation Polycold PCC Cryotiger compressor, supply and return lines of the refrigerant gas and cryocooler.

The cryocooler provides a temperature range, using the proprietary gas blend PT-30, ranging from 100 K to 293 K with a heat removal capacity (cooling power) ranging from ~ 0.5 W to 30 W, respectively – with proper cryostat design and adequate thermal insulation of the cryostat this cooling power was enough to liquefy roughly 13Kg of xenon, as will be demonstrated. The cooling power curves versus the temperature of a "standard" Polycold PCC Cryotiger cryocooler are represented in Figure 3.7. It can be seen that for the gas-blend used, the cooling power is at its maximum when the cryocooler temperature is roughly 130 K.

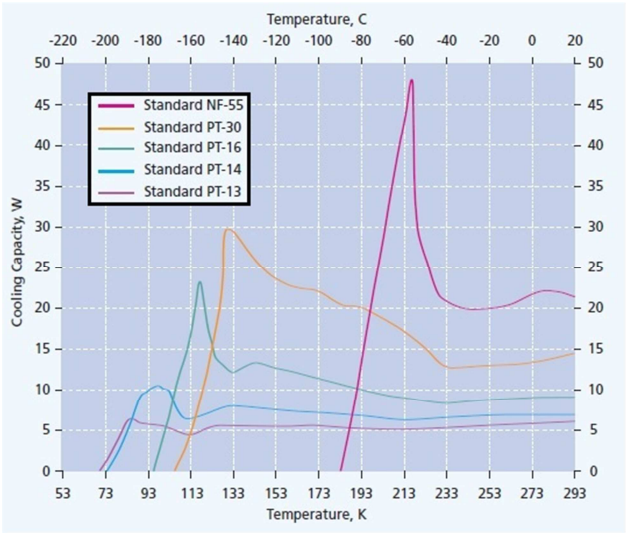

Figure 3.7 – Typical cooling capacity of the PCC Cryotiger using a standard cryocooler. The gas blend used for refrigeration is PT-30.

Once inside the IVC the gaseous xenon will transfer heat to the cooling fins until it reaches its temperature of liquefaction, beginning to condensate on the copper fins. Liquid xenon will then start to drip and flow through a cup beneath the copper fins and into the IVC.

Temperature control

The temperature control mechanism implemented is based on a Cryo-con, Inc. Model 24C Cryogenic Temperature Controller with associated temperature sensors and a heater cartridge installed in the cooling fins.

Along the length of the cryocooler, cooling rod and cooling fins assembly, four temperature sensors were installed (one Cryo-con S900 silicon diode temperature sensor and three Lakeshore PT-111 Platinum Resistance Thermometers), as represented in Figure 3.8, using a four-wire configuration for highest precision. Thermal coupling of

the temperature sensors to each of the elements was made with Apiezon-N cryogenic high vacuum thermal grease and care was taken to ensure good thermal anchoring by winding the connection wires around the cooling rod and coating with cryogenic varnish diluted in a 50/50 toluene/methanol solution. Thermal coupling between the separate cryocooler, cooling rod and cold fins elements was ensured by use of indium sheet.

The cooling power of the PCC's cryocooler is temperature dependent but the power delivered by the compressor is constant and it continuously cools the cryocooler. The temperature reached in the cooling fins without any means of control would eventually freeze the xenon inside the IVC. In order to avoid such event the temperature regulation is provided by a 25 W cartridge heater installed in the cooling fins. The heater is controlled by the Cryocon Model 24C Cryogenic Temperature Controller, represented in Figure 3.9, which implements a fully tunable PID, or Proportional Integral Derivative, control loop which regulates the heating power delivered. The temperature is measured directly on the cooling fins with one of the PT-111 PRT sensor. In operation this system provided an extremely stable operation temperature of ±0.5 K around the set point, at 165 K.

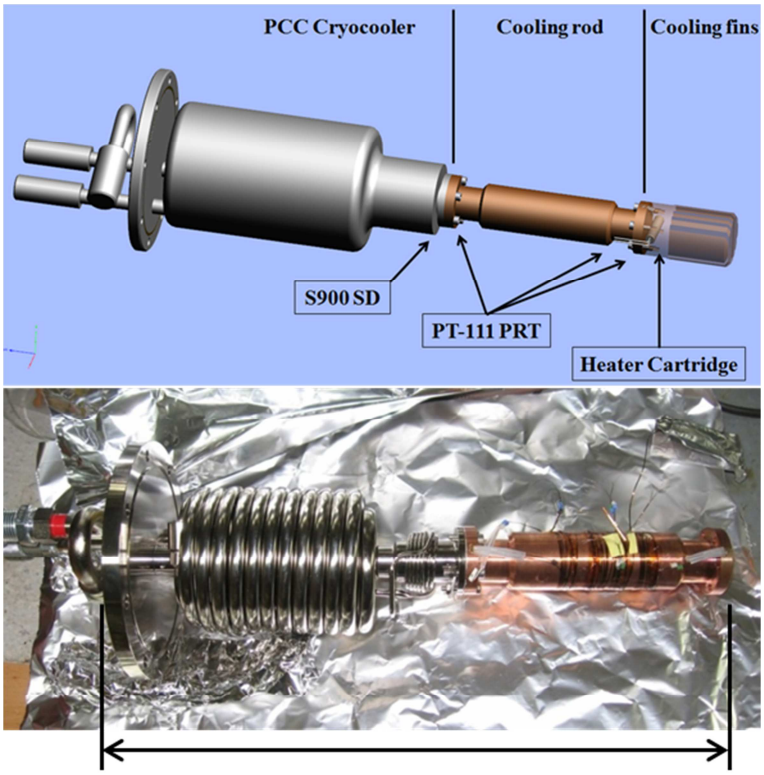

Figure 3.8 – Top: Autodesk Inventor representation of the PCC cryocooler with cooling rod and condensation fins, also visible is the 100 W heater; Bottom: Photograph of the PCC cryocooler and cooling rod already instrumented with temperature sensors, before thermal insulation with aluminized Mylar.

Figure 3.9 – A pair of Cryo-con, Inc. Model 24C Cryogenic Temperature Controllers. Left one is used for WILiX while the right is one used for the GPM temperature control.

Outer vacuum chamber (OVC) and inner vacuum chamber (IVC)

The technical schematic of the Outer Vacuum Chamber and the Inner Vacuum Chamber, with the future GPM detector assembled is represented in Figure 3.10.

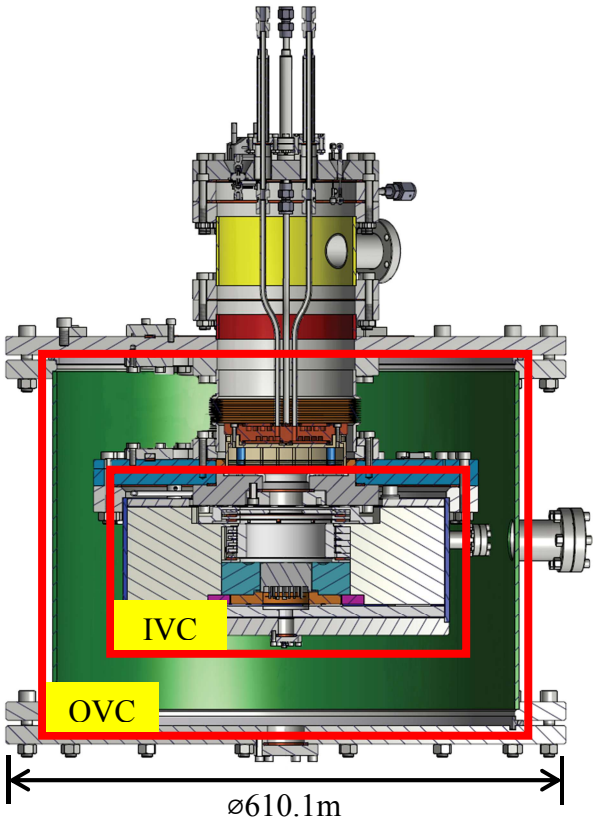

Figure 3.10 – Technical drawing of the OVC and IVC. Also visible is the future GPM detector in the Teflon block. The linear manipulator, cryocooler with cooling rod and cooling fins and the heat exchanger have been removed for clarity.

Once the xenon is liquefied and starts to drip from the condensing fins it gradually fills the Inner Vacuum Chamber (IVC). The IVC is a stainless steel vessel which contains the detector and where the liquid xenon is kept during the course of the

experimental phase. The heat transfer routes with the exterior are by convection, conduction and radiation. In order to keep the xenon in liquid state the heat transfer rates with the exterior must be minimized.

In order to minimize the heat exchanges between the IVC and the exterior by convection, the IVC is placed inside a large Outer Vacuum Chamber (OVC). The OVC is served by a dedicated vacuum station composed by a turbo–molecular vacuum pump followed by rotary scroll pump, which are in constant operation during the course of the experiments to maintain the vacuum in the OVC at ~10^{-6} torr. The absolute vacuum reached inside the OVC after 2 days of pumping is usually around ~10^{-5} torr.

To minimize the heat exchanges by conduction between the IVC and the exterior the IVC is supported inside the OVC by the minimum number of stainless steel tubes and bellows, which must serve both as physical supports and as a way to make the electrical connections from the inner detector inside the IVC with the exterior. Also installed is a large central bellows with a viewport – which will later be substituted by a large area fused quartz window for the GPM.

Finally, in order to minimize the heat exchanges by radiation, the IVC, the supporting stainless steel tubes and bellows with electrical wires and the large central bellows with the viewport and window are wrapped in several layers (>10) of thin aluminized Mylar, as can be seen in Figure 3.4, and a special sheet composed of insulating fabric sandwiched between 2 thick layers of aluminized Mylar, absorbing infra-red radiation.

3.3.2 Xenon circulation and purification

In order to continuously purify the xenon, removing the electronegative impurities such as water, oxygen or carbon dioxide that degrade the ionization and scintillation signals, WILiX has a closed circulation system which extracts liquid xenon from the IVC, converts it to gas in a heat exchanger, passes it through a getter based purification system and feeds it back into the IVC. The gas circulation system was designed having in mind the necessity for vacuum pumping and for high temperature baking, from 100ºC to 150ºC. All the piping components are manufactured from stainless steel and were thoroughly cleaned before installation and baked under vacuum pumping. Metal gaskets were used throughout the system (stainless steel for the Swagelok VCR tubes and connectors and copper for the large IVC flange), while the use of Viton gaskets is limited to the circulation pump. The gas system was thoroughly helium leak tested down to ~10^{-8} mbar/l*s.

Circulation pump

The circulation pump used on the system is a KNF N 143 SV.12 E diaphragm pump with a double diaphragm system. Its operation is illustrated in Figure 3.11. All the diaphragms and O-rings are made of Viton material. The pump is of the dry type since it does not use oil in the transfer volume, avoiding contamination of the xenon.

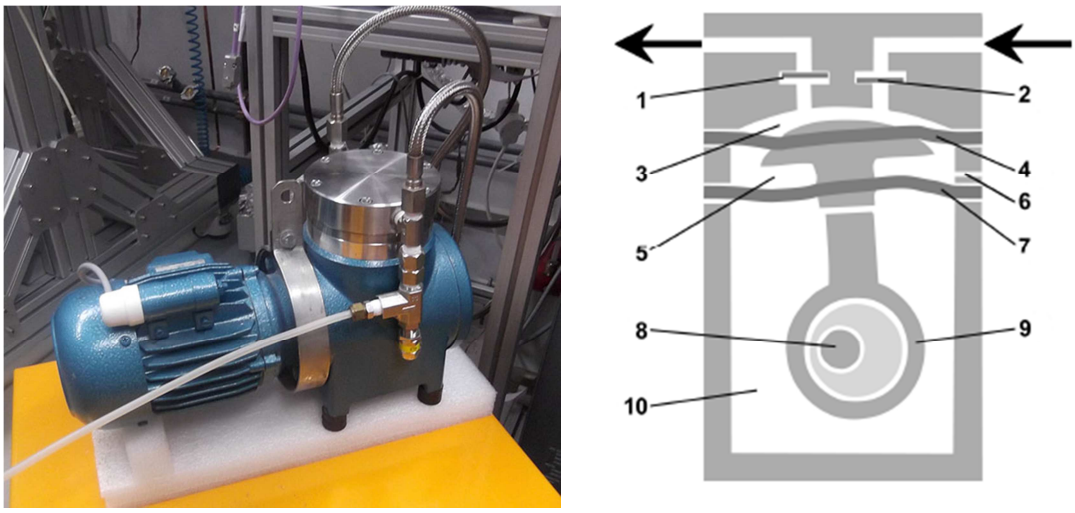

Figure 3.11 – A) Photograph of the KNF pump with pressure relieve valve installed on output and B) Simplified diagram of the circulation pump. 1) outlet valve, 2) inlet valve, 3) transfer chamber, 4) working diaphragm, 5) inter-diaphragm space 6) hole for inter-diaphragm space pressure monitoring, 7) safety diaphragm, 8) eccentric, 9) connecting rod and 10) pump drive.

The working diaphragm is moved vertically by the eccentric and connecting rod. In the downward motion xenon gas is aspirated through the inlet valve due to a decrease in pressure which also closes the outlet valve. In the upward motion the gas is pushed out through the now opened outlet valve. The volume of the transfer chamber is hermetically separated from the outside by the working diaphragm and a second, safety diaphragm. Since the working diaphragm is under strong mechanical stress the safety diaphragm (under less stress) installed underneath the working one prevents any possible leak developed in the working diaphragm to/from the outside – with consequent loss of xenon.

Getter based purification

To remove impurities from the gaseous xenon a commercial SAES MonoTorr Phase II model PS4-MT3-R-2 heated zirconium based getter is used. Zirconium is an effective absorbent since its surface bonds with virtually any non-noble gas species including O_2, H_2O, N_2. The purifier heats the getter element to a temperature of several hundred degrees Celsius, which encourages impurities that are bonded to surface sites to diffuse into the bulk, leaving the surface available for additional gettering. Impurity levels for H_2O, O_2, H_2, CO, CO_2, CH_4 and N_2 are reduced to the parts per billion levels. The single-pass purification efficiencies were measured to be greater than 99.99% and 99.9% for O_2 and N_2, respectively. These values were measured at a flow rate of 12.6SLPM, and at the default getter temperature of 400 ºC. These values are expected to further improve using lower flow rates.

3.3.3 Internal vacuum chamber (IVC) volume

Inside the inner vacuum chamber, or IVC, several kilograms of xenon are condensed and maintained in liquid state by the Polycold PCC Cryotiger. A multipurpose support, or bath, was designed and machined from a large block of Teflon providing a platform for detector or time projection chamber assembly with provisions for a cryogenic photomultiplier. This bath allows directing the liquid xenon flow through the central core for efficient extraction and several temperature and capacity sensors were installed throughout. The Teflon bath is represented in Figure 3.12 with sensor placement points highlighted.

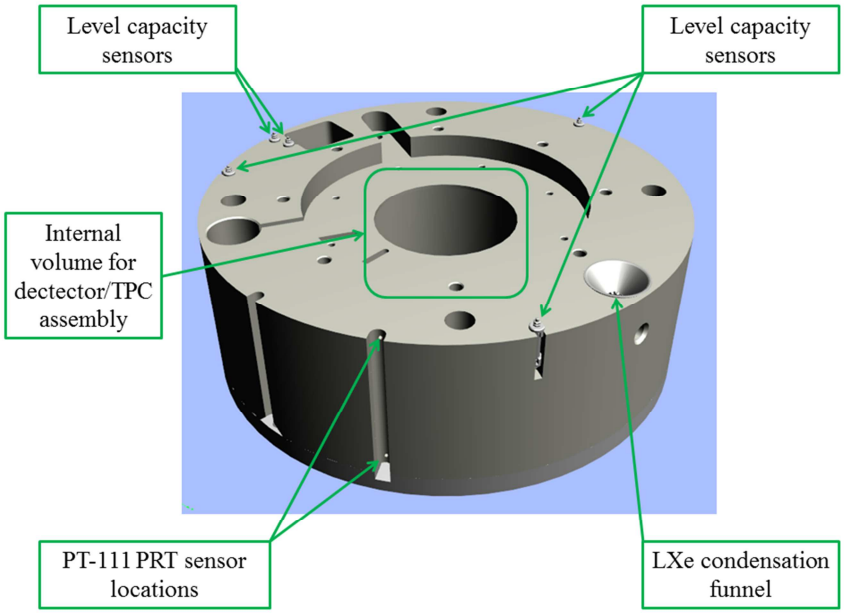

Figure 3.12 – AutoCAD design of the Teflon bath with sensor location highlighted.

The sensors installed in the Teflon bath serve several purposes: to monitor the temperature inside the IVC at two different heights, to sense the level of liquid xenon and finally to sense the tilt of the chamber. A cold-cathode vacuum sensor was also installed on the IVC in order to measure the pressure when vacuum pumping and a MKS Baratron is used for measuring xenon gas-phase pressure.

The temperature sensors installed are two Lakeshore PT-111 PTRs and they are placed in drilled holes on the top and bottom of the Teflon bath. They are held in place by Teflon wedges. The electrical connection to each of these sensors is made in a 3-wire scheme to a PACSystems RX3i Universal Analog Input Module.

The capacitive sensors are manufactured as hollow stainless steel cylinders, into which liquid xenon is allowed to flow in, with an internal conductor. The walls of the cylinder, the internal conductor and the liquid xenon form a capacitor with the liquid xenon being a portion of the dielectric. As the level of liquid xenon changes a

corresponding change in capacitance occurs, which is then transmitted over shielded cables to dedicated electronic equipment for processing, logging and display. Five of such capacitors sensors are installed: one large capacitor spanning the height of the Teflon bath and a smaller one installed inside the pool from where liquid xenon is extracted. The remaining three capacitor sensors were installed on the rim of the Teflon batch 120º apart. The purpose of these sensors is to detect the tilt of the chamber provided sufficient sensitivity is achieved.

The temperature and capacitive sensors are connected by a 19pin Accu–Glass ultra-high-vacuum (UHV) PEEK connector to a UHV CF feedthrough flange and to the exterior.

The internal volume machined in the Teflon block allows room for installation of several components: from single stage THGEM detectors operating immersed in the liquid xenon, along with high transparency meshes and a complete photomultiplier tube assembly, to a future time projection chamber with a height of 43 mm (if using a R6061 PMT) and a diameter of 107 mm that will be used with the GPM.

Below, in Figure 3.13, typical temperature and gas-phase pressure evolution plots are represented, as measured during a cooling phase. The temperature curve shown corresponds to the topmost sensor on the Teflon block. The IVC is initially filled with approximately 2 bar of xenon. With the cryocooler in operation the pressure and temperature of the gas gradually decrease – in this case the average rate of temperature change was about –0.92 K/hour. During the following days xenon gas is periodically introduced to approximately 2bar and eventually liquid xenon begins to form on the bottom of the IVC. The presence of liquid xenon is confirmed when the capacitance from the large capacitor gradually increases, as represented in Figure 3.14.

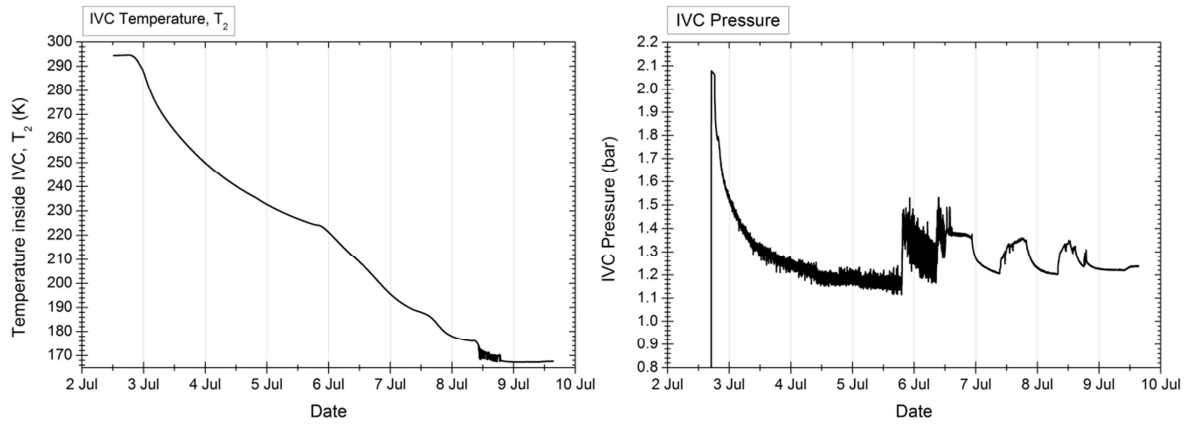

Figure 3.13 – Temperature and pressure logs registered during cooling and filling the IVC.

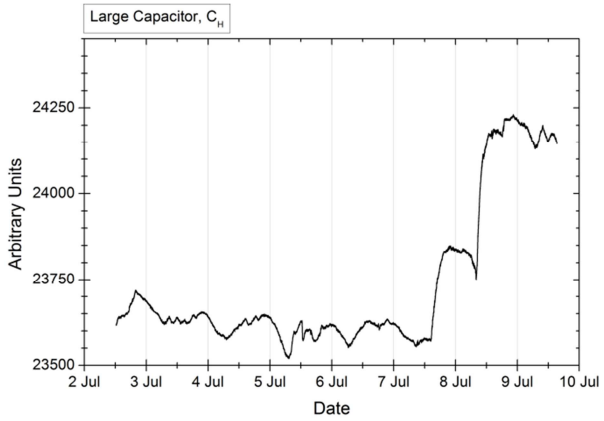

Figure 3.14 – Measurement (proportional to capacitance) of the large capacitor.

3.4 Large electrode preparation and testing

3.4.1 Leak current measurement

In order to have some preliminary indication about the quality of each of the THGEM electrodes, a setup was used that permitted the biasing of one the electrode faces while

the other was connected to a grounded and discharge protected picoammeter. The setup allowed the installation of an electrically insulated THGEM in a closed vessel while constantly flushed with pure nitrogen gas. By applying increasingly higher voltages, up to the sparking limit, and recording the electrical current on the picoammeter the THGEM leakage current versus applied voltage can be determined.

The THGEM electrodes that showed the lowest leakage current were considered potential candidates for installation on the GPM, while the ones that showed that highest were reprocessed with the standard cleaning method: 1) Cleaning the electrode with doubly deionized water followed by 2) 30 minutes in an ultrasonic bath of iso-propyl alcohol followed by 3) 1 hour in 60º and then followed by 4) 2 hours at 95º. After this procedure they were re-tested. The criteria that was used for selecting "good" electrodes, in terms of leakage current, was that for any applied voltage up to 1.5 kV on the THGEM electrode, the current measured on the picoammeter after 10 minutes of stabilization, should be lower than 0.5 nA and present no significant fluctuations.

3.4.2 Optical discharge localization

Each THGEM tested was thoroughly flushed with dry N_2 gas (not high pressure air) and installed in a chamber with a large Mylar window. The window provided unobstructed view of the full area of the THGEM. Each THGEM was biased on the top electrode while the bottom electrode was kept at ground potential. The chamber was flushed with pure helium gas – which decreased the THGEM discharge voltage from ~1800 V to ~500 V. A large number (~10^3) of individual discharge events were recorded for each THGEM with a FLI CCD camera (512x512pixels) set for an exposure time of 0.2 seconds, through a Nikon Nikkor f/1.6 50 mm objective. The camera was cooled by an

internal Peltier cooler and was set for continuous frame acquisitions, from which only the frames where discharges could be seen were selected. The system used is represented in Figure 3.15. Each frame was then processed in MatLab and the position of each discharge event was localized and recorded. In Figure 3.16A, the illuminated THGEM electrode is shown framed in the image as to occupy most of the area possible, while in Figure 3.16B a typical recorded discharge is shown, as localized by MatLab. Each of the localized discharge events are then plotted according to its position and the number of times a discharge was initiated by the same hole was determined for each THGEM. This provided a clear indication of a damaged hole or area.

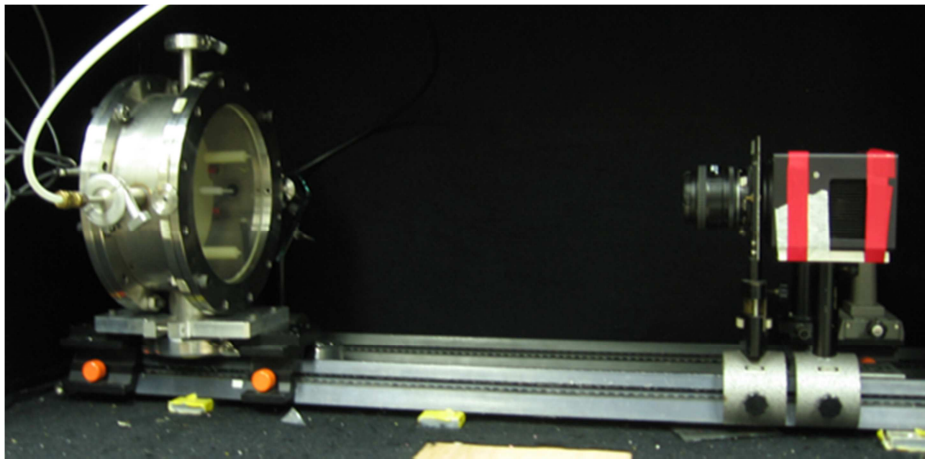

Figure 3.15 – Photograph of the setup used for THGEM discharge studies. Gas chamber, objective and the FLI camera are visible.

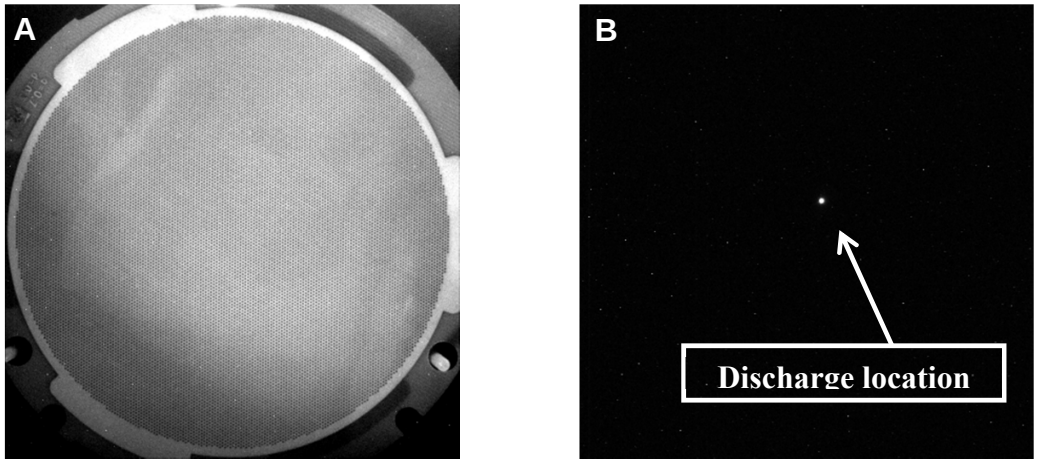

Figure 3.16 – A) Image of an installed THGEM acquired by the FLI CCD camera, and B) a typical raw image of a discharge.

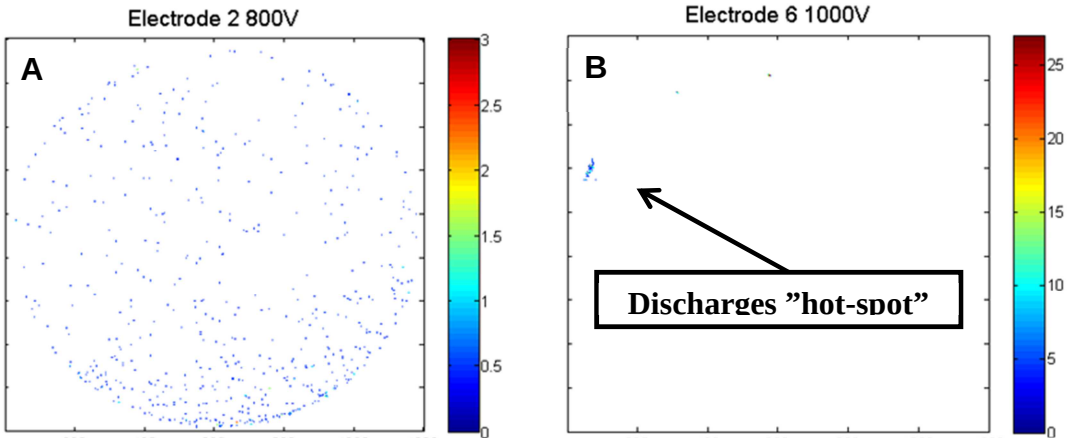

Figure 3.17 – Position of discharges after MatLab processing for a "good" electrode (A) and a "bad" electrode (B). Discharges in B are heavily localized. Scale on right indicates maximum number overlapping discharge events.

In Figure 3.17 the spatial distribution of discharges is shown for two extreme cases: for a "good" electrode, Figure 3.17A, and for a "bad" electrode, Figure 3.17B. In the good electrode the recorded discharges occurred well distributed throughout all of its area – the round shape of the electrode can clearly be inferred – and only three

discharges occurred in the same hole, shown by the color bar on the right. In the “bad” electrode most of the recorded discharges occurred in a very localized area (close to the 9 o’clock position) and more than 25 discharges occurred in the same hole, shown on the color bar on the right. In this particular case, upon close inspection of the problematic area, it was observed that at some point in time the electrode was handled without gloves as witnessed by a fingerprint. Cleaning the electrode with doubly deionized water followed by 30 minutes in an ultrasonic bath of iso-propyl alcohol followed by 1 hour in 60 ºC and 2 hours at 95 ºC for drying purposes, improved its condition dramatically.

The THGEM electrodes that were selected for use filled mainly two criteria: 1 – a low value of leakage current below ~5×10^{-10} A, preferably below 1×10^{-10} A, and 2 – the discharge locations should be somewhat spread over the area the electrode, i.e. not having a “hot-spot” where >10 discharges occurred over the measurement time.

Chapter 4 – Cesium iodide photocathode production and characterization

4.1 Introduction

The proposal by G. Charpak, in the 1980's, of using cesium iodide photocathodes coupled to gas detectors for the detection of UV photons [**51**], opened a window of new detection possibilities explored in depth by the RD26 collaboration, in the 1990's [**52**]. The results of this collaboration were important in understanding the processes leading to the improvement of photocathodes, from the choice of substrate and optimization of deposition procedures to the selection of operating gases in order to minimize photoelectron backscattering, to long-term quality assessments of deposited photocathodes [**53**] [**54**].

Cesium iodide has good quantum efficiency in the VUV region of the electromagnetic spectrum (100 nm to 200 nm) and although being hygroscopic its production is relatively simple and it is significantly more stable than other types of photocathodes like bi-alkali or multi-alkali photocathodes. Moreover, for the successful use of a cesium iodide photocathode, a suitable substrate needs to be used in order to avoid chemical reactions that dissociate the CsI, resulting in the loss of quantum

efficiency – studies performed within the RD-26 collaboration framework have shown that gold, nickel or aluminum substrates are the most appropriate. For this reason the THGEM electrodes used in the GPM are gold-plated.

4.2 Photon conversion in cesium iodide

The process of photon detection with cesium iodide photocathodes relies on the external photoelectric effect where photons with energy above a certain threshold are absorbed by the photosensitive material within a certain depth. This generates mobile charge carriers which are ejected from its surface under certain conditions in a process called photoemission. The charges are then accelerated by an electric field and multiplied generating a measurable current pulse.

Distinctively from the photoelectric effect in metals being illuminated by mono-energetic radiation, *hν*, where the maximum energy of emitted photoelectrons is given by the relation:

$$E_k = h\nu - \phi^W$$

and where the work function, ϕ^W, is the energy difference between the fully occupied valence band (up to the Fermi level) to the vacuum energy level (in gold for example, ϕ^W(Au)=5.1eV), in semiconductors like cesium iodide the excited electrons are mostly emitted from the valence band with a maximum energy given by:

$$E_k = h\nu - (E_g + \chi)$$

where E_g is the energy bandgap from the top of the valence band to the conduction band and χ is the electron affinity of the specific material – which is the energy gap from the

conduction band minimum to the vacuum energy level. From the literature it can be established that for CsI, due to experimental uncertainties, there is quite a significant scatter around the most probable values for the energy bandgap, E_g, the electron affinity, χ, and the energy threshold for photoemission, E_t. Combining several authors [**55**] [**56**] [**57**] it can be established that for CsI E_g=6.0 eV, χ= 0.2 eV and E_t=6.2 eV.

The external photoelectric effect occurring in cesium iodide photocathodes can be described by the Spicer Three-Step model [**58**] and [**59**], which treats the electron photoemission in terms of three successive steps:

1) Optical absorption of a photon into the bulk of the photocathode leading to the liberation of electrons into the bulk,
2) The motion of the electrons through the bulk of the crystalline structure of the photocathode towards its surface, and
3) Escape of the electrons from the photocathode's surface.

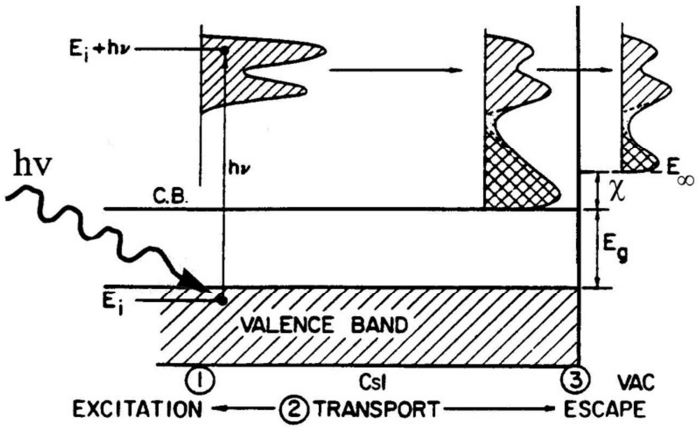

Figure 4.1 – Representation of the Spicer Three-Step model, adapted from [**59**].

These three steps are depicted in Figure 4.1. Electrons reaching the surface of the photocathode can only escape if their energy is greater than the vacuum level. The

Three-Step model provided the means of understanding photo-emitters, and more generally it has been found to describe photoemission from all solids, besides that it gave the possibility of estimating the yield of a photo-emitter (photoelectrons per photon) as a function of photon energy. A more sophisticated development of the Spicer Three-Step model by Berglund and Spicer [**60**] gives the energy distribution of the emitted photoelectrons.

To determine the basic equation for the quantum yield of a photocathode in the frame of the Three-Step model it is necessary to recognize the excitation of photoelectrons as a consequence of a bulk absorption effect [**58**]. Photons hitting the photocathode will transverse a certain thickness of material before being absorbed, meaning that the light intensity *I* after traversing a thickness *x* of material is given by:

$$I(x, h\nu) = I_0(h\nu) * (1 - R(h\nu))e^{-\alpha(h\nu)*x}$$

where $I_0(h\nu)$ is the initial intensity of photons, $R(h\nu)$ is the photocathodes' surface reflectivity and $\alpha(h\nu)$ is the photocathodes' absorption coefficient, as a function of incident photons' energy, $h\nu$. The amount of light absorbed at a distance *x* from the photocathodes' surface can then be given by:

$$dI(x) = I_0 * (1 - R)e^{-\alpha(h\nu)*x} * \alpha * dx$$

Some of the excited electrons induced by the absorbed light will then travel to the surface and escape originating from a layer *x* to *x+dx*. The contribution *di*(x) from the layer *x* to *x+dx* to the quantum efficiency or yield can then be expressed by:

$$di(x) = P_{0\alpha}(h\nu, x, dx) * P_T(h\nu, x) * P_E(h\nu)$$

where $P_{0\alpha}(h\nu, x, dx)$ is the probability of exciting electrons above the vacuum energy level in the layer x and $x+dx$, or the "absorption probability,", $P_T(h\nu, x)$ is the probability that electrons reach the surface with sufficient energy to escape, or "transport probability" and $P_E(h\nu)$ is the probability of escape of electrons reaching the surface, or "escape probability". Where $P_{0\alpha}(h\nu, x, dx)$ is given by:

$$P_{0\alpha}(h\nu, x, dx) = \alpha_{PE}(h\nu) * I(x)dx = \alpha_{PE}(h\nu) * I_0(1-R)e^{-\alpha x}dx$$

where α_{PE} represents the part of the photoelectrons that have energy higher than the vacuum energy level and have the possibility to escape. It can also be shown that [**58**]:

$$P_T(h\nu, x) = e^{-\left(\frac{x}{L(h\nu)}\right)}$$

where $L(h\nu)$ is the electron scattering length, since the electron scattering probability is proportional to the distance traveled. This way, for $di(x)$, we have:

$$di(x) = \alpha_{PE} * I_0(1-R)e^{-\alpha x} * e^{-\left(\frac{x}{L}\right)} * P_E(h\nu)dx$$

The quantum efficiency, or yield, for a given wavelength can then be defined as the ratio between the emitted photoelectrons to the number of impinging photons.

$$QE = \frac{i}{I_0} = \frac{\frac{\alpha_{PE}}{\alpha}P_E}{1+\frac{l_\alpha}{L}}(1-R)$$

where $l_\alpha = 1/\alpha$ is the absorption length, l_α/L is the ratio of absorption length to scattering length and α_{PE}/α is the fraction of electrons excited above the vacuum level, which normally increases monotonically as $h\nu$ increases above the threshold for emission (E_t=6.2 eV, for CsI). From this expression it can be observed that in order to

maximize the quantum efficiency then $l_\alpha \ll L$, meaning that a large fraction of the photo-excited electrons contribute to the yield, and that α_{PE}/α and P_E should be close to unity.

4.3 Cesium iodide photocathode evaporation

The CsI photocathodes used in the GPM were deposited on one side of the THGEM electrodes by Joule effect, on the evaporation setup available at the Weizmann Institute of Science. The THGEM electrode is clean beforehand with the standard procedure: 1) flushed with doubly deionized water followed by 2) 30 minutes in an ultrasonic bath of iso-propyl alcohol followed by 3) baking for 1hour at 60 ºC while flushing with pure nitrogen and followed by 4) baking for 2 hours at 95 ºC also flushing with pure nitrogen. The THGEM electrode is then attached to an aluminum heater base which provides some level of annealing before and after deposition, which enhances the quantum efficiency of the photocathode [**61**] and [**62**]. The aim is to maximize the CsI photocathode quantum efficiency and to improve resistance to short term exposure to air during the transfer and installation, from the evaporation chamber to the GPM. In view of this the evaporation plant in WIS, schematically represented in Figure 4.2, was designed for large area photocathode production, to accommodate the large 123 mm diameter THGEMs and, based on the experience previously gained, provisions were made in order to have inside the evaporation chamber a heating element to heat the large THGEM surface by conduction prior to evaporation. Moreover an in-situ relative quantum efficiency determination is possible using an Ar-Hg UV lamp, a monochromator and monitoring photodiode. A Meissner trap was also recently designed, manufactured and installed in order to improve the photocathode evaporation

conditions, reducing the absolute vacuum level by approximately one order of magnitude.

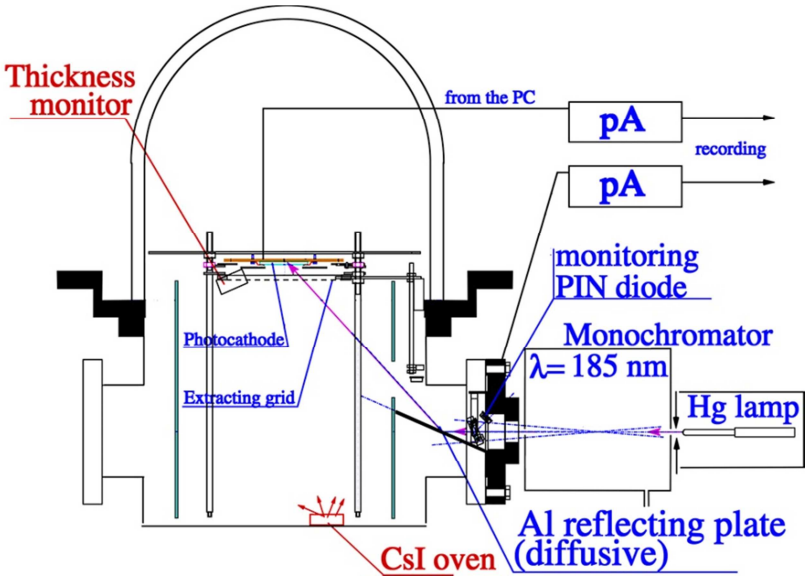

Figure 4.2 – Scheme of the CsI evaporation setup by Joule effect.

Before loading the evaporation crucible with CsI, the chamber is vacuum pumped down to ~1x10^{-7} torr and filled with argon. After opening the evaporation chamber, by removing the glass bell, a sealed vial with CsI (purity of 99.999%) is placed on the chamber bottom and then opened. A significant amount of CsI powder is then loaded on the tungsten crucible and the vial is then closed and removed. The evaporation chamber is then closed and vacuum pumped again down ~1x10^{-7}torr. The CsI loaded on the tungsten crucible is then heated to its melting point (T_{fusion} = 621 ºC) at high vacuum in order to remove any impurities or humidity before evaporating on a THGEM electrode (this process is the pre-melting phase).

The THGEM electrode assembled on the aluminum heater base is then installed under argon atmosphere in the evaporation chamber facing the CsI loaded tungsten

crucible and vacuum pumped again down to ~$1x10^{-7}$ torr. With an internal shutter closed, current is applied to the tungsten crucible and gradually increased until melting begins. At that moment the shutter is opened and the evaporated CsI is deposited on the opposite THGEM electrode.

The thickness and deposition rate is monitored by a Sycon Thickness/Rate Monitor STM-100 with a quartz oscillator, and manually controlled by adjusting the applied current to the tungsten crucible at a rate of 8 to 10 Å/s to a thickness of ~3000 Å. After the deposition procedure the photocurrent from the photocathode is monitored for 24 hours and the entire evaporation chamber is then enclosed in an airtight glove-bag which is then filled with dry nitrogen. The glass bell of the evaporation is removed under the nitrogen filled glove-bag and the THGEM electrode with the CsI photocathode, still on its aluminum heater base, is transferred to a transportation chamber and sealed under nitrogen. The transportation chamber with the THGEM electrode is removed from the glove-bag and it can either be a) transferred to the nitrogen filled glove-box for installation on the GPM or b) coupled to a McPherson 302 vacuum monochromator for a precision measurement of the photocathodes' quantum efficiency. The measurement in the vacuum monochromator exposes the CsI to air for a few seconds during installation so this step is usually only used for calibrating the in-situ measurements in the evaporation chamber.

4.4 Photocathode characterization

The quantum efficiency can be estimated, in-situ, by illuminating the photocathode with light from an Oriel Hg(Ar) calibration lamp wavelength selected to 185 nm using an Oriel monochromator model 77250 flushed with pure nitrogen gas. The light intensity is

monitored using a UV beam-splitter and a far-UV sensitive Hamamatsu S1722-02 Si PIN photodiode. By comparing the measured photocurrent from the photocathode, normalized to the light intensity from the photodiode, with previous measurements with other photocathodes with a known quantum efficiency determined with a McPherson 302 vacuum monochromator, the quantum efficiency of the photocathode can be estimated to within ±10%. This is a relative quantum efficiency measurement.

To determine the absolute quantum efficiency of a photocathode its photocurrent is measured as a function of wavelength in a McPherson 302 vacuum monochromator, equipped with a deuterium light source, versus the photocurrent of a Ball Aerospace far-UV vacuum photodiode (s/n: 1-926) calibrated by the National Institute of Standards and Technology (NIST). The photodiode is operated with +150 V bias, has a cesium telluride photocathode, a magnesium fluoride window and a precisely known quantum efficiency curve (to within 6% between 1164 Å and 2000 Å). The monochromator is equipped, at the exit port, with a 1m focal length collimator which collimates and reduces the light spot size to ~8 mm. Moreover the vacuum monochromator has a third port, besides the entrance and exit ports, where the current from a phototube operating in collection mode allows monitoring the light intensity for normalization. The currents are measured by Keithley 610C pico-amperimeters. In Figure 4.3 is shown the simplified schematic of the vacuum monochromator setup.

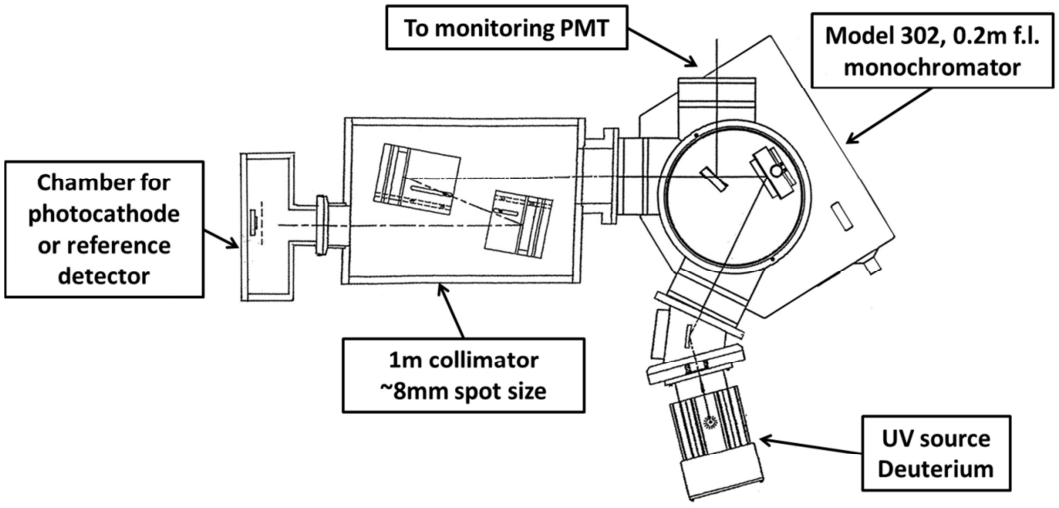

Figure 4.3 – Simplified schematic of the CsI photocathode quantum efficiency measurement setup with the McPherson 302 monochromator.

The quantum efficiency of a CsI photocathode, $QE_{CsI}(\lambda)$, as a function of the wavelength is then determined according to the following equation:

$$QE_{CsI}(\lambda) = QE_{Ball}(\lambda) * \frac{I_{CsI}(\lambda)}{I_{Ball}(\lambda)} * \frac{I_{MonitorBall}(\lambda)}{I_{MonitorCsI}(\lambda)}$$

Where $QE_{Ball}(\lambda)$ is the known quantum efficiency of the Ball Aerospace photodiode, $I_{CsI}(\lambda)$ is the measured photocurrent of the CsI photocathode, $I_{Ball}(\lambda)$ is the current measured from the Ball Aerospace photodiode, $I_{MonitorBall}(\lambda)$ and $I_{MonitorCsI}(\lambda)$ are the currents from the monitoring PMT during measurement with photodiode and photocathode, respectively. In Figure 4.4 is represented the quantum efficiency of the Ball Aerospace photodiode and respective error bars, as stated in the original NIST certificate of calibration from 1993, and the recalibrated quantum efficiency measurement performed in 2015. A decrease of ~12% at 175 nm from the original value

was observed, representing a decay of ~1% per year, which is within the <3% per year likelihood drift stated by NIST.

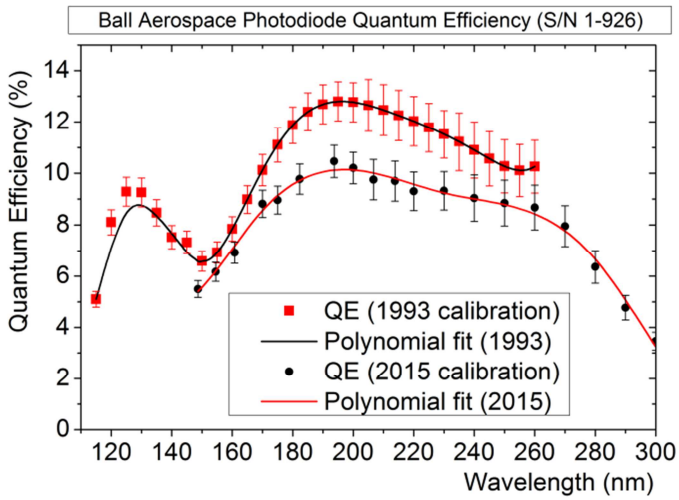

Figure 4.4 – Quantum efficiency of the Ball Aerospace photodiode from the original 1993 NIST calibration and from the recent 2015 calibration results.

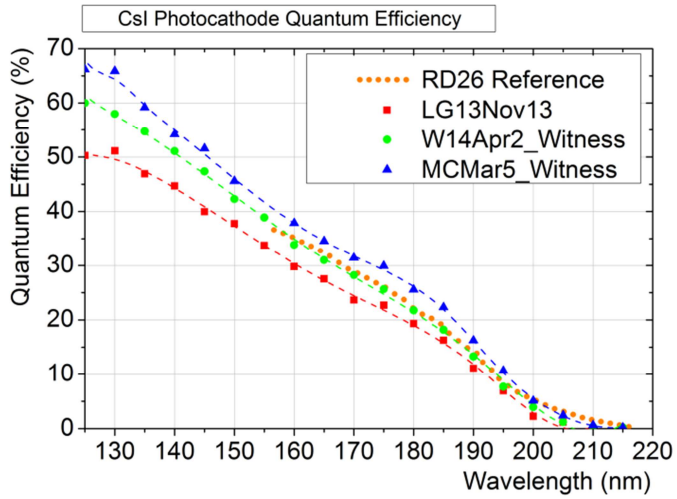

Figure 4.5 – Measured quantum efficiency of several CsI photocathodes as evaporated on freshly cleaned THGEM gold-plated electrodes. Also represented is the RD-26 reference.

Figure 4.5 shows the typical result of the quantum efficiency measurements for several CsI photocathodes we deposited on gold plated THGEM's. It was observed that for a wavelength of 175 nm the quantum efficiency usually ranged from 24% to 30%, decreasing for higher wavelengths: at a wavelength of 205 nm the quantum efficiency is already significantly reduced to ~1% – 3%. The measured quantum efficiency values compare very positively to the RD-26 Collaboration reference value also represented in Figure 4.5. The photocathodes used for these measurements were only exposed for a few seconds to air during installation in the vacuum monochromator.

Chapter 5 – Large area gas photomultiplier

5.1 Introduction

Large area THGEMs were manufactured by Eltos S.p.A. in Italy according to our designs and specifications. To accommodate the large area THGEMs a gas photomultiplier assembly was designed, assembled and tested. The design took into consideration the future application of a Triple- or Quadruple-THGEM detector with a segmented anode for position recording in the restricted space of the WiLIX cryogenic system. All the materials were selected keeping in mind their use in a high vacuum system so their outgassing should be minimal to avoid unwanted degradation of the CsI photocathode. The materials used were stainless steel 304L, oxygen-free high thermal conductivity copper (OFHC), polytetrafluoroethylene (PTFE or Teflon), Polyether-ether-ketone (PEEK), Kapton tape for insulation, FR4 on the electrodes and readout plane, and indium foil for thermal coupling of temperature sensors and heaters.

The selection of the operating gas mixture for the GPM was a compromise between permitting high photoelectron extraction efficiency from the photocathode at low fields and achieving high gains at relatively low voltages for the detection of single-photons and safe operation. A secondary consideration was that the mixture should be relatively fast and with small diffusion properties that would affect the localization accuracy. Calculations were performed that combined electrostatic simulations, based

on the available electrode geometries, and published data on the photoelectron extraction efficiency from CsI photocathodes into several Ne, Ar, CH_4 and CF_4 gases mixtures, in order to determine the mean photoelectron extraction efficiency for each of the geometries and each gas mixture, for each electrostatic condition applied.

5.2 Overall extraction efficiency calculation

The UV-detection efficiency, ε_{Det}, of a THGEM based GPM can be described as the probability of detecting an incoming photon as a GPM signal over the detector noise:

$$\varepsilon_{Det} = QE_{eff} * prob(signal > noise)$$

Since signal formation on the GPM is initiated by the conversion of a photon to a photoelectron on the photocathode this process is strongly dependent on the effective quantum efficiency, (QE_{eff}), of the CsI photocathode deposited on the first electrode as described by the following expression [**63**]:

$$QE_{eff} = QE \cdot A_{CsI} \cdot \varepsilon_{ext} \cdot \varepsilon_{col}$$

Where QE is the intrinsic quantum efficiency of the CsI photocathode's for the 175 nm wavelength, A_{CsI} is the fraction of the THGEM area covered by CsI, ε_{ext} is the extraction efficiency of photoelectrons into the gas mixture for a certain electric field value and ε_{col} is the photoelectron collection efficiency into the THGEM holes.

Through simulations it was found that, for null electric field above and below the THGEM electrode, the electric field on the surface of a THGEM electrode shows a strong dependence with the applied voltage difference between the top and bottom electrodes and with its geometrical parameters namely the distance between holes

(parameter “a”), the hole diameter (parameter “d”), its rim size (parameter “h”) and the thickness of THGEM (parameter “t”). In Figure 5.1 the geometrical parameters are shown:

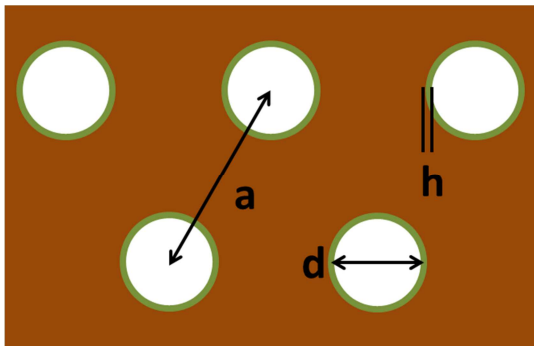

Figure 5.1 – Representation of the geometrical parameters used to define a specific THGEM.

Surprisingly, it was also found to depend on the thickness of the conductive cladding to a large extent. (This last parameter is not easily controllable since its thickness is dramatically reduced during the process of rim etching.). In Figure 5.2 is shown the calculation results, calculated using Maxwell software [**64**], for the electric field magnitude variation in the equidistant point to the center of three holes i.e. the minimum, for several rim sizes and cladding thicknesses. Each parameter was changed keeping the other parameter unchanged. The voltages, electrode thickness, hole pitch and hole diameter are fixed.

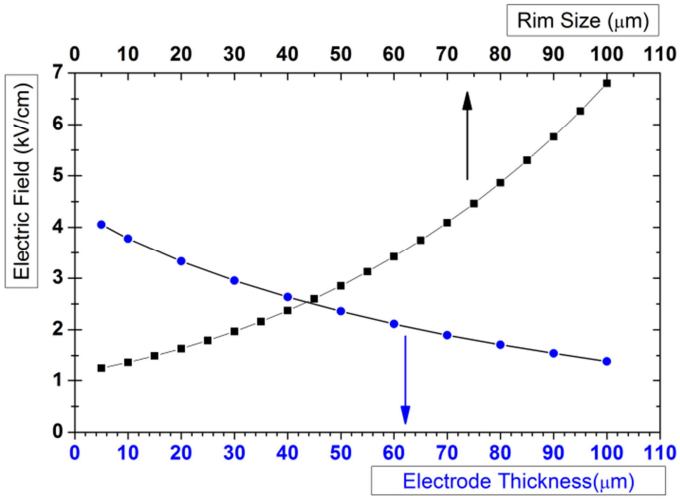

Figure 5.2 – Variation of the minimum electric field magnitude on the electrode surface varying the rim size and cladding thickness.

The calculation results show that an increase of the rim size leads to an increase of the magnitude of the minimum electric field on the electrode surface while an increase in cladding thickness leads to a reduction in the magnitude of the minimum electric field.

The electric field on the photocathode surface, as function of the voltage applied across the THGEM, was calculated using Maxwell software [**64**] in 2 μm resolution (see for example Figure 5.3), for the THGEM geometries available (**A** – pitch "a" = 0.8 mm; hole diameter "d" = 0.4 mm; thickness of the substrate "t" = 0.4 mm; rim around the hole "h" = 10 μm; thickness of the gold layer Au = 33 μm; **B** – a=0.8 mm; d=0.4 mm; t=0.4 mm; h=50 μm; Au=64 μm; **C** – a=0.7 mm; d=0.3 mm; t=0.4 mm; h=10 μm; Au=33 μm; **D** – a=0.7 mm; d=0.3 mm; t=0.4 mm; h=50 μm; Au=64 μm). The photoelectron extraction efficiencies from CsI into CH_4, CF_4, Ne/CF_4, Ne/CH_4 and Ar/CH_4 as function of the drift field in a parallel plate configuration, were simulated and

measured by several authors, using a UV lamp (185 nm peak) [**63**], [**65**], [**66**], and are shown in Figure 5.4 for convenience. The extraction efficiency, in each point of the photocathode surface, was estimated using the calculated electric field data and the data from Figure 5.4. The extraction efficiency for electric fields larger than the maximum electric field of the data from Figure 5.4 was done by extrapolation (taking 1 as the upper limit for extraction efficiency). The overall extraction efficiency for a given geometry and applied bias, was taken as the average of the extraction efficiency over all the points on the photocathode surface.

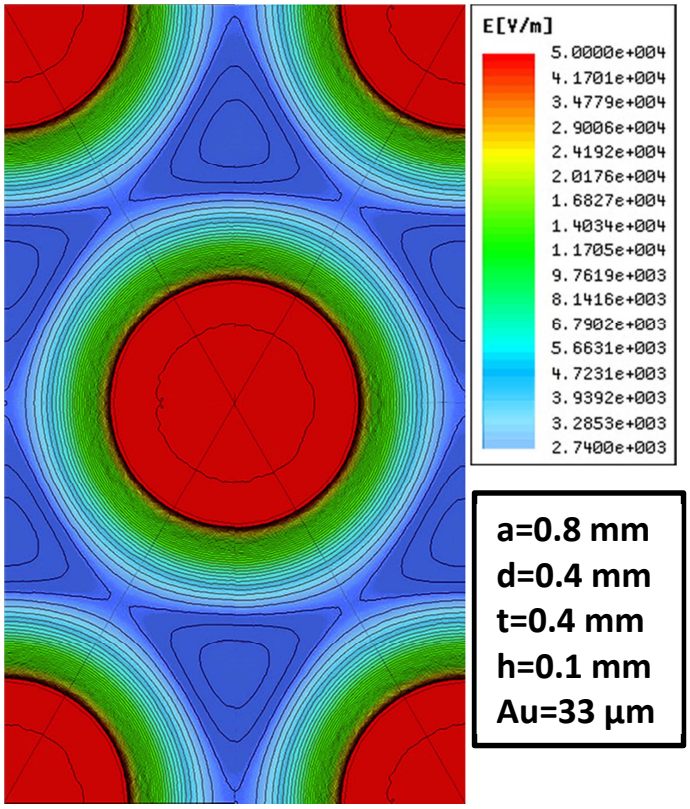

Figure 5.3 – Electric field intensity map on the THGEM surface for THGEM geometry: a=0.8 mm, d=0.4 mm, t=0.4 mm, h=0.1 µm and cladding thickness of 33 µm.

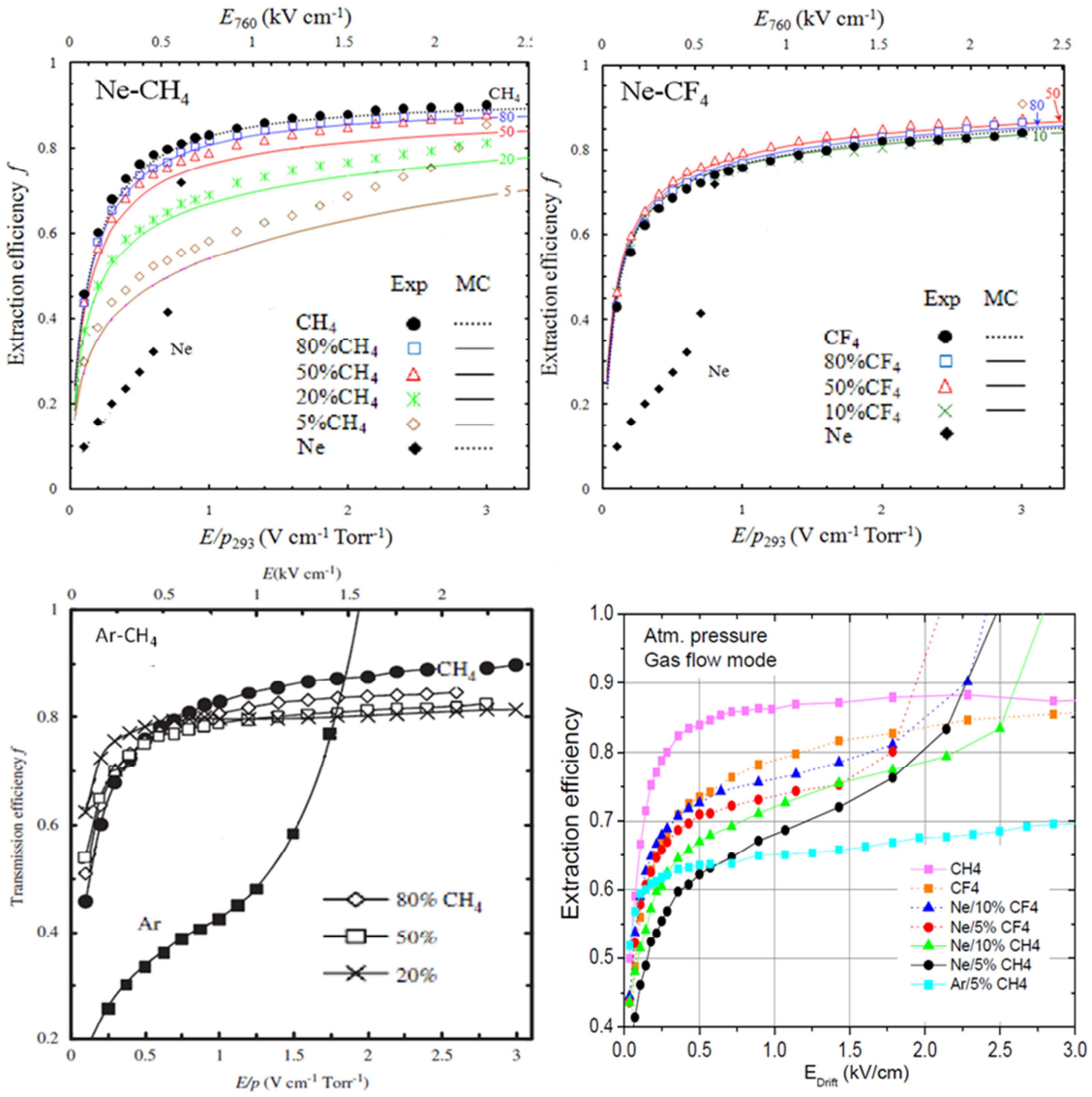

Figure 5.4 – Photoelectron extraction/transmission efficiency from CsI into various mixtures of CH_4, CF_4 with Ne and Ar as a function of the applied electric field using a UV lamp (185 nm), figures adapted from [**65**], [**66**] and [**63**].

The overall extraction efficiencies as a function of the electric field for Ne/CH_4, Ar/CH_4 and Ne/CF_4 for four gold coated-THGEM geometries are shown in Figure 5.5, Figure 5.6 and Figure 5.7, respectively. For geometry A, extraction efficiencies above

0.7 (and below 0.8) were estimated for Ne/CH_4 with CH_4 concentration >50% or Ne/CF_4 with CF_4 concentration >10% and voltages above 400 V. For Ar/CH_4, extraction efficiencies of ~0.8 were estimated for voltages above 400 V.

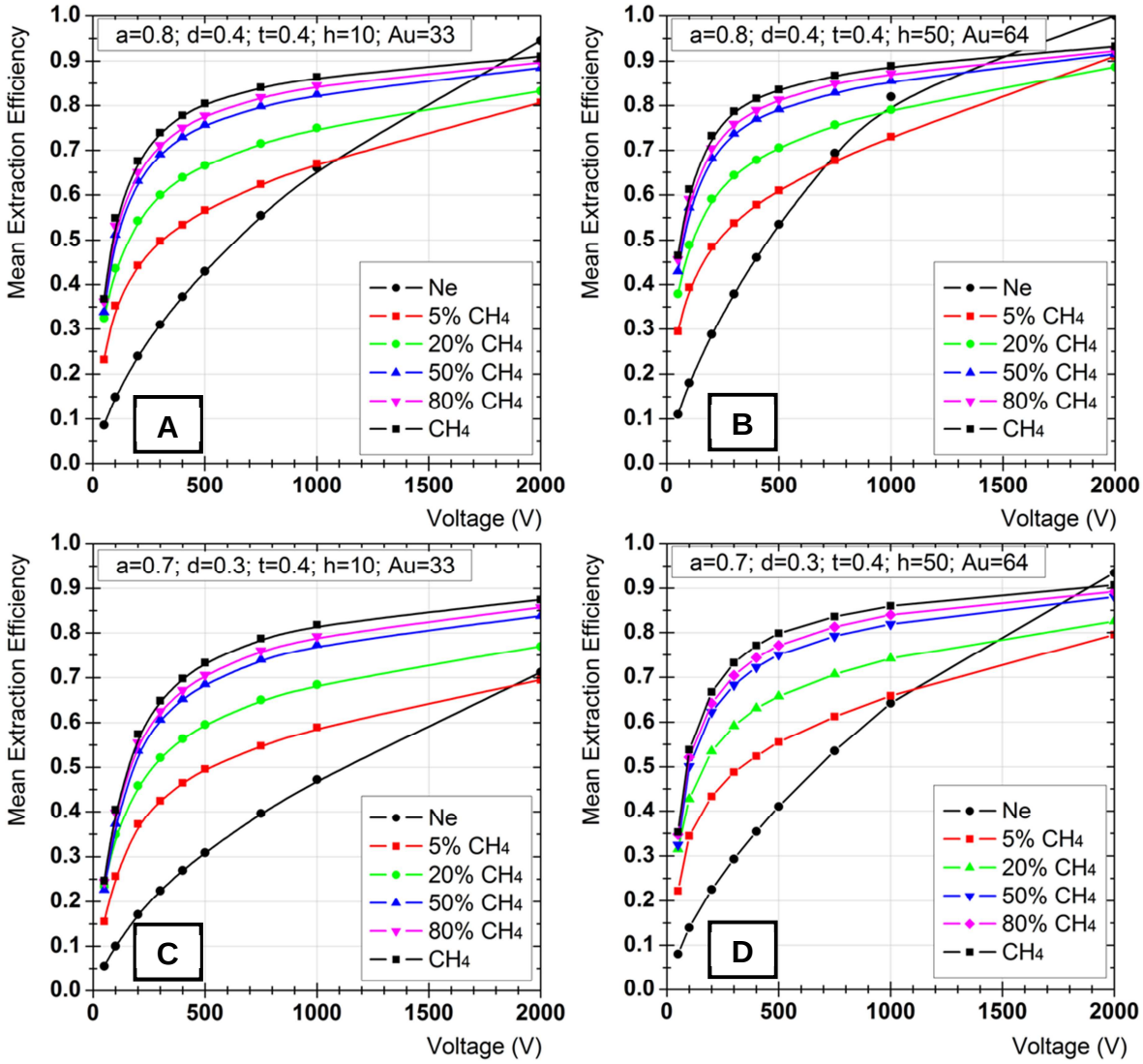

Figure 5.5 – The overall extraction efficiencies as a function of the electric field for Ne/CH_4, for four gold coated-THGEM geometries; A- a=0.8 mm; d1=0.4 mm; t=0.4 mm; h=10 µm; Au=33 µm; B- a=0.8 mm; d1=0.4 mm; t=0.4 mm; h=50 µm; Au=64 µm; C- a=0.7mm ; d1=0.3 mm; t=0.4 mm; h=10 µm; Au=33 µm; and D- a=0.7 mm; d1=0.3 mm; t=0.4m mm; h=50 µm; Au=64 µm.

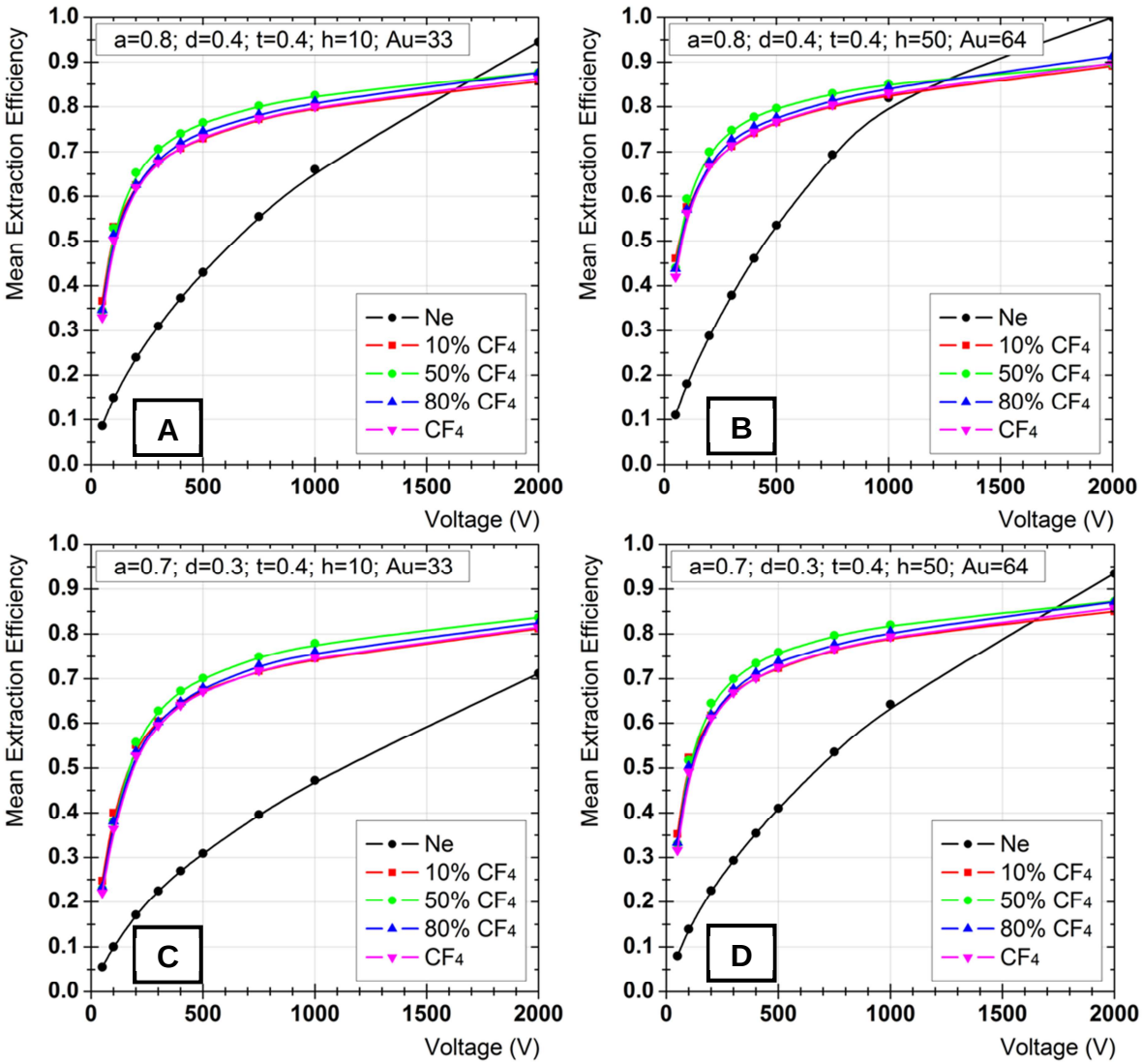

Figure 5.6 – The overall extraction efficiencies as a function of the electric field for Ne/CF_4, for four gold coated-THGEM geometries; A- a=0.8 mm; d1=0.4 mm; t=0.4 mm; h=10 µm; Au=33 µm; B- a=0.8 mm; d1=0.4 mm; t=0.4 mm; h=50 µm; Au=64 µm; C- a=0.7 mm; d1=0.3 mm; t=0.4 mm; h=10 µm; Au=33 µm; and D- a=0.7 mm; d1=0.3 mm; t=0.4 mm; h=50 µm; Au=64 µm.

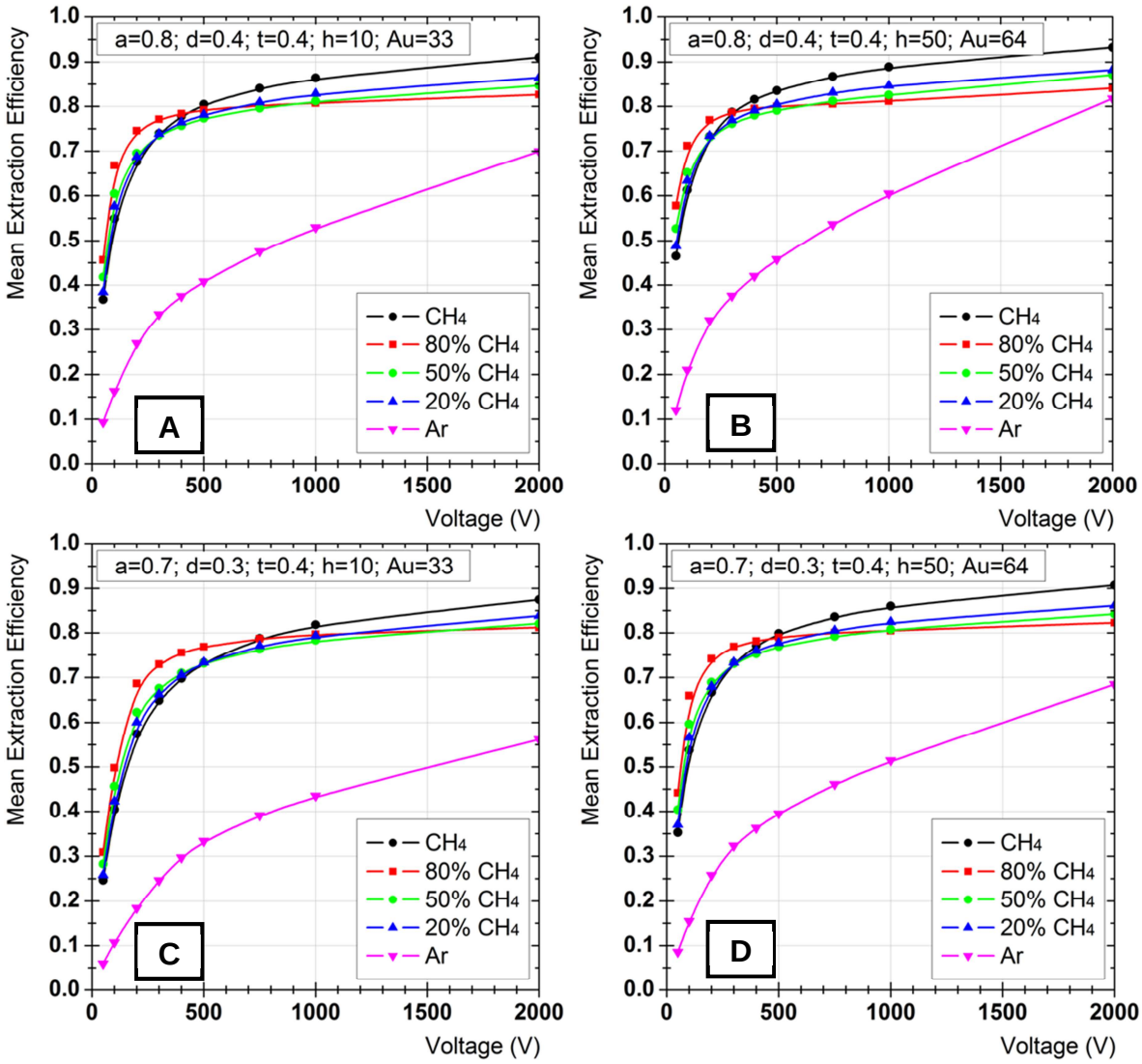

Figure 5.7 – The overall extraction efficiencies as a function of the electric field for Ar/CH_4, for four gold coated-THGEM geometries; A- a=0.8 mm; d1=0.4 mm; t=0.4 mm; h=10 µm; Au=33 µm; B- a=0.8 mm; d1=0.4 mm; t=0.4 mm; h=50 µm; Au=64 µm; C- a=0.7 mm; d1=0.3 mm; t=0.4 mm; h=10 µm; Au=33 µm; and D- a=0.7 mm; d1=0.3 mm; t=0.4 mm; h=50 µm; Au=64 µm.

It can be observed that enlarging the rim and the Au thickness increases the extraction efficiency by a few percent, for certain voltages (compare Figure 5.5A to B and Figure 5.5C to D). Reducing the pitch decreases the extraction efficiency by a few percent, for certain voltage (compare Figure 5.5A to C and B to D).

5.3 GPM description

The GPM was designed to be compatible with the Weizmann Institute Liquid Xenon – WILiX system (described in 3.3 and in [**67**]) for liquid xenon scintillation detection experiments. For preliminary tests a room temperature chamber was designed and built to accommodate the GPM and ancillary instrumentation. The general GPM structure is represented in Figure 5.8. It is composed by four or five circular THGEM electrodes with a diameter of 12.3 cm, the last of these being used as an anode for charge readout, with a fused silica viewport allowing UV photons to enter the detector space and impinge in the CsI photocathode. Photoelectrons extracted from the photocathode are drifted in the holes of the first THGEM, due to the effect of a dipole field, and multiplied by electron avalanche within the THGEMs holes due to the presence of a high electric field. The multiplied electrons are then extracted from the holes of the first THGEM, by application of lower electric field, and drifted towards the holes of the second THGEM where they are further multiplied. This process occurs a further one or two times, depending if the detector is operated with a triple stage or a four stage electron multiplier. Finally the electrons are drifted towards the readout electrode where they induce a current pulse which is then readout with our electronics.

In Figure 5.9 is represented the design of the THGEM electrodes with all of the dimensions highlighted. The actual active area is a circular region of 10.4 cm in

diameter, corresponding to an area of ~340 cm^2. For comparison, the active area of the largest vacuum devices available for cryogenic applications is ~182 cm^2, corresponding to the 3 inch devices – practically half of the active area of our detector.

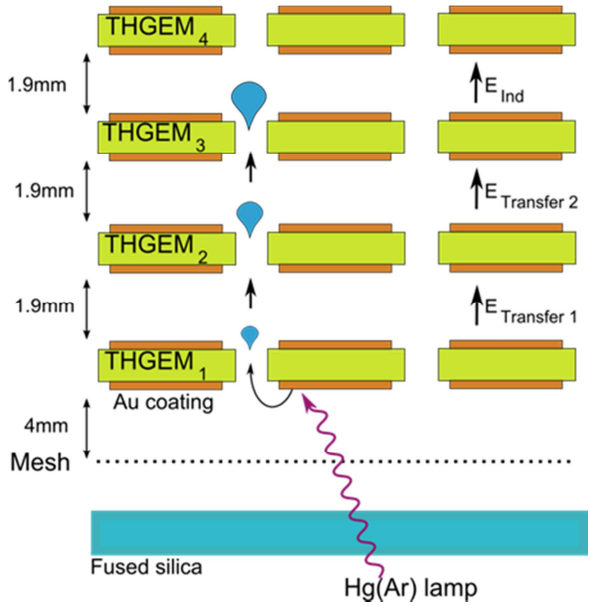

Figure 5.8 – Simplified schematic of the GPM assembly.

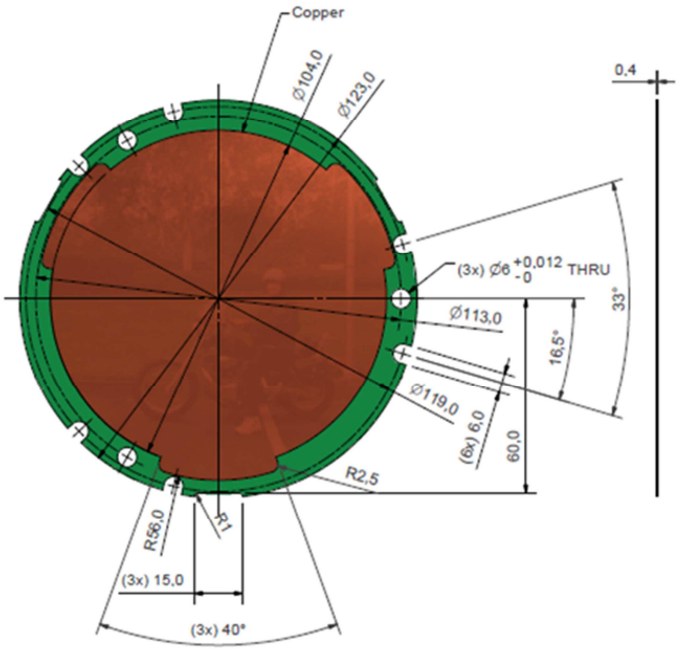

Figure 5.9 – Detail of the design of the large area THGEMs used in the GPM, highlighting all the dimensions.

5.3.1 Voltage, signal and gas feedthroughs

The GPM was designed with flexibility in mind. For that purpose a wide selection of electrical feedthroughs were installed: for high voltage biasing of a multi-structure detector eight 10 kV grounded SHV feedthroughs; for low voltage and signals six floating-shield BNC connectors and for temperature monitoring and control a multi-purpose Sub-D -Double-Ended 15 Pin connector. These feedthroughs and connectors were laser welded through a CNC machined 8" ConFlat blank flange represented in Figure 5.10. For counting gas and cooling N_2 circulation, four cryogenic fluid-feedthroughs were also installed via 1.33" ConFlat flanges terminated in ultra-high-vacuum ¼" VCR connections.

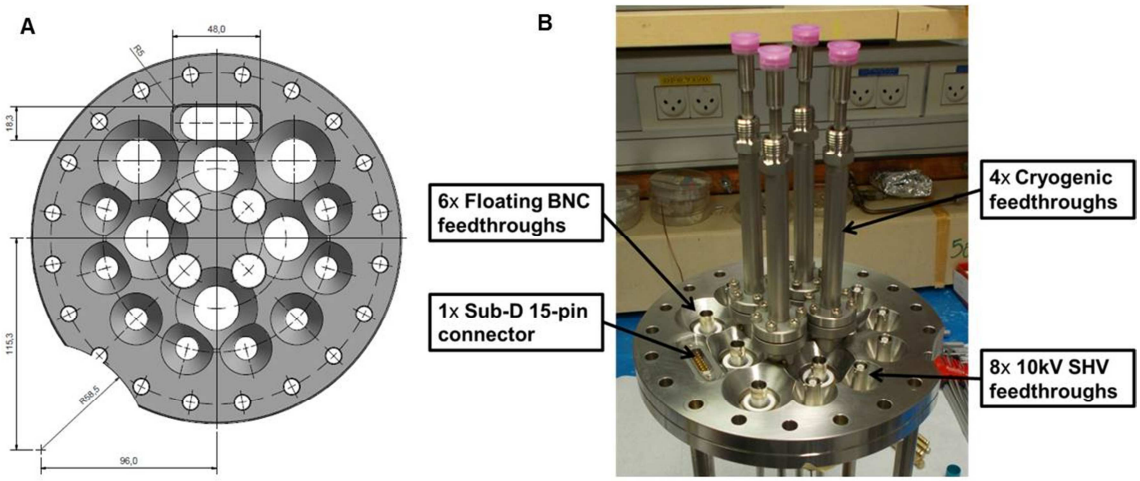

Figure 5.10 – A – Autodesk Inventor design for the CNC machining of the 8" CF flange and, B – Photograph of the machined 8" CF with the welded SHV, BNC, Sub-D feedthroughs and installed cryogenic gas feedthroughs.

After welding the feedthroughs and connectors, the whole assembly was thoroughly clean with petroleum-ether followed by isopropanol and leak tested with a Pfeiffer QualyTest HLT-270 He leak tester. The maximum leak rate observed over all the welds and connectors was a few times 10^{-11} mbar*l/sec.

5.3.2 Temperature monitor and control system

By design, the GPM assembly will inevitably feel a thermal gradient from ~300 K, on the top flange exposed to air, to ~180 K at the point closest to the LXe. The GPM will sit between these extremes. In order to ensure that the GPM will be close to thermal equilibrium with the LXe and that the incoming counting gas will not add a significant heat load while circulating, a temperature control system was designed to minimize the

thermal gradient on the GPM and to thermalize the incoming gas. Part of the system is shown in Figure 5.11. It consists in an OFHC copper block, onto which the GPM detector is assembled, machined in a way as to allow a cooling flow of cooled nitrogen vapor through it, while simultaneously cooling the counting gas flowing into the GPM volume, efficiently diffuse it near the THGEM electrodes and allowing the exhaust to the outside. The cooled nitrogen vapor circulates in a sealed spiral circuit within the bottom of copper block while the counting gas zigzags on the upper side before being released in the GPM volume through two openings, then returning through one exhaust to the outside, as shown in Figure 5.12. Top and bottom covers were welded to copper block and high vacuum stainless steel tubes were brazed to the gas ports that in turn connected to the four fluid feedthroughs on the top 8" CF flange via ¼" VCR connectors.

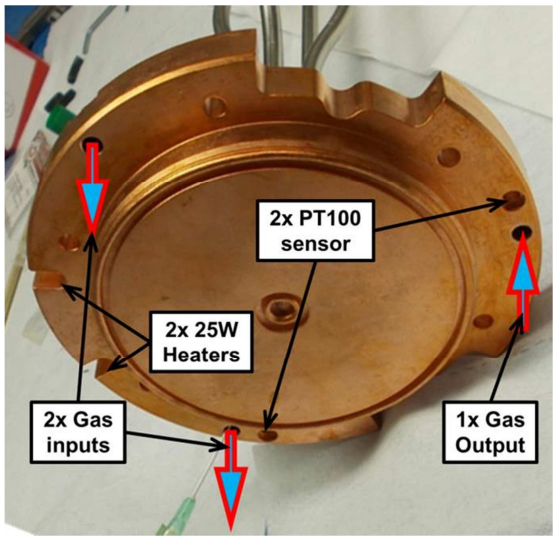

Figure 5.11 – Bottom view of the cooling copper block during leak testing after brazing and cleaning. The locations of the temperature sensors and heating cartridges are also visible.

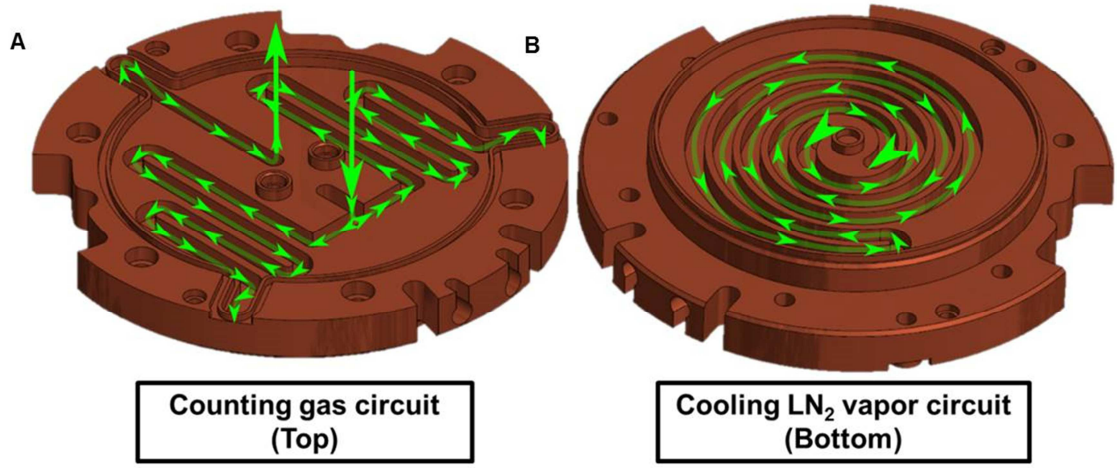

Figure 5.12 – Representation of the counting gas flow circuit (A, on the right) and LN_2 vapor cooling circuit (B, on the left).

A pair of Lakeshore PT-111 platinum resistance thermometers (PRTs) are installed in the copper block with a small amount of indium foil for thermal coupling, close to the gas input and output respectively, allowing to monitor the overall temperature of the copper block as well as any temperature gradient between the input and output gas lines. Each PRT is wired in a 4-wire connection method for high accuracy. To provide heating power, two 50 W cartridge heaters were installed inside the copper block, with indium foil for thermal coupling. Their high voltage connection wires were shielded with grounded silver-plated copper-braid to prevent RF emissions inside the GPM volume. The described sensors and cartridge heaters were connected to a Cryo-con 24C Cryogenic Temperature controller through the Sub-D Double-Ended 15 Pin connector. The Cryo-con 24C Cryogenic Temperature controller implements a Proportional-Integral-Derivative control response to the cartridge heaters as function of the measured temperature. The cooling power is provided by the vapor phase of a ~90 l LN_2 dewar, connected to the cooling base through a cryogenic hose.

5.3.3 Gas system

The GPM can be operated either in gas flow mode where gas composition and flow-rate are controlled via two MKS mass-flow controllers or in sealed mode where gas mixture composition is manually regulated. The schematic of the gas system for the GPM is represented in Figure 5.13, highlighting its major components. The gas system is provided with a vacuum pump (for initial gas filling), a nitrogen flushing line (for flushing during photocathode installation) and two mass-flow controllers (MFCs). The MFCs are calibrated and the maximum deviation was checked to be 1.4% full scale, at 200 sccm. The MFCs are connected to an MKS 247B controller where the appropriate gas correction factors are introduced to provide the correct flow rates of Ne, Ar, CH_4 or CF_4 for mixing. The gas mixture flows through an Entegris Gatekeeper model 35KF inert gas purifier which removes O_2, H_2, CO, CO_2, and H_2O to sub-ppb (parts-per-billion) levels. A control loop consisting of an MKS 250 Pressure/Flow controller, an MKS 121 pressure transducer (baratron) and an MKS 184J all-metal control valve maintained the gas pressure in the GPM at a slightly (~1.05 atm) higher value than atmospheric pressure. Prior to the introduction of gas, the GPM chamber is vacuum pumped down to ~10^{-6} torr with a turbo molecular pump. The gases used were research grade Ne N4.8 (Ne 99.998%), Ar 5.0 (99.999%) and CH4 M5.5 (CH4 99.9995%).

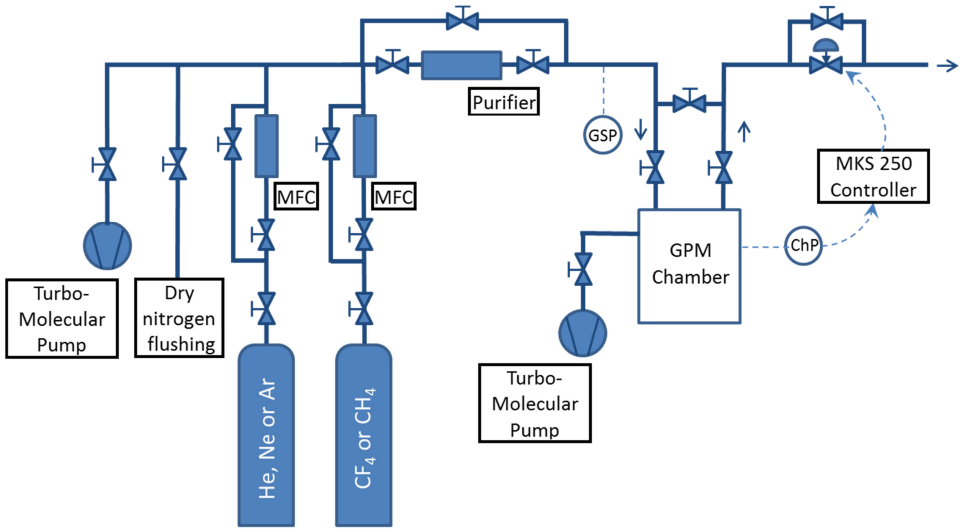

Figure 5.13 – Schematic of the gas GPM gas system.

5.4 Room temperature tests

The GPM detector for these set of experiments was composed by the copper cooling base, a PEEK support, five THGEMs and an electroformed copper mesh. The geometry of the THGEMs used were: 0.4 mm thick, 0.4 mm hole diameter, 0.8 mm pitch and 10 or 50 μm rim. The copper mesh (70 wires per inch with 90% transmission) was placed 3.9 mm away from the first THGEM. The transfer gaps between the THGEMs were set at 1.9 mm by PEEK spacers assembled on PEEK pillars to the PEEK support. The last THGEM ($THGEM_4$ in Figure 5.8) was used as a non-segmented anode by interconnecting the top and bottom electrodes. The distance between $THGEM_4$ and the PEEK support is 15 mm. Note that this anode will eventually be replaced by the 61pads segmented readout. A photograph of the assembled GPM detector can be seen in Figure 5.14.

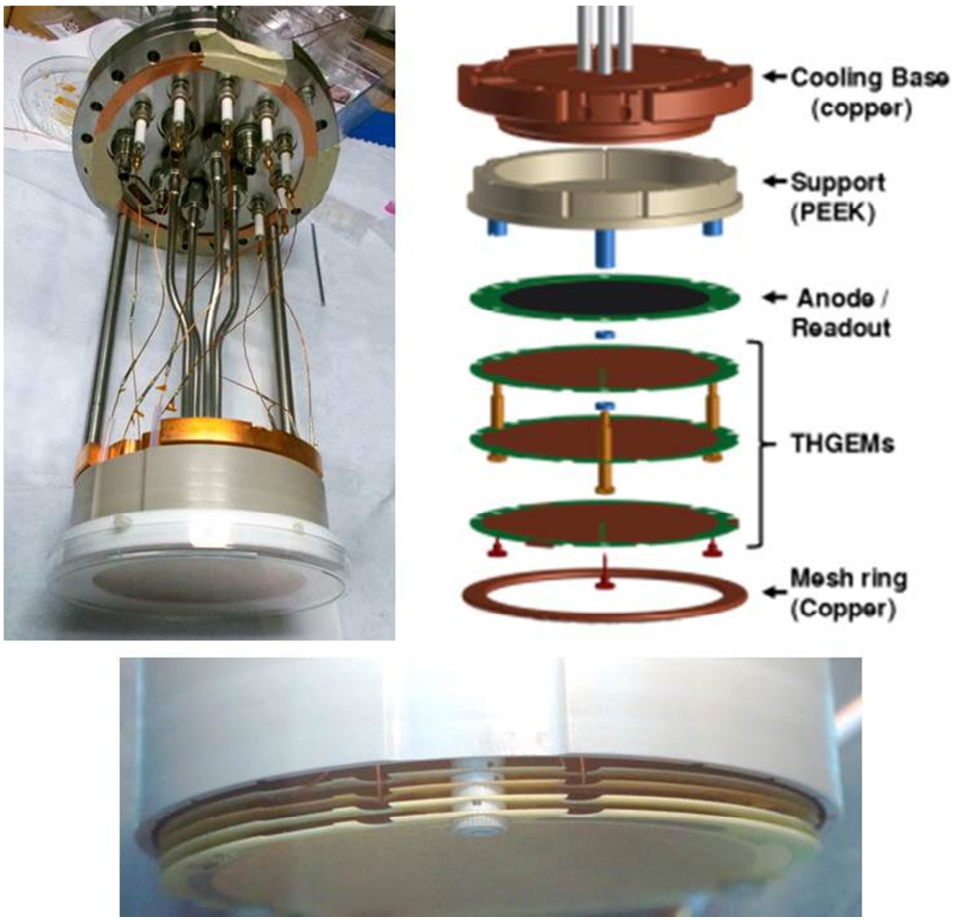

Figure 5.14 – Photograph of the assembled GPM detector on the copper cooling base ready to install. Petri dish on the front protects the mesh during transfer and is removed before installation.

5.4.1 Current mode measurements

Initial tests were performed without a CsI photocathode and an Oriel model 6035 Hg(Ar) lamp (peaking at 184.9 nm) powered by an Oriel model 6060 DC power supply was used to extract photoelectrons from the gold plated THGEM electrodes, before CsI evaporation. The photoelectrons were amplified in the THGEM holes due to electron

impact ionization. The current on the various electrodes was measured with a Keithley 610C electrometer. All THGEM electrodes were biased with independent CAEN N471A power supplies. The current measured on the last stage was normalized to the extraction current measured between the first THGEM and the mesh.

Results

In Figure 5.15 the gain measurement results obtained with the GPM at room temperature are represented for Single–, Double– and Triple–THGEM configurations in Ne/CH_4(95:5). The maximal gains shown correspond to the onset of discharges at a rate of approximately 1/min. One can see the increase in maximal gain from 3×10^3 to 4×10^5 to 4×10^6 in Single–, Double– and Triple–THGEM configurations, respectively.

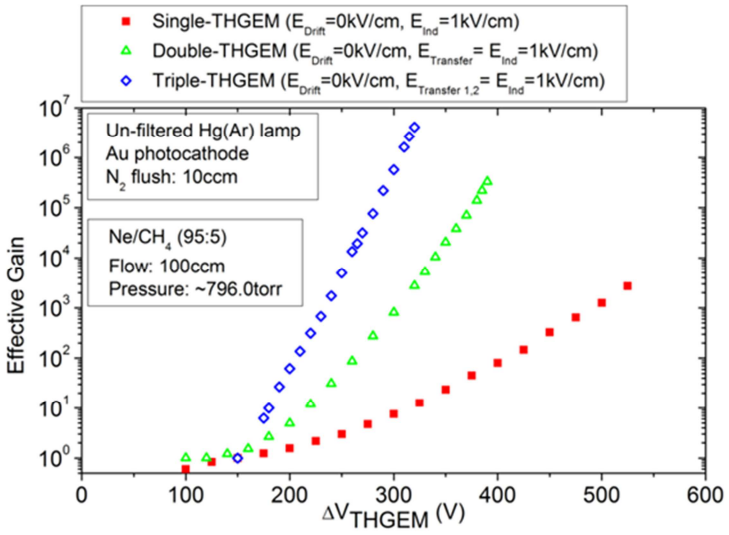

Figure 5.15 – Effective gain curves as a function of the voltage applied to each THGEM (ΔV_{THGEM}) measured in current mode for Single–, Double– and Triple–THGEM configurations in 796 torr of Ne/CH_4 (95:5).

5.4.2 Pulse mode measurements

For these tests a CsI photocathode was evaporated on the first THGEM electrode. The methods used for the cleaning of the electrode, for the photocathode evaporation and the transfer and installation of the electrode + photocathode were already described in Chapter 4. Using a strongly attenuated self-discharging flashed H_2 lamp (UV emissions peaking at 157.8 and 160.8 nm) and gating the acquisition chain with a trigger from the discharge lamp pickup it was possible to determine the detector gain with single photoelectrons. The light attenuation was done using a combination of Oriel UV neutral density filters and GEM foils in a way that only one out of four lamp pulses were accompanied by a GPM pulse – translating to a GPM pulse rate of approximately 15 Hz. The schematic of the electronic chains is represented in Figure 5.16. The GPM anode is connected to a Canberra 2006 charge sensitive preamplifier followed by an Ortec 572A linear amplifier and an AmpTek 8000A MCA. The acquisition of the MCA was set in coincidence with a trigger adapted from the pickup provided by the flashed lamp. For each lamp flash a strong signal was generated on a series attenuator. This signal was then provided to an Ortec 934 constant fraction discriminator followed by a CAEN N89 NIM-to-TTL converter followed by an Ortec 442 linear gate stretcher. The linear gate stretcher provided a TTL signal, formatted to be in coincidence with, and at least 1μs longer than, each detector pulse, which was fed to the coincidence input of the MCA gate. The charge pulses from the Canberra preamplifier were also visualized and recorded in an Agilent DSO-X 3034A oscilloscope.

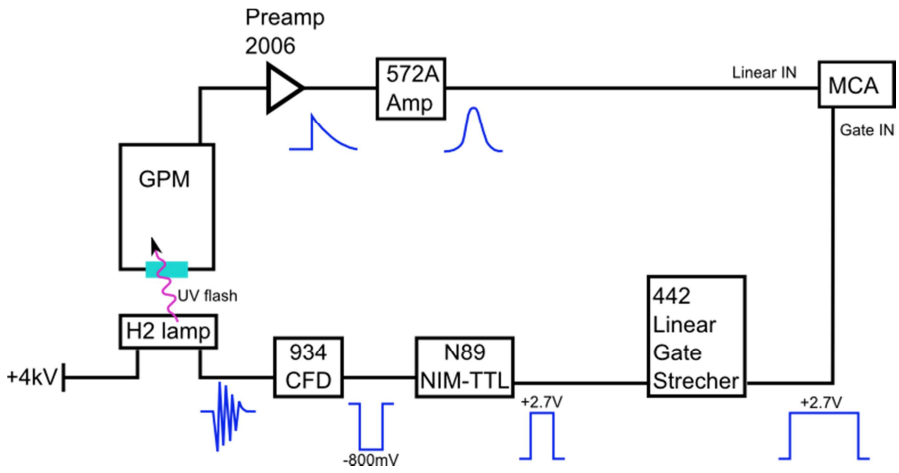

Figure 5.16 – Schematic of the electronic chain use for gain determination with a flashed H_2 lamp.

In order to determine the absolute effective gain of the GPM detector the charge sensitive pre-amplifier and the electronic chain were calibrated using the circuit shown in Figure 5.17. The test input provided in the preamplifier was not used in order to take into account the possible effects of the connections from the detector to the preamplifier, moreover, to be as close as possible to real measurement conditions, the same cables and connections were used (whenever possible). Instead an external calibration capacitor was used.

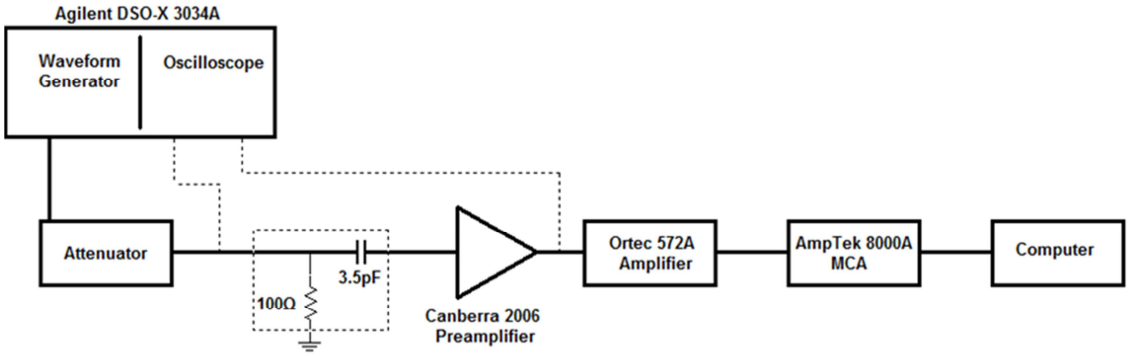

Figure 5.17 – Schematic of the setup used for charge calibration

The setup for calibration includes: 1) a wave form generator (internal module of Agilent DSO-X 3034A), 2) a variable attenuator Kay Electric Co. model 430B, 3) a standard calibration capacitor consisting of an encapsulated RC circuit with R=100 Ω and C_{calib}=3.5 pF for charge injection, 4) a Canberra 2006 charge sensitive pre-amplifier (S/N: 13000740), 5) an Ortec 572A linear amplifier and 6) an AmpTek 8000A multi-channel analyzer.

The waveform generator is connected to the input of the attenuator, providing exponential voltage pulses (variable amplitude, rise time of ~17 ns and decay time of ~3 ms, at a frequency of 75 Hz, with high impedance). The attenuator (50 Ω input impedance) provides discrete levels of attenuation from 10 to 51 dB and the signal output (V_{Calib}) is recorded by the Agilent DSO-X 3034A oscilloscope at 1 MΩ impedance, AC coupling. The signal is then introduced to the input of the calibration capacitor (C_{calib}), which in turn is connected to the input of the charge sensitive preamplifier through a length of cable equivalent to that used in the real detector, injecting a charge $Q_{calib}=C_{calib}V_{calib}$ in the preamplifier input – thus simulating charge pulses from the anode of the GPM.. The output of the charge sensitive preamplifier is recorded by the same oscilloscope at 1 MΩ impedance, AC coupling. The signal is then

connected to the input of the ORTEC 572A linear amplifier. The pulse from the linear amplifier is taken to the multi-channel analyzer and the pulse-height spectrum is saved and the peak position is determined.

For several values of V_{calib} (hence several values of Q_{calib}) the centroid of the corresponding channel in the pulse-height spectrum is taken. In this way a calibration curve of the amount of charge, n_{charge}, versus MCA channel, *ch*, can be determined:

$$n = {Q_{calib}}/{q_{electron}} = {C_{calib} \times V_{calib}}/{q_{electron}} = a \times ch + b$$

Where $q_{elecron}$ is the elementary electron charge or 1.602×10^{-19}C.

For each detector voltage configuration the obtained pulse-height spectrum was then fitted to an exponential distribution:

$$Q = A * e^{-\frac{x}{c}}$$

In Figure 5.18 is represented a typical single photoelectron spectrum obtained with the GPM in a Triple-THGEM configuration. Also represented on the same image is an exponential fit to the data points. The voltages applied were V_{Mesh}=V_{Top1}=-3250 V, $V_{Bottom1}$=-2300 V, V_{Top2}=-2100 V, $V_{Bottom2}$=-1250 V, V_{Top3}=-1050V, $V_{Bottom3}$=-200 V, corresponding to ΔV_{THGEM1}=950 V, ΔV_{THGEM2}= ΔV_{THGEM3}=850 V and $E_{Transfer1}$= $E_{Transfer2}$= $E_{Induction}$=1 kV/cm. From the fit it can be determined that the mean charge of the distribution is ~16.4 ± 0.1 fC, corresponding to a detector gain of $\sim1\times10^{5}$. The selection of an asymmetric voltage distribution across the stages of the GPM serves to maximize the voltage on the first stage electrode – the electrode with the evaporated photocathode – hence maximizing the photoelectron extraction efficiency.

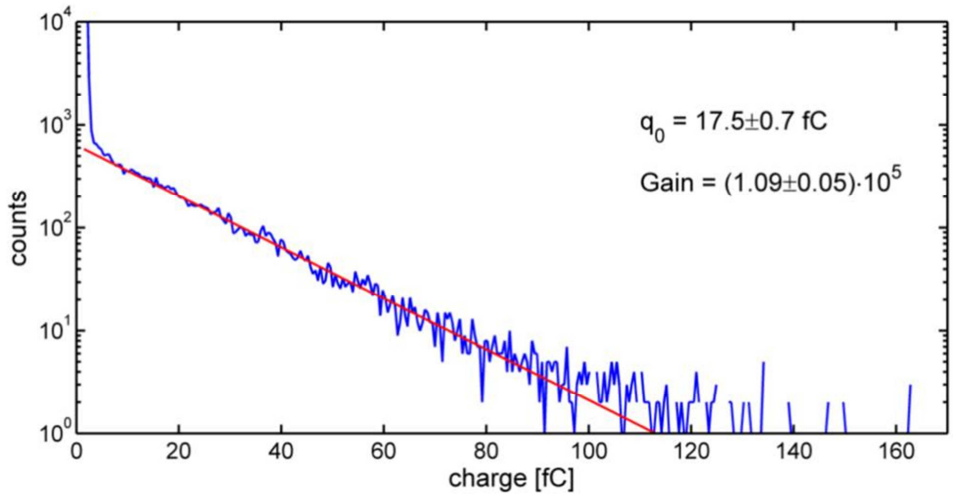

Figure 5.18 – Typical single-photoelectron spectrum operating obtained with the Triple–THGEM GPM configuration in ~1.1 bar of Ne/CH_4(80:20)

Results

In Figure 5.19 are represented the charge gain results obtained with a Triple– and Quad–THGEM GPM at room temperature with single–photoelectrons extracted from the CsI photocathode with the H_2 flashed lamp in ~600 torr of Ne/CH_4(80:20) gas mixture. The maximal gains correspond to the appearance of discharges at a rate of about 1/min. The voltage division across the stages was set asymmetrically in order to maximize the extraction efficiency on the first stage between 1000 V and 850 V, for Triple– and Quad–THGEM setups, respectively. The maximal gains recorded were ~3×10^5 and ~1×10^6, for Triple– and Quad–THGEM setups, respectively.

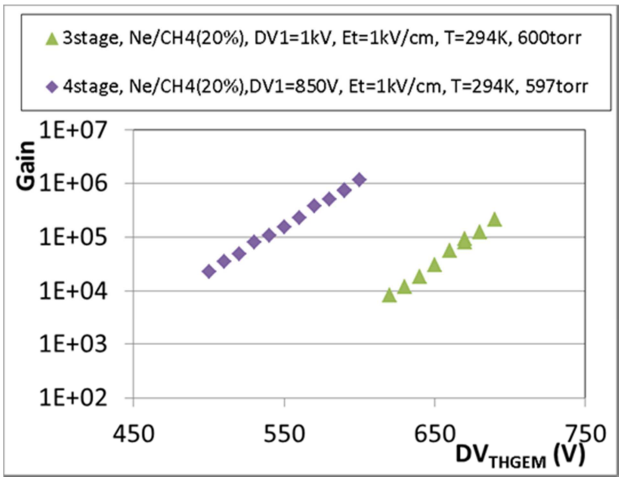

Figure 5.19 – Gain measurement as a function of the voltage difference applied to the THGEMs of the cascade, except the first, for a Triple– and Quad–THGEM GPM configuration in Ne/CH_4(80:20), using single-photoelectrons from a flashed H_2 lamp at room temperature.

5.5 Cryogenic characterization

The GPM assembly was installed in the central shaft of WILiX, as shown in Figure 5.20, above a UV transparent window with a 35.6 mm clear aperture (MPF A0650-2-CF, with Corning HPFS 7980 fused silica). The window transmission was measured to be 90% at 175 nm. The GPM prototype investigated in this work, shown in detail in Figure 5.14, comprised a cascaded structure of three THGEMs with a pitch of 0.8 mm between the hole-centers, hole-diameter of 0.4 mm and the width of the etched rims was 50 μm. The Cu layer thickness (after etching) was 64 μm. The transfer gaps between the stages, as well as the induction gap between the third THGEM and readout plane were 2 mm wide. The readout plane (anode) was a whole, un-segmented unit. An electro-formed Cu mesh with 85% transparency (Precision Eforming, MC17)

was set 3 mm below the first amplification stage and kept at the same potential as the CsI-coated face of the first THGEM, to maximize the extraction efficiency of electrons from the reflective CsI photocathode: since the field at the photocathode surface is the combination of the electric field due to the potential applied between the two THGEM faces and the drift field, when the drift field is negative (pointing toward the photocathode), the mesh, being more positive than the THGEM photocathode, collects part of the photoelectrons, which are then lost. On the other hand, when the drift field is positive (oriented toward the wire cathode), the resulting field at the photocathode surface is reduced, and so is the probability of photoelectron extraction. For zero drift field all electron trajectories enter the THGEM holes [**68**] and [**69**]. HV bias to each electrode was done through low-pass filters with a cutoff frequency of ~5Hz, using a CAEN N1471H power supply. The signal was taken from the readout plane on a coaxial cable (inside the GPM chamber), to a Canberra 2006 charge sensitive preamplifier connected on the outer side of the top flange of the GPM chamber.

For these experiments several mixtures of neon and methane were used: Ne/CH_4(5%), Ne/CH_4(10%) and Ne/CH_4(20%). Most of the data were taken at a pressure of 0.7 bar (~500 torr), which at 180K corresponds to roughly the same gas density as in 1.1 bar (~800 torr) at room temperature. Even though the GPM gas system allows operation in gas-flow mode, it was decided to begin the study with the detector operating as a sealed device.

For this study the WILiX cryostat was used to house a small dual-phase TPC at its center (Figure 5.20 and Figure 5.21). Two electro-formed Cu meshes with 85% transparency (Precision Eforming, MC17), set 5 mm apart, were used as the TPC anode and gate - bounding the liquid-gas interface from above and below, respectively. The liquid level was controlled by a movable level controller (not shown in the figure). An 18 mm diameter stainless steel disc, serving both as the TPC cathode and as an alpha

particle source, was held 5 mm below the gate mesh. The disc carried a central oval active spot of 80 Bq ^{241}Am, roughly 8×5 mm^2 in size. Prior to the experiments, the source was tested in liquid nitrogen, showing no loss of activity in repeated thermal cycles.

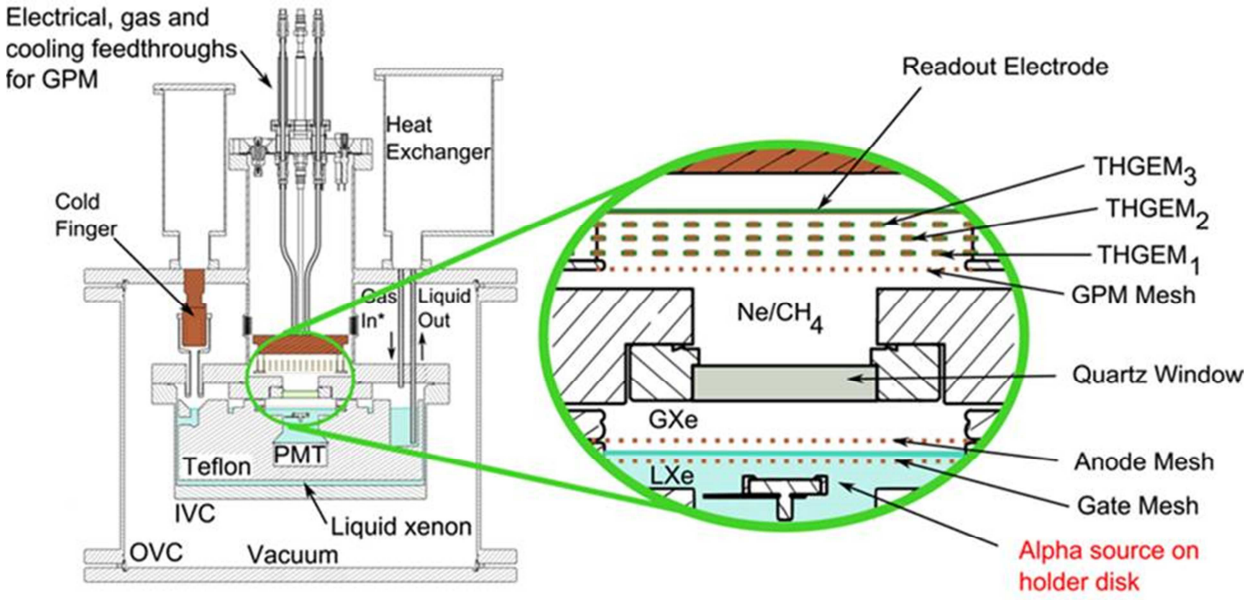

Figure 5.20 – Schematic of the TPC and Triple-THGEM GPM. The main elements are highlighted like the alpha source, gate and anode mesh, the quartz window and the components of the GPM.

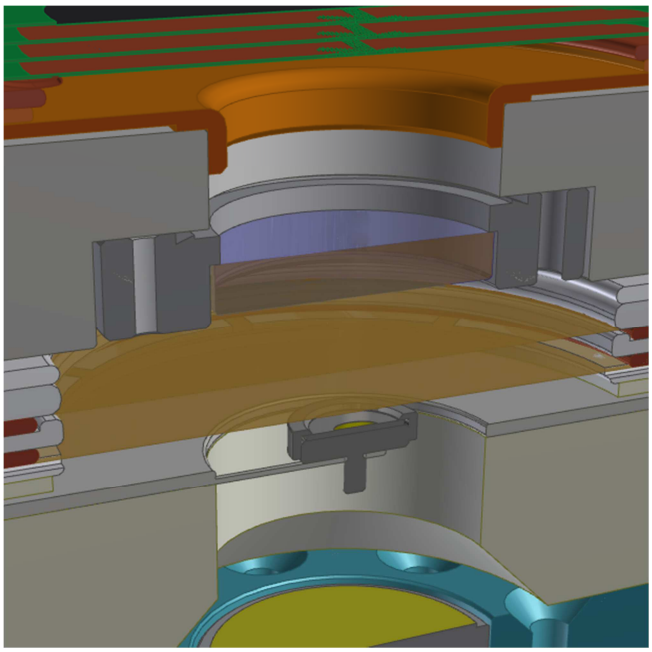

Figure 5.21 – Interior 3D schematic of the WILiX – TPC. The PMT can be seen at the bottom and the Triple-THGEM GPM at the top separated by the quartz window.

The TPC voltages, set by a CAEN N1471H power supply, were −3kV for the cathode/source, −2.5 kV for the gate and +2 kV for the anode, defining a drift field of 1 kV/cm and a nominal extraction field of ~12 kV/cm in the gas phase (assuming the liquid-gas interface lies half-way between the meshes). Alpha emissions from the source are stopped within ~40 μm in the liquid producing prompt S1, primary scintillation light signals, and primary ionization electrons. The primary electrons that escape recombination due the applied electric drift field on the TPC are drifted towards the gate mesh and extracted through the liquid/gas xenon interface into the gas phase. There, due to the high electric field between the liquid surface and anode mesh (~12 kV/cm), the electrons produce secondary electroluminescence (S2), appearing 2.4 μs later, depending on the TPC drift field. A 1” square PMT (Hamamatsu R8520-06-Al), located 3.5 cm below the top surface of the source, was used to record reflected S1 and S2

photons (the source disc holder was mounted on a stainless steel structure with wide openings to allow reflected photons to reach the bottom PMT). Throughout the experiment the xenon pressure in the TPC was ~1.8 bar and the recirculation flow through the purifier was about 3 standard liters per minute.

5.5.1 S1 and S2 GPM signals

At adequate electric fields in the LXe TPC, alpha-particle induced S1 and S2 signal pairs were observed on the GPM anode, starting at gains of ~10^3. For a drift field of 1 kV/cm and nominal extraction field of 12 kV/cm in the gas phase, S_2 signals appeared ~2.4 μs after S1, as expected based on the known drift velocity of electrons in liquid xenon [**46**] [**70**]. The ratio of S2 to S1 pulse areas measured by the PMT was ~25 (the PMT signal was used as direct input to the oscilloscope without amplification and shaping; the pulse area was therefore proportional to the number of photoelectrons). Figure 5.22 shows a typical signal of the charge sensitive preamplifier (CSP) connected to the GPM anode, along with the corresponding PMT signal for the same event. In this particular case the GPM was operated with Ne/CH_4(10%) at a pressure of 1.05 bar at ~190 K. The voltage across THGEM1 was 1250 V, with 1050 V across THGEMs 2 and 3 (overall gain of ~1×10^5); the transfer and induction fields were 0.5 kV/cm.

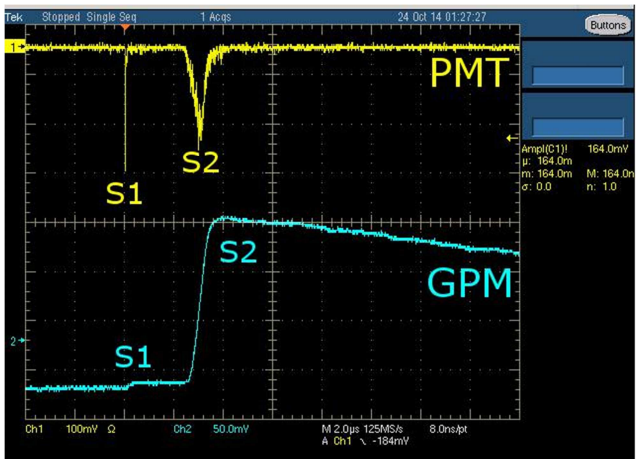

Figure 5.22 – Typical S1 and S2 signals from the PMT and GPM (the latter – through a charge sensitive preamplifier). The GPM was operated here with Ne/CH_4 (10%) at 1.05 bar and 190 ± 1K, at a gain of ~1×10^5. The vertical scales are 100 mV/div for the top signal and 50 mV/div for the bottom scale, while the horizontal scale is 2 μs/div.

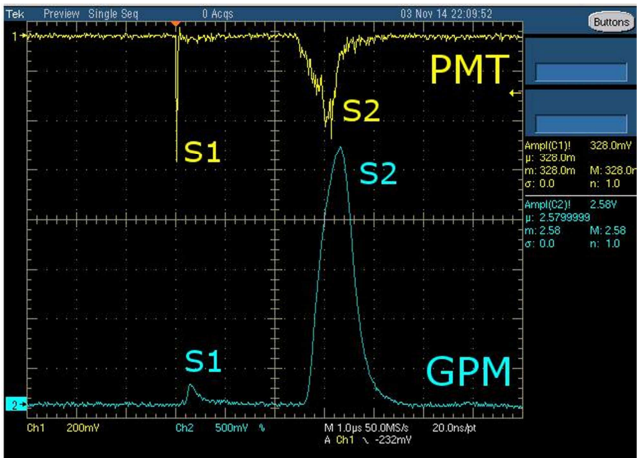

Figure 5.23 – Typical S1 and S2 signals from the PMT and the GPM (the latter – through a timing filter amplifier). The GPM was operated here with Ne/CH_4 (5%) at 0.7 bar and 180 ± 1K, at a gain of ~1×10^5. The vertical scales are 200 mV/div for the top signal and 500 mV/div for the bottom scale, while the horizontal scale is 1 μs/div.

Figure 5.23 shows an example of the GPM signal where the CSP output was processed by the timing filter amplifier (ORTEC 474), with integration and differentiation time constants of 20 ns and 100 ns, respectively. This particular image was taken with the GPM operated with Ne/CH_4 (5%) at 0.7 bar and ~180 K. The voltage across THGEM1 was 700 V, with 430 V across THGEMs 2 and 3 (gain ~1×10^5); the transfer and induction fields were all 1 kV/cm.

5.5.2 GPM gain and stability

A GPM deployed within an array of photosensors in a dual-phase noble-liquid DM detector should have a large dynamic range; it should be capable of consistently recording both single S1 photons with high detection efficiency and S2 signals comprising thousands of photoelectrons with minimum discharges. The GPM gain plays a key role in its detection efficiency: for example, a gain of 1×10^5 should permit >90% detection of single-photoelectron signals above noise for front-end electronics with a moderate noise level of ~1 fC (~6,000 e-). For a noise level of ~1000 e-, a gain of ~3×10^4 would permit ~95% detection efficiency at the level of a 3σ cut, as shown, for example, for a quintuple-GEM prototype in [**71**].

Gain measurements were performed by shining a deuterium UV lamp through a fused silica window near the top of the GPM port. The lamp provided single UV photons at a rate of a few hundred Hz that reached the CsI photocathode by reflection. The gain was estimated by fitting an exponential function to the pulse height distribution of these photons, as shown in Figure 5.18. The position of the GPM S1 peak due to alpha particle scintillation was also recorded on the multichannel analyzer (MCA), serving as a complementary handle to find relative changes in the gain; in

particular, this allowed estimating the gain at low GPM voltages, where the exponential fit was no longer possible because of noise limitations in the present setup. During gain measurements the TPC voltages were set to zero, thus preventing the formation of S2 and leaving only alpha-induced S1 signals at a rate of 40 Hz. The typical amplitude of the S1 pulses was much larger than that of the single-photon signals, and thus did not affect the single-photoelectron pulse-height distribution.

During gain measurements the TPC voltages were set to zero, thus canceling contributions from S2 signals and leaving only S1 alpha particle signals with a rate of 40Hz. The typical amplitude of these pulses was considerably larger than those of the single-photon signals induced by the lamp, and thus did not affect the single-photoelectron pulse height distribution.

The detector gain (Figure 5.24) depended on the gas composition, with lower voltages required for smaller admixtures of methane for a given gas-multiplication value. The maximum gain obtained at 0.7 bar and 180 K was ~8×10^5 for Ne/CH_4 (5%) and ~3×10^5 for Ne/CH_4(20%); increasing the voltages to higher values resulted in occasional discharges. For both gas mixtures, “asymmetric” THGEM polarization (with higher voltage across THGEM1) proved to be more stable, as shown in Figure 5.24A. Thus, for Ne/CH_4(5%), 700 V were applied on the first stage with 400 – 495 V on the second and third, while for Ne/CH_4 (20%) the voltage on the first stage was set to 1000 V, with 660-820 V on the second and third. The transfer and induction fields in both cases were all 1 kV/cm. While operating with the TPC voltages on, and thus with S2 signals, the maximal stable gain was lower by a factor of ~2-3 for both gas mixtures. With Ne/CH_4 (5%) at a gain of 1×10^5 and alpha-particle S_2 signals at 40 Hz, the discharge probability was found to be of the order of 10^{-6}. We note that in addition to the alpha particle S_2 signals (resulting in a few thousand photoelectrons on the GPM), there

were ~20-30 cosmic rays per minute crossing the TPC; these deposited charges resulted in S2 signals up to ~100 times larger than those induced by the alpha particles.

Figure 5.24B shows two gain measurements performed with Ne/CH_4 (20%) under similar conditions (0.7 bar, ~190 K) over a period of two months. During this entire time interval, the detector operated in a sealed mode, i.e., with no exchange of the gas. The two curves are consistent to within 7-15% over the range of overlapping voltages, with the higher values obtained in the second measurement (for which the onset of occasional discharges occurred at a lower gain). The results of the two measurements were consistent for both the D_2 lamp and alpha S1 signals, indicating that there were no significant changes in either the gas composition or the CsI QE between them.

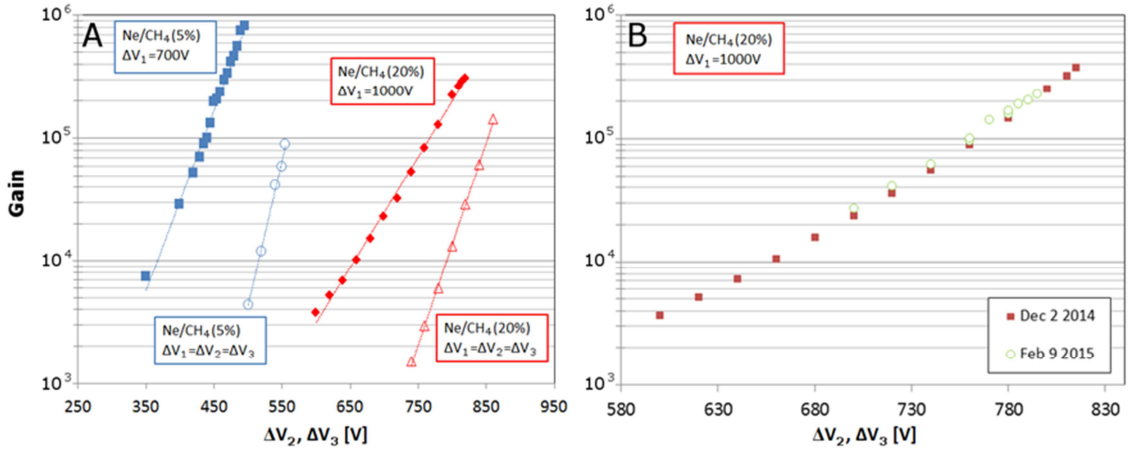

Figure 5.24 – (A) Gain curves for symmetric and asymmetric voltage divisions in Ne/CH_4(5%) and Ne/CH_4(20%) at 0.7 bar and 180 K vs. the equal voltages on the second and third THGEMs ($\Delta V_{2,3}$); in the asymmetric cases the voltage across THGEM1 (ΔV_1) was kept at a fixed value: 700 V for Ne/CH_4(5%) and 1000V for Ne/CH_4(20%). (B) Gain curves recorded within two months of each other with Ne/CH_4(20%) at 0.7 bar and ~190 K with the detector operated in sealed mode.

5.5.3 Energy resolution

Figure 5.25 shows the GPM pulse height distributions of alpha particle-induced S1 and S2 signals. The detector was operated with Ne/CH_4 (5%) at 0.7 bar and 180 K; the voltages were ΔV_1=700 V and $\Delta V_{2,3}$=430 V and the transfer and induction fields were 1 kV/cm, with a resulting gain of 1×10^5. For S1 a RMS resolution of σ/E=10.9% was derived (by fitting a Gaussian to the entire S1 peak). For S2, the asymmetric shape of the spectrum reflects the coincidence of alpha and 59.5 keV gamma emissions from the source, and a Gaussian fit to the left side of the peak gives σ/E=8.7%. Note that in the S2 spectrum one can clearly see the 59.5 keV peak, for events in which the alpha particle is emitted into the source holder and the correlated gamma is emitted into the liquid. The ratio of alpha to the 59.5 keV gamma S2 peaks (~5.7) is consistent with the

different charge yields from their respective tracks in LXe [**72**]. The S2 resolution recorded here is comparable to that obtained in XENON100 with PMTs (there σ/E=10.0 ± 1.5%), for a similar number of ionization electrons (~8000) entering the gas phase [**73**].

The S1 RMS resolution can serve as an independent estimate for the detection efficiency of the GPM prototype of this study. The argument relies on a comparison between the expected number of photoelectrons N_{pe} and a lower bound on N_{pe} derived from the observed S1 resolution. The number of photoelectrons in an alpha particle S1 signal can be estimated as follows. Since the average ^{241}Am alpha particle energy is 5.5 MeV and the average energy required to produce one VUV photon in an alpha particle track is ~18 eV [**48**] and [**72**], the number of photons emitted into 4π is ~3×10^5. Considering the geometry of the setup, and applying Snell's law on the liquid-gas interface, only 1.7% of these photons are emitted into the solid angle that may allow them to reach the GPM window. With Fresnel reflection (5%) from the interface and the measured transmission of the three electroformed meshes (85%) and fused silica window (90% at 175 nm), the number of photons reaching the first THGEM is thus ~2700. The number of resulting photoelectrons is determined by the effective *QE* given by [**63**], as discussed previously in chapter 5.2:

$$QE_{eff} = QE \cdot A_{CsI} \cdot \varepsilon_{ext} \cdot \varepsilon_{col}$$

Where A_{CsI} is the fraction of THGEM area covered with CsI (0.77 in the present geometry, including the rims), ε_{ext} is the overall extraction efficiency (~0.6 for this geometry, gas mixture, pressure and voltage – see Chapter 5.2 above) and ε_{col} is the collection efficiency, assumed to be 1 under the present condition [**63**].

For a nominal *QE* of 25% at 175 nm [**74**] [**52**] we have that QE_{eff} = 11.5% (for Ne/CH_4(20%) the nominal effective QE for the present geometry is ~14% as discussed

below). With these values, the nominal number of photoelectrons for an alpha S1 signal is $N_{pe} \approx 2700 * 0.115 = 310$.

A lower bound on the actual value of N_{pe} can be obtained from the measured S1 RMS resolution. Considering only the statistical fluctuation in N_{pe} and detector gain:

$$\frac{\sigma}{E} > \frac{1}{\sqrt{N_{pe}}}\left(1 + \left(\frac{\sigma_M}{M}\right)^2\right)^{1/2}$$

where M is the average single-photoelectron avalanche size and σ_M is its standard deviation. For an exponential single-photoelectron pulse height distribution $\sigma_M = M$ and thus the lower bound on the RMS resolution becomes $\sigma/E > \sqrt{2/N_{pe}}$. Here, with σ/E =0.109, we find $N_{pe} \gtrsim 170$. In terms of the effective quantum efficiency, this gives QE_{eff} > 6.2% (QE > 14%). We note that additional effects can contribute to the observed S1 RMS resolution, including, in particular VUV light scattering on the liquid-gas interface (which is difficult to quantify); thus the actual values of N_{pe} and QE_{eff} in the present experiment were likely considerably higher than their respective lower bounds.

Since the observed ratio S2/S1 was ~25, a lower bound on the average number of S2 photoelectrons is N_{pe} $(S_2) \gtrsim 170 * 25 = 4250$ (the upper bound is ~7800). Using the same consideration this gives $\sigma/E > 2.2\%$. The fact that the observed value is 8.7% suggests that the S2 RMS resolution is governed by fluctuations in the secondary scintillation process in the xenon gas phase, likely because of ripples in the liquid-gas interface.

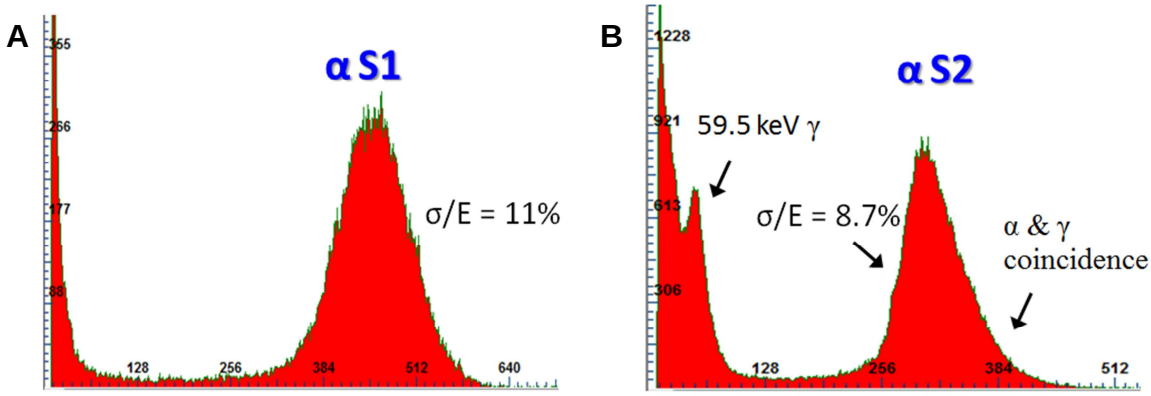

Figure 5.25 – S1 (A) and S2 (B) spectra and their associated RMS resolution, recorded with the GPM operated with Ne/CH_4(5%) at a gain of 1×10^5 at 0.7 bar and 180 K.

5.5.4 GPM time resolution

The time delay between the moment of photoelectron emission from the GPM's CsI photocathode (here deduced from the S1 PMT signal) and the signal formation on the GPM's anode depends on the gas composition, pressure and fields (particularly the transfer and induction fields). For Ne/CH_4 (5%) at 0.7 bar and 180 K with transfer and induction fields of 1 kV/cm, the time difference between the PMT S_1 signal and the corresponding signal on the GPM was found to be ~220 ns, as shown in Figure 5.26, corresponding to the time spread of collection of emitted photoelectrons plus the drift time for the electrons to transverse the three transfer gaps with 1 kV/cm electric field and the drift time through the three THGEMs holes with high (<10 kV/cm) electric field; for Ne/CH_4 (20%) under the same conditions, the GPM signal appeared only ~135 ns after the PMT signal. This is expected, based on the known increase of the electron drift velocity with the percentage of methane in Ne/CH_4 mixtures [**75**].

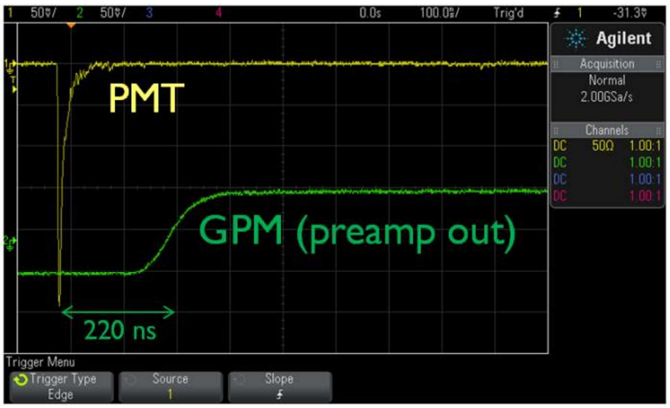

Figure 5.26 – The GPM S_1 signal (at the charge sensitive preamplifier output) along with the corresponding signal on the PMT, for Ne/CH_4 (5%) at 0.7 bar and 180 K. The vertical scale is 50 mV/div for both of the pulses while the horizontal scale is 100 ns/div.

While the GPM response is delayed compared to that of a PMT, its time resolution was shown to be on the nanosecond scale. The GPM time resolution was measured with reference to the PMT signal using the PMT and GPM output signals as the 'start' and 'stop' signals, respectively, for a time-to-amplitude converter (TAC), which provides an output signal whose amplitude is proportional to the time difference between both. The setup used is shown schematically in Figure 5.27: the PMT output signal was connected to an Ortec 934 Quad-constant fraction discriminator (CFD), followed by an adjustable delay box and connected to the start input of an Elscint time–to–amplitude converter model N-1, initiating the internal timer. On the other hand, the GPM signal was amplified and shaped by a Canberra 2006 preamplifier and an Ortec 474 timing filter amplifier (TFA). The shaped GPM signal was then provided to another channel of the Ortec 934 Quad-CFD and then to the 'stop' input of the TAC. The TAC output was used as the input signal for the multichannel analyzer (Amptek 8000A pocket MCA).

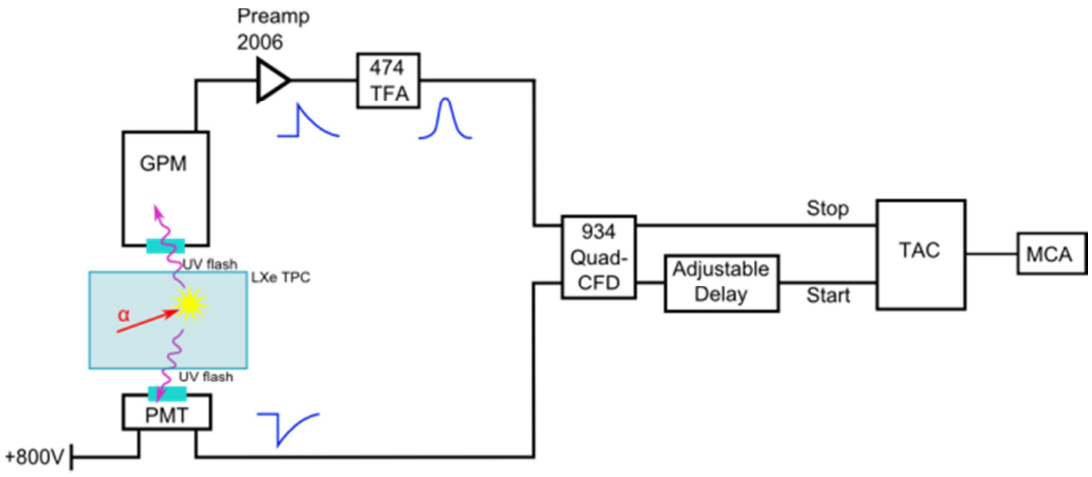

Figure 5.27 – Setup used for measuring the time jitter between the GPM and PMT signal.

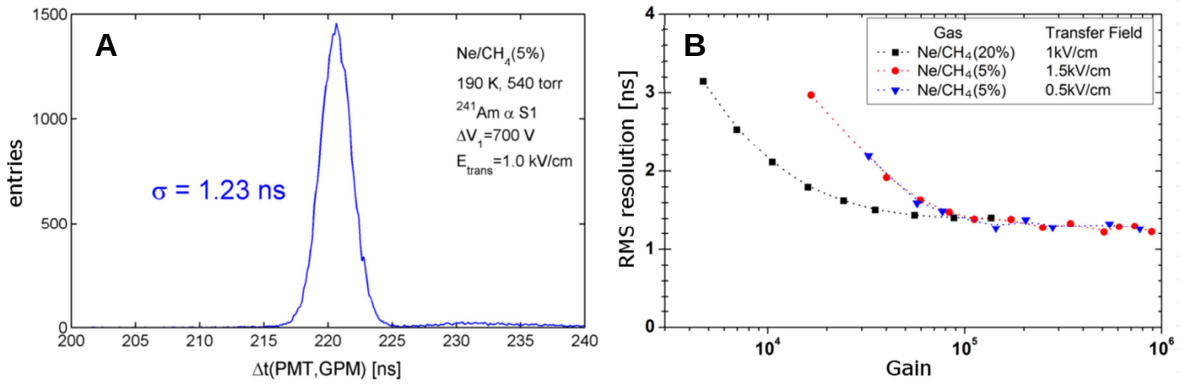

Figure 5.28 – (A) Distribution of the time differences between the GPM and PMT alpha particle S1 signals at a gain of ~3×10^5 and, (B) Dependence of the time jitter (standard deviation of the GPM-PMT time-difference distribution) on the overall detector gain for Ne/CH_4(5%) and Ne/CH_4(20%) at 0.7 bar and ~190 K.

Figure 5.28A shows the time difference distribution in Ne/CH_4 (5%), measured at a gain of 3×10^5. Figure 5.28B shows the RMS time resolution (standard deviation of

the time difference distribution) as a function of the GPM gain for Ne/CH_4 (5%) and Ne/CH_4 (20%) at 0.7 bar and ~190 K. The voltage on the THGEM1 was 700 V for Ne/CH_4 (5%) with the transfer and induction fields set at 0.5 kV/cm, and 1000 V for Ne/CH_4 (20%) with the transfer and induction fields set 1 kV/cm and 1.5 kV/cm (the gain was varied by changing the voltages on THGEMs 2 and 3). In all cases, the time jitter decreased with increasing detector gain (i.e., with increasing $\Delta V_{2,3}$), approaching a plateau of ~1.2 – 1.3 ns RMS. While a full explanation for this behavior requires a detailed simulation study, it may result from improved focusing of the electrons into the holes of THGEMs 2 and 3 with increased voltages. For Ne/CH_4 (20%) the faster stabilization of the time jitter on the 1.3 ns plateau (as a function of the overall gain) may be attributed to the fact that for a given gain the THGEM voltages are significantly higher than for the Ne/CH_4 (5%) gas mixture, leading to a faster signal formation. It should be emphasized that these measurements were all performed with alpha particle induced S_1 signals comprising ~170-200 photoelectrons per event; the ultimate time resolution should obviously be defined for single-photoelectron pulses. These are expected to be governed by signal-to-noise issues, by the hole-geometry of the THGEM electrodes, and by the electric field at the photocathode surface.

5.6 Discussion

The maximum gain obtained at 0.7 bar and 180 K was $\sim 8\times10^5$ for Ne/CH_4 (5%) and $\sim 3\times10^5$ for Ne/CH_4 (20%). For both gas mixtures, “asymmetric” THGEM polarization (with higher voltage across THGEM1) proved to be more stable. Starting at gains of $\sim 10^3$, alpha-particle induced S1 and S2 signal pairs were observed on the GPM anode. With Ne/CH_4 (5%) at a gain of 1×10^5 and alpha-particle S_2 signals at 40 Hz, the

discharge probability was found to be of the order of 10^{-6}. In terms of S1 and S2 energy resolution, for S1 a RMS resolution of $\sigma/E=10.9\%$ was derived (by fitting a Gaussian to the entire S1 peak) while for S2 a Gaussian fit to the left side of the peak gives $\sigma/E=8.7\%$. This is comparable to that obtained in XENON100 with PMTs (there $\sigma/E=10.0\pm1.5\%$), for a similar number of ionization electrons (~8000) entering the gas phase.

While the GPM response is delayed compared to that of a PMT, its time resolution was shown to be on the nanosecond scale. In all studied gas mixtures, the time jitter decreased with increasing detector gain (i.e., with increasing $\Delta V_{2,3}$), approaching a plateau of ~1.2 – 1.3 ns RMS for ~200 photoelectron signals.

Chapter 6 – Position readout

6.1 Introduction

Reconstructing the interaction position as well as estimating the number of secondary scintillation photons emitted from the gas phase of double phase detectors is fundamental for the determination of valid primary scintillation events and for discrimination between electronic and nuclear recoils in the liquid phase. Current and future double-phase experiments use a time projection chamber (TPC) to detect rare-events. These experiments rely on phototubes ranging from 1” to 3” in diameter arranged in arrays on the top and bottom of the TPC. The top array is primarily used to reconstruct the (x, y) coordinates of the interaction while its z-position is determined from the time difference between the primary and secondary scintillation signals (S1 and S2, respectively). In existing double-phase experiments the (x,y) positions are determined from the photon hit pattern on the top PMTs and the resolution is smaller than 3 mm (1σ) in XENON100 [**73**], between 4 to 6 mm in LUX [**76**] and for the proposed next generation DARWIN detector it is expected to be 8 mm [**77**].

In this section I will describe the methods used for simulating a future large volume double-phase detector, focusing particularly on the physics of secondary scintillation photon propagation from the gas phase to a gas photo multiplier detector (GPM). A center of gravity method is used to determine the most likely position of the event and the deviation from the actual position is computed for several pixel sizes. The

results were taken into consideration in the design of a segmented position sensitive readout to be used in the GPM for WILiX.

6.2 Position resolution simulations

We optimized the pixel's size by simulating scintillation photons in the 2.5 mm gas phase of a DARWIN-type experiment [**78**] (a 2 meter in diameter and 2 meter high cryostat for a double-phase xenon TPC) and calculating the deviation between the actual scintillation point and the calculated center-of-gravity point, for different pixels sizes (binning).

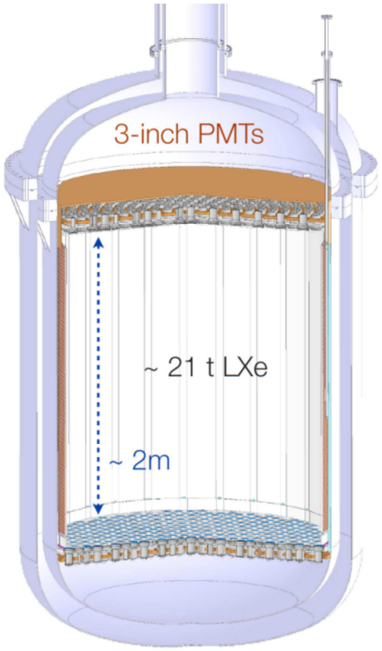

Figure 6.1 – Computer generated model of the DARWIN consortium multi-ton liquid xenon detector.

The physical model implemented in GEANT4 is based on the latest conceptual design of the next-generation large-volume double-phase detector as proposed by the DARWIN consortium [**79**], and represented in Figure 6.1.

The model is composed of a cylindrical geometry representing the internal volume with a height of 2040 mm and diameter of 2000 mm, the material of the inner walls of the cylinder are defined as PTFE and a top window of quartz. For the calculations the liquid xenon level was set at 2 m high. Above the liquid surface the quartz window was modeled as 10 mm thickness, separated by a xenon gas gap of 40 mm thickness. The window was modeled as "one piece" for simplicity, although in reality some supports will inevitably be used for mechanical rigidity. In Figure 6.2 is represented a typical simulated scintillation event, highlighting the liquid and gaseous xenon phases, the quartz window and the detection space filled with Ne/CH_4.

The origin of the secondary scintillation photons was defined to be a cylindrical volume whose height corresponds to the region of high electric field between the liquid surface and a mesh. The radius of the cylindrical volume is a random number whose maximum value was set at 5.6 mm. This maximum value is given by the following expression:

$$r(Z) = \sqrt{\frac{\sigma_T * \mathrm{Z}}{\pi * v_d}}$$

Where σ_T is the electron transverse diffusion coefficient at a given drift electric field, in cm^2/s, Z is the interaction depth within the TPC, and v_d is the electron drift velocity in liquid xenon for a given drift field and considering the worst hypothetical case scenario of an interaction occurring at the bottom of the 2meter deep TPC (Z=2000 cm). The initial electron cloud would drift upward with a velocity $v_d = 2\times10^5$ cm/s

(considering a drift field of 0.6 kV/cm), taking approximately 0.01s to transverse the whole length of the TPC. Simultaneously to this movement the electron cloud diffuses both longitudinally and transversely – the transverse diffusion coefficient is taken to be σ_T~100 cm^2/s, see Figure 2.11. The position of the cylinder was then randomly set.

The localization of the interacting particle in the LXe volume is derived from the calculated center of the gravity (CG) of all the secondary scintillation photons detected by the segmented readout electrode of the GPM. The average number of scintillation photons, created within the xenon gas gap, was predicted to be 208 per extracted ionization electron from the liquid [**80**], given empirically by:

$$n_{ph} = 70 * \left(E_e/p - 1\right) * x * p$$

where E_e is the applied extraction field of 12 $kV*cm^{-1}$ across a Xe gas gap, *x*, of 0.3 cm and a gas phase pressure, *p*, of 2.1atm.

The hit position of each photon on the readout was then recorded and the corresponding coordinates used for the calculation of the center of gravity, according to the following set of equations implemented in a MatLab routine [**81**]:

$$\begin{cases} COG_X = \sum X_i n_i / \sum n_i \\ COG_Y = \sum Y_i n_i / \sum n_i \end{cases}$$

Where X_i and Y_i are the coordinates of the center of each pixel in the *XX* and *YY* axis respectively, and n_i is the number of hits within the considered pixel. Figure 6.3 shows typical hit patterns obtained from GEANT4 and processed by MatLab.

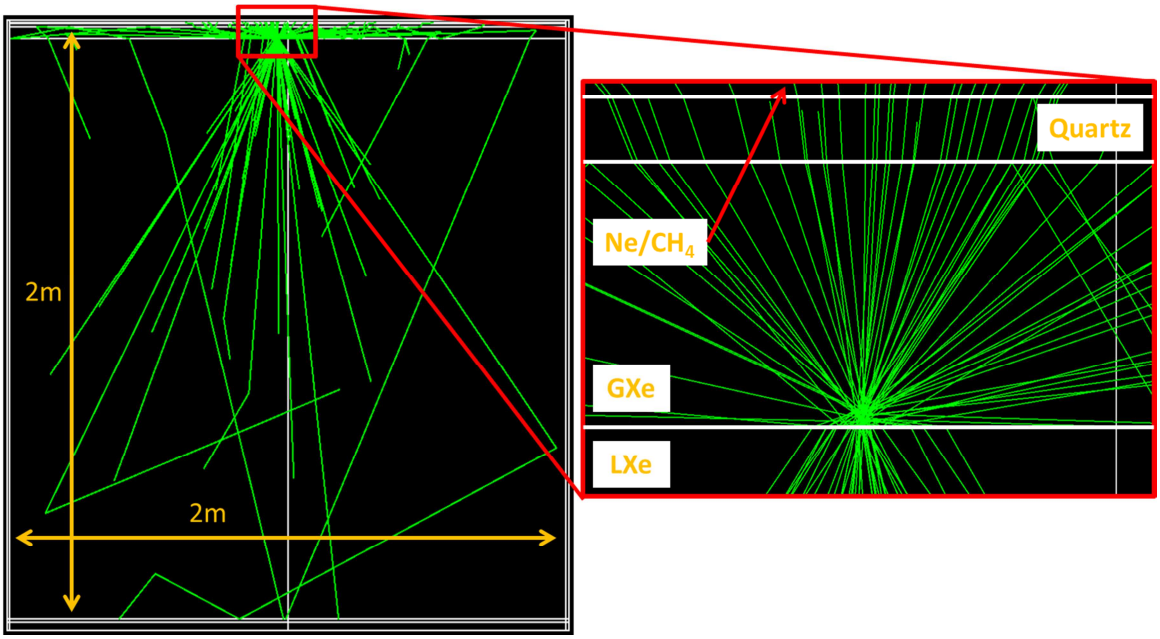

Figure 6.2 – Result of a GEANT4 simulation run of the implemented detector. The green lines are the calculated photon paths taking into account reflections, refractions and absorptions, highlighting the liquid and gaseous xenon gap and the quartz window.

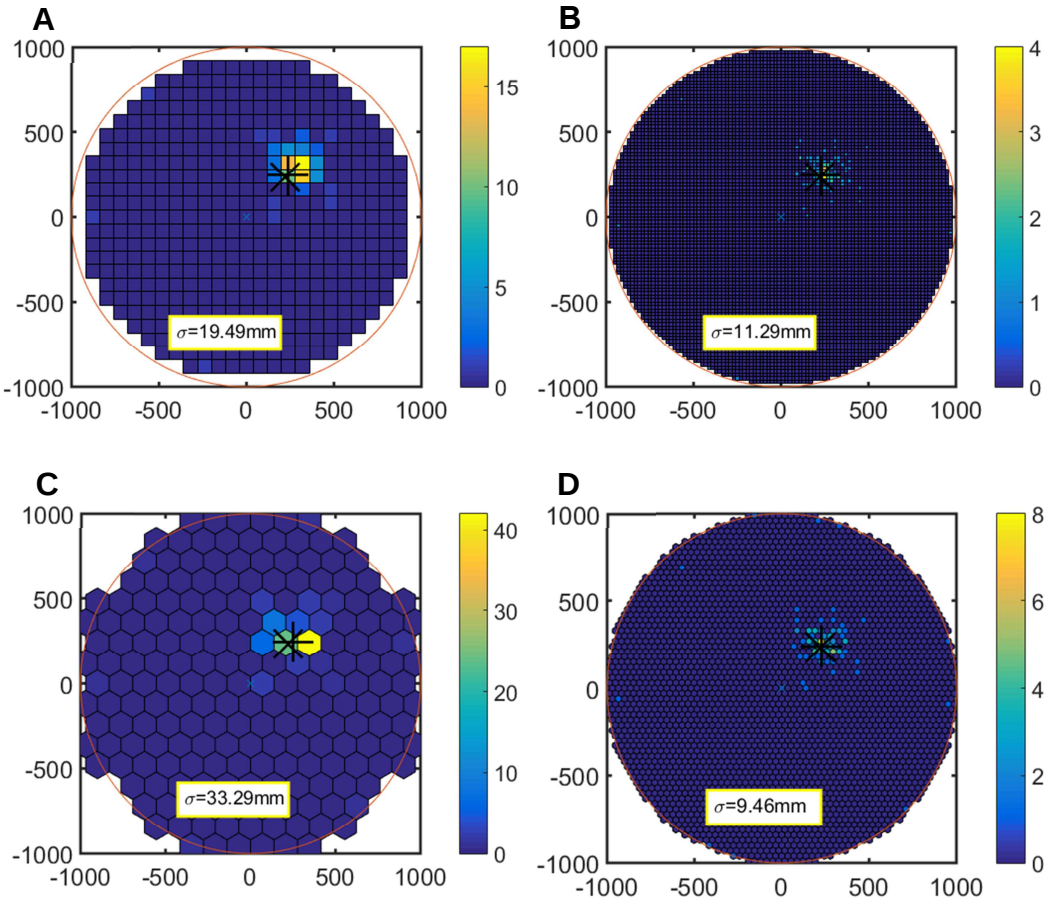

Figure 6.3 – Typical hit patterns on the detector volume resulting from the simulations for two different pixel sizes and shapes for a number of photons equivalent to 10electrons emerging from the liquid surface (~1800photons), the same event is represented for: A and B, square pixels , and C and D, hexagonal pixels of 80 mm and 20 mm size, respectively. Inset is the deviation between the real COG and calculated COG.

Figure 6.4 shows COG reconstruction deviation, for Xenon100 [**73**] and Xenon1T experiments, for comparison. There is no decrease in the reconstruction deviation while

using pixels sizes up to 30 mm, due to averaging effect of the large number of photoelectrons.

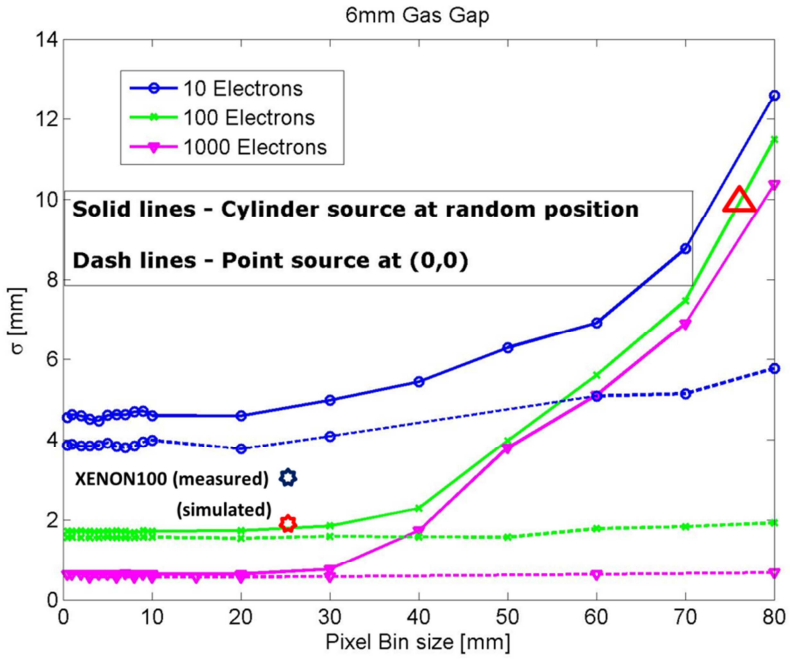

Figure 6.4 – Deviation between actual scintillation point and calculated center-of-gravity, for different pixel sizes, as calculated for DARWIN, XENON100 (simulation and measurement) and XENON1T experiments.

6.3 Segmented anode design

For the segmented readout design it was decided to use hexagonal versus conventional square pads since it provides the most efficient and compact division of the round surface available with equal sided polygons [**82**]. The next design consideration was, for the first prototype, to use less than the total available channels on the analog readout chip selected for use in the WiLIX–GPM. The selected analog readout chips have the

benefit of the already acquired know-how and the potential low-noise (1-2 fC) [**83**] and small size.

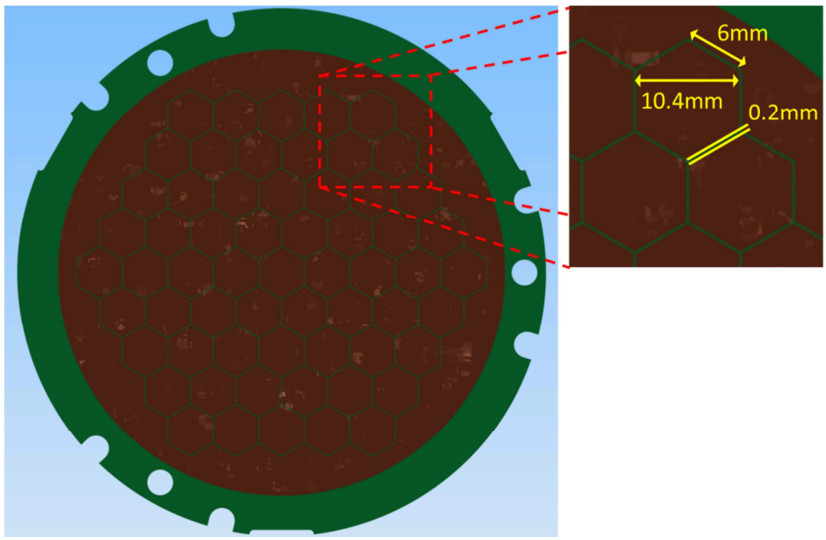

Figure 6.5 – Autodesk Inventor image of the designed segmented readout with main dimensions highlighted.

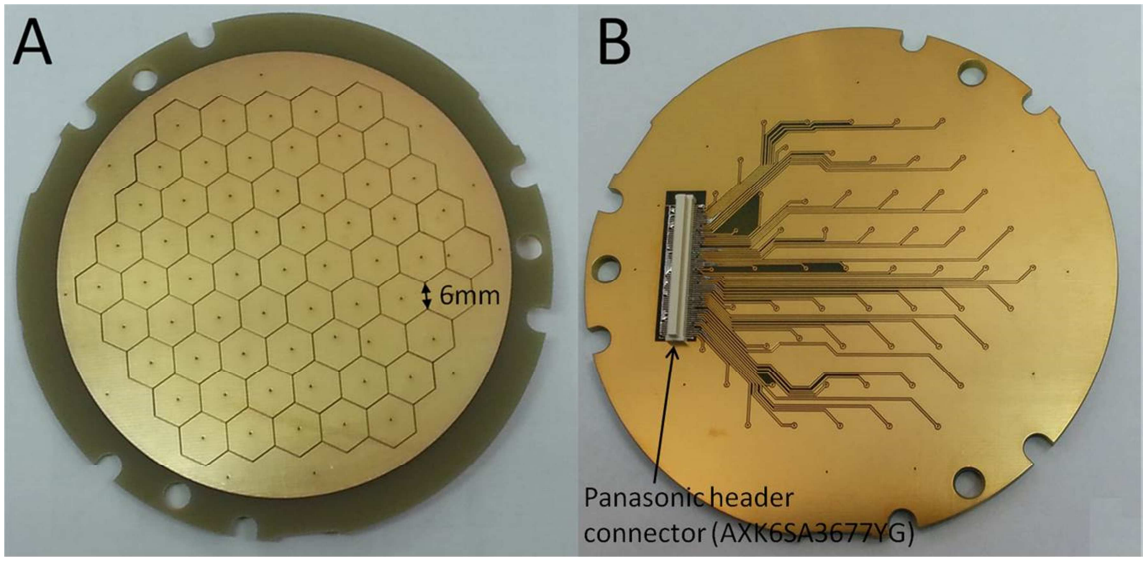

Figure 6.6 – Photograph of a segmented 61 pixel hexagonal-pad readout. A) Front and B) back. Pad side is 6 mm.

The segmented readout (Figure 6.5) was designed with 61 6 mm sided hexagons that cover almost completely the useful area of the THGEM. Each hexagon is 10.4 mm across with an area of 93.5 mm^2. The total active area is 5705.4 mm^2. The spacing between each pad was set at 0.2 mm. The readouts were produced and tested by Shenzen Suntak Multilayer PCB Co. in 3.2 mm thick FR-4 with 70 μm Cu plating on each side, followed by 4.2 μm Ni followed by 0.07 μm Au.

The electrical contact between the segmented readout and the analog readout electronics is done via standard RD51 130-pin Panasonic socket (male on readout, female on chip). In Figure 6.6 is represented a photograph of a finished segmented readout.

6.4 First imaging results

To test the position readout sensitivity at room temperature and to test the complete electronics suite coupled to the hexagonal pads readout, a series of experiments were devised that consisted in visualizing the charge density of alpha particles tracks emitted from a ^{241}Am source into Ne/CH_4(95:5) and the imaging of UV light.

For the alpha-track visualization and UV light imaging a test detector was assembled that consisted in a Double-THGEM configuration, the hexagonal pads readout and the electronics suite, a simple gas system consisting in a pre-mixed Ne/CH_4(95:5) cylinder, a gas-flow regulator and a bubbler. For the UV light imaging experiments a quartz 2¾" CF window was installed with a transmission of 85.5% for λ=175 nm, but only 4.3% at λ=160.8 nm (main emission from the H_2 lamp), a CsI

photocathode was deposited on the first-THGEM and a flashed hydrogen lamp was used to extract photoelectrons.

The experimental setup is shown in Figure 6.7. The THGEMs were made of an FR4 plate with an active diameter of 100 mm and with a thickness t = 0.4 mm, Cu-clad on both sides. The drilled hole pattern was hexagonal, with a pitch a = 0.8 mm (between the hole centres) and hole diameter d = 0.4 mm; the width of the etched hole rims (h) was 10 μm. The Cu layer thickness (after etching) was 64 μm. The THGEM electrodes were produced by ELTOS SpA, Italy. The final processing stages, including gold-plating, cleaning and baking were done in the CERN MPGD workshop. The transfer gaps between the stages, as well as the induction gap between the last THGEM and the segmented readout electrode were 1.5 mm wide. Each of the THGEM faces, as well as the mesh mounted 13 mm above THGEM1, had a separate high voltage bias, provided through low – pass filters.

The segmented readout electrode contains 61 hexagonal pads arranged in a hexagonal pattern (see Figure 6.6A). Each of the 6 mm pads is connected to a Panasonic header connector (type: AXK6SA3677YG) (see Figure 6.6B), which is suitable for the SRS (Scalable Readout System [**84**]) frontend hybrid, the APV25 chip [**85**]. The APV25 chip can be connected directly on the readout electrode, however, in our measurements the signals from each pad were transferred to the APV25 chip through a ribbon flat cable (3754/80 80 conduct 0.025" pitch) 30 cm long and two PCB adaptors: 1. Panasonic to flat cable adaptor, using a PCB with Panasonic socket AXK5SA3277YG and SBH41-NBPB-D17-ST-BK connectors, and 2. flat cable to Panasonic adaptor, using a PCB with Panasonic header (type: AXK6SA3677YG) and SBH41-NBPB-D17-ST-BK connectors. The flat cable was wrapped by copper tape and aluminum foil. The APV25's ground was well connected to the electrode ground.

The APV25 chip was connected to the SRS [**84**] using a 1 meter long homemade vacuum rated micro-HDMI to HDMI cable and feedthrough. Triggers for the SRS were extracted from the top of the THGEM closest to the readout electrode through a coaxial cable into a Canberra 2006 charge sensitive preamplifier connected on the outer side of the GPM chamber's top flange.

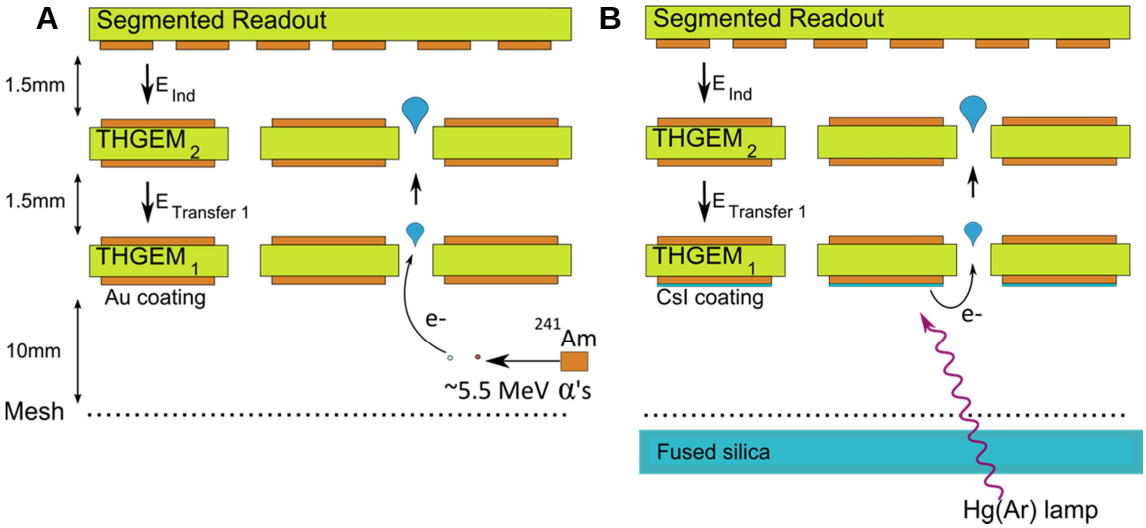

Figure 6.7 – Schematic of the setups used for the position sensitivity tests: A) Setup for the 241Am source, and B) Setup for the UV light imaging.

6.4.1 Alpha-particle tracks

For the alpha particle track visualization the ^{241}Am source was placed halfway in the drift gap, between the drift mesh and the first THGEM, with the source face perpendicular to the THGEM face. The alpha particles were emitted primarily in the direction perpendicular to the applied drift field. The alpha particles were stopped within a few centimeters in the Ne/CH_4(95:5) and the resulting ionization electron cloud

was drifted towards the first THGEM' holes, were they underwent electron impact ionization due the high applied electric field. The resulting electron avalanche was then drifted towards the holes of the second THGEM where it underwent further electron impact ionization before being drifted to the segmented anodes' pads.

Typical single alpha track events, as measured in the hexagonal pads electrode, are shown in Figure 6.8A and Figure 6.8B. In this figure the color bar represents the charge in each pad in femtocoulombs.

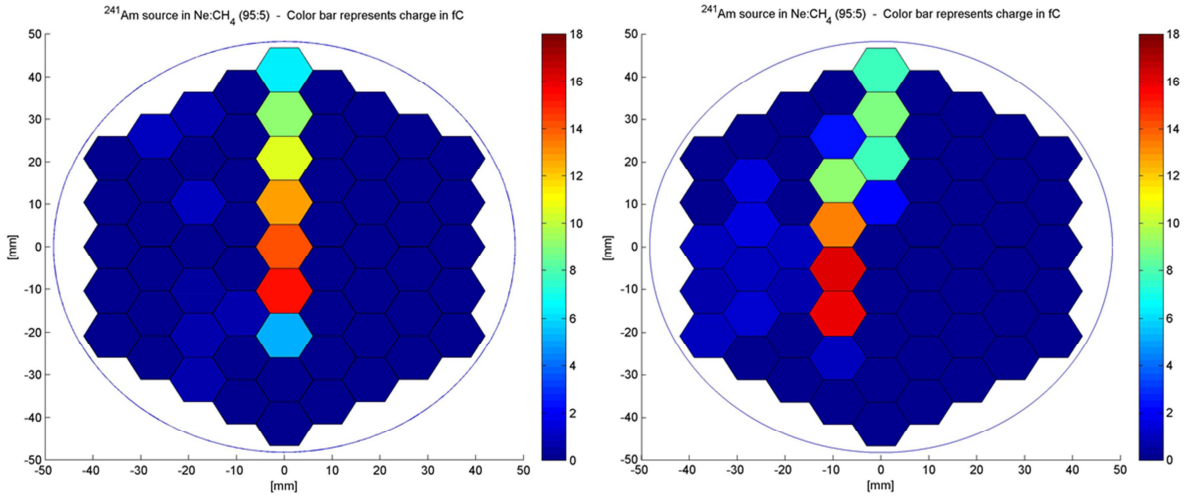

Figure 6.8 – Typical single alpha track events, as measured in the hexagonal pads electrode. The color bar on the right represents the charge in each pad in fC.

6.4.2 Flashed UV lamp test

For these tests the self-discharging flashed H_2 lamp (UV emissions peaking at 157.8 and 160.8 nm) previously described in 5.4.2 was used, shining on the GPM through a pinhole (ϕ=3 mm) and the 2¾" CF window. For these measurements the SRS

acquisition was triggered directly by the UV lamp discharge. A typical single UV-scintillation event, as measured in the hexagonal pads electrode, is shown in Figure 6.9.

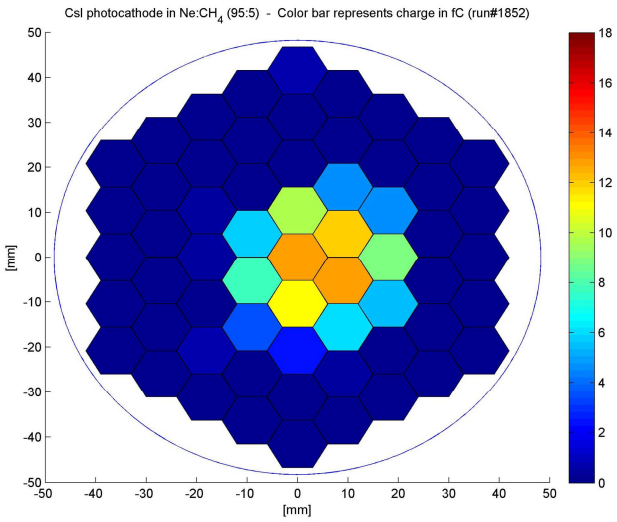

Figure 6.9 – Typical single UV lamp discharge event, as measured in the hexagonal pads electrode. The color bar on the right represents the charge in each pad in fC.

For the measurements of various lamp positions the voltages applied on the detector were set at V_{mesh}=-1100 V, V_{T1}=-800 V, V_{B1}= 475 V, V_{T2}=-400V and V_{B2}=-75V. The lamp voltage was set at +2273V. For each measurement of different lamp X-Y position, the center of gravity (COG) was calculated, event by event, according to the following equation, with a threshold of 1.6fC on the charge in each pad:

$$\overrightarrow{COG_i} = \frac{\sum_{j=1}^{j=61} \vec{P_j} \cdot Q_{i,j}}{\sum_{j=1}^{j=61} Q_{i,j}}$$

Then, a 2D histogram of the COGs is plotted. In the equation, $Q_{i,j}$ is the charge collected in event i by pad j and $\vec{P_j}$ is a $[x,y]$ position vector of the center of pad j. Table 3 lists the calculated COG for seven different measurements of lamp positions. In these

measurements, the number of photoelectrons in each event was ~1.3×10^5. As can be seen, the calculated COGs are in very good agreement (within few tenths of millimeter) with the actual lamp positions. In two cases (line 6 and 7) there is bias of 2–3 mm in the calculated *Y* position, probably due to edge effects of the small quartz window.

Measurement number	Lamp position		Calculated COG	
	X [mm]	Y [mm]	X [mm]	Y [mm]
1	0.3	-8.4	0.1	-7.9
2	5.0	-1.9	4.8	-1.6
3	7.9	2.2	7.8	2.3
4	11.9	-0.7	12.0	-1.3
5	12.1	-5.7	12.3	-6.0
6	5.7	-14.7	5.1	-11.5
7	3.2	-12.9	2.9	-10.9

Table 3 – Calculated COG for seven different measurements of lamp positions.

Chapter 7 – Study of submillimetric induction gaps

7.1 Introduction

Following the promising studies performed in Coimbra with the Gas Electron Multiplier coupled to a Micro Induction Gap Amplification Stage, or the GEM – MIGAS [**86**], [**87**], [**88**], an analogous configuration of a THGEM coupled to a submillimetric induction gap was investigated to eventually obtain a GPM configuration capable to reach higher gains with lower biasing voltages.

7.2 Electric field simulations

Electric-field simulations with Ansys release 12 package [**89**] were carried out to assess and optimize the field strength and distribution in the THGEM/parallel-gap configuration, under various geometrical and bias conditions. They permitted to define the conditions and the region of electron multiplication.

The unit cell shown in Figure 7.1 corresponds to a 4-fold rotation of the basic 1/4 cell along the Z-axis used in the simulations and consisted of a THGEM with the following parameters: 0.4 mm thick G–10 with 0.02 mm thick copper clad on both sides, cylindrical holes of 0.3 mm diameter arranged in a hexagonal pattern with 1 mm

pitch and an etched rim around holes of 0.1 mm; the multiplication parallel gap was of either 400 μm or 800 μm deep. The drift/conversion region was set at 11.5 mm.

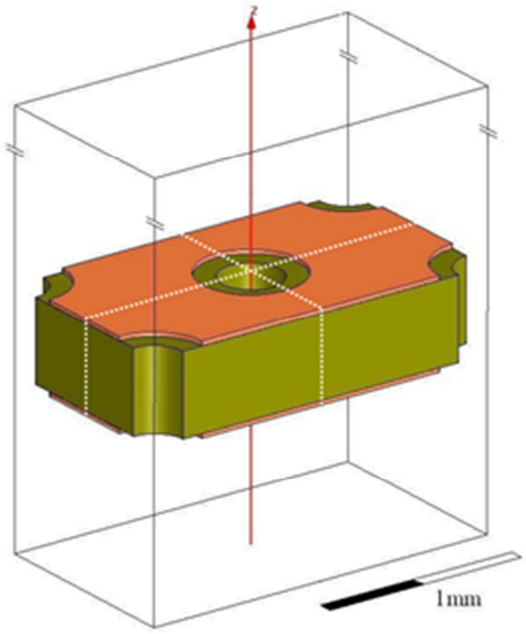

Figure 7.1 – Representation of the three dimensional THGEM cell, highlighting the boundaries (white dotted lines) of the repeated unit cell used in the simulations.

The electric-field strength was calculated along the axis of one of the THGEMs holes, i.e. along the Z–axis in Figure 7.1, at different bias settings on the THGEM and for different parallel-gap depths. In all of the following representations the abscissa corresponds to the distance (in mm) from the anode in the multiplication gap, with the origin corresponding to the anode. The drift field was set at constant value of 0.5 kV/cm. Figure 7.2 provides the simulation results for a 400 μm gap. In these simulations and for each case the bias voltage on the THGEM was varied in the range 50 – 350 V, while across the gap the induction voltage was set at 40, 160 and 280 V, corresponding roughly to parallel-gap fields, E_{Gap}, of 1, 4 and 7 kV/cm, respectively. Figure 7.3 depicts simulation results for an 800 μm induction gap, for induction

voltages set in the range 0 – 280 V and THGEM bias values of 150V, 250 V and 350 V. The gap voltages were selected so as to roughly correspond to E_{Gap} in the range of 0 – 3.5 kV/cm in 0.5 kV/cm steps.

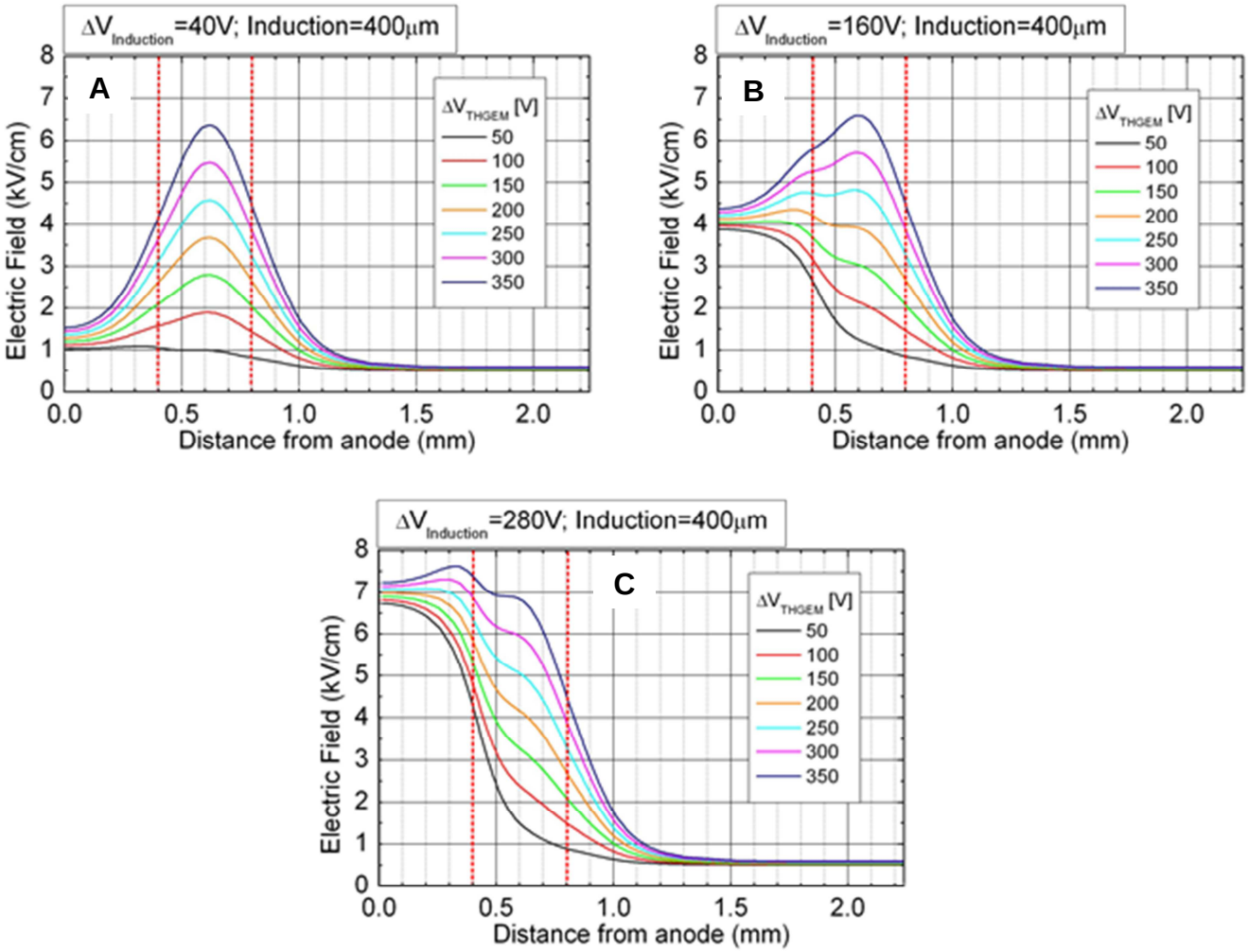

Figure 7.2 – Electric field profile along the axis of a THGEM hole coupled to a multiplication gap of 400 μm, for THGEM voltages in the range of 50 to 350V; gap voltages: 40V (A), 160V (B) and 280V (C).

The simulation results show an evidence of the interdependence of the hole and the induction electric fields in a region between halfway within the THGEM holes and part of the induction region, just outside the holes, which can extend as far as to 300 μm away. Outside this region the influence of the fields on each other becomes negligible.

For low induction fields, e.g. typical fields of ~1 kV/cm, the electric field inside the holes dominates, reaching values of ~6.4 kV/cm at the center of the hole, for typical THGEM voltages of 350 V, presenting a fast decrease when approaching the exit and reducing to values of about 3 and 2 kV/cm at distances of 100 and 200 μm away from the hole exit. We note that in the Ne/5%CF_4 gas mixture used in this work, the onset for gap multiplication was evaluated to be ~2 kV/cm [**90**]. Therefore, if one wants to exploit the full development of the charge avalanche of the THGEM, the induction gap should be thicker than the above values. Nevertheless, even for a distance of 800 μm away from the hole exit there is a slight increase in the induction electric field as the THGEM voltage increases.

As the induction voltage increases, the electric field around the hole exit increases and the charge avalanche extends to outside the holes. Increasing further the voltage in the induction region, the charge avalanche eventually extends to the whole induction region. For high induction voltages, the induction electric field dominates, increasing significantly the field inside the hole, in the region close to the hole exit. Nevertheless, the effect of the induction field becomes smaller towards hole center, e.g. at the hole center the electric field increases only from 6.4 to 6.8 kV/cm and from 4.5 to 5.0 kV/cm as the induction field near the anode increases from 1 to 7 kV/cm, for a THGEM voltage of 350 V and 250 V, respectively.

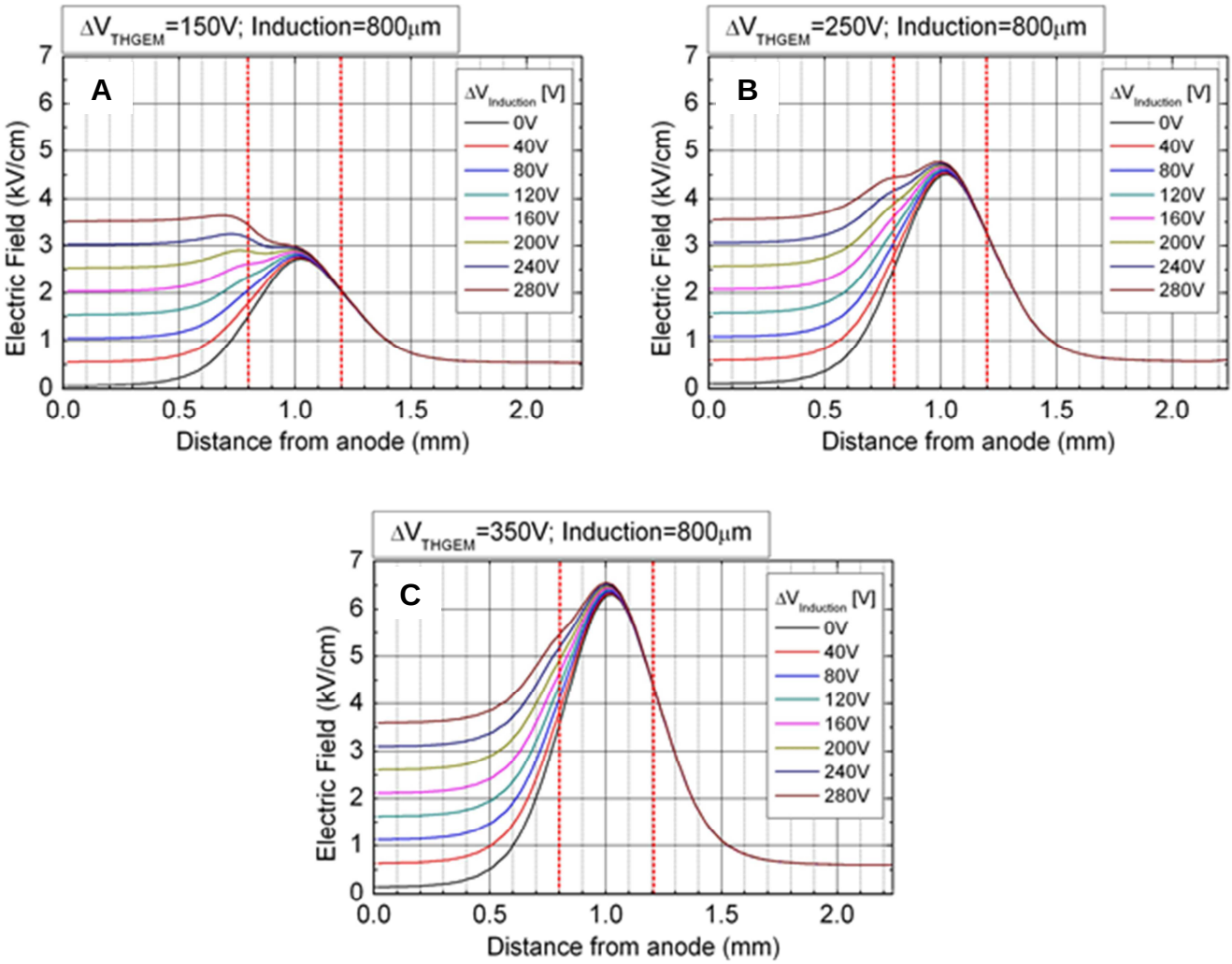

Figure 7.3 – Electric field profile along the axis of a THGEM hole coupled to a multiplication gap of 800 μm, for gap voltages in the range 0 to 320 V and for THGEM voltages of 150 V (A), 250 V (B) and 350 V (C).

For the experimental work, we used a single THGEM produced from G-10 with 0.4 mm thickness and with a 0.02 mm copper clad on both sides. It had a hexagonal pattern of 0.3 mm diameter holes, with a pitch of 1 mm over an active area of 20 mm by 20 mm; the holes had 0.1 mm wide etched rims.

The THGEM was assembled inside a cylindrical stainless steel vessel (~150 mm in diameter) where in one of the bases a 75 μm thick Kapton window 10 mm in diameter was installed. The Kapton was glued to the chamber with TRA-BOND 2116 low vapour-pressure epoxy. The detector, depicted in Figure 7.4, had a stainless-steel drift mesh, of 50 mm thick wires and with 500 mm pitch, the THGEM and a copper anode plane; it was assembled on Teflon mountings within the stainless steel chamber. The drift/conversion region was 11.5 mm wide, set by Macor spacers; the induction (multiplication) gap was varied from 400 μm up to 800 μm, using spacers of adequate thickness.

The chamber was vacuum pumped down to 10^{-5} mbar by a turbo-molecular pump and then filled with 1.1 bar of each gas mixture. The gases used were research grade Ne N4.0 (Ne 99.99%), Ar 5.0 (99.999%), CH_4 4.5 (CH_4 99.995%) and CF_4 R14 (purity of 99.8%); Ne was filled through a cold finger immersed in liquid nitrogen. After filling, the chamber was decoupled from the gas-filling system and gas purity was maintained by circulating it, by convection, through SAES St707 non-evaporable getters, heated to ~150ºC. Measurements were made after at least 24 hours of gas purification.

The detector was irradiated through the Kapton window with 5.9 keV X-rays from a ^{55}Fe source, collimated to 1.5 mm diameter. The resulting primary electron cloud deposited in the 11.5 mm drift region was focused into the THGEM holes where the electrons were multiplied. The avalanche electron cloud was extracted into the following gap where further multiplication occurred under sufficiently high electric field. The resulting electron charge signal was read-out on a copper anode, with a Canberra 2004 charge pre-amplifier with a sensitivity of 0.2V/pC. The charge signals were also visualized on a digital oscilloscope Tektronix TDS 2022B (200 MHz, 2 GS/s). The average counting rate with the X-ray source was of ~450 Hz. The charge signals

were further processed by a Canberra 2025 shaper; pulse-height spectra were recorded with a Maestro Multi-Channel Analyzer. The electronic chain was calibrated for charge gain determination using the 2.2 pC/V test input of the preamplifier and a BNC model PB-3 precision pulse generator.

The drift mesh was biased using an Ortec 659 high-voltage power supply; the THGEM electrodes were biased with a CAEN N471A high-voltage power supply. Voltages were supplied to the respective electrodes through low-pass RC filters with a cutoff frequency of ~16 Hz.

The pulse-height distributions obtained for the 5.9 keV X-rays were fitted to a Gaussian superimposed on a linear background; the peak centroids and the respective FWHM values were registered for each experimental condition. The detector gain was derived from the centroids, using the electronics calibration.

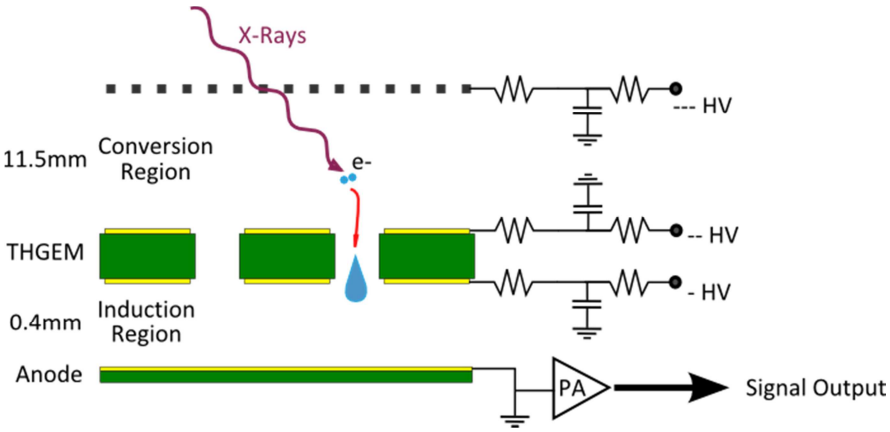

Figure 7.4 – Setup used in pulse-mode measurements. Charges deposited in the drift gap are multiplied in the THGEM; avalanche electrons are further multiplied in the following thin parallel gap.

7.3 Ne mixtures with tetrafluoromethane

7.3.1 Charge gain characteristics

Figure 7.5A depicts the charge gain measured on the anode as a function of the voltage applied to the THGEM (ΔV_{THGEM}), for different values of electric field in the multiplication gap (E_{Gap}) (between 1 and 5.7 kV/cm), of 400 μm depth following the THGEM. The limitation on the applied induction field and ΔV_{THGEM} was determined by the onset of discharges at a rate of about 0.5 discharges per minute. A gain increase from 7.8×10^3 to 2.2×10^4 was observed for E_{Gap} increase in the multiplying gap from 1 to 5.7 kV/cm. The gain curves show a typical exponential rise; the increase in E_{Gap} showed a shift of the gain-curves to lower THGEM bias values, as previously observed in GEM-MIGAS [**91**].

Figure 7.5B presents the gain curves for a multiplication gap of 500 μm. A somewhat larger gain increase with increase of E_{Gap} is observed, compared to the smaller gap: from ~2×10^4 at 1 kV/cm to 10^5 at 5.6 kV/cm. A thicker induction region allows further development of the electron avalanche. Figure 7.5C depicts the gain with an 800 μm thick multiplication gap. A maximum gain of ~10^5 before the onset of micro-discharges was obtained with an E_{Gap} of 3.8 kV/cm.

Previous works [**92**] provided maximum gains in Single-THGEM of ~5×10^3 and in a Double-THGEM of ~7×10^4, in the same gas mixture of Ne/CF_4(95:5). Thus the maximum gains reached during the present studies using the THGEM and submillimetric induction gap multiplication proved to reach about 10 fold higher gains than those with the Single-THGEM detector, and similar to that with a double-THGEM.

In Figure 7.6 the charge gain is depicted as a function of the induction field for different values of the THGEM voltage, for a THGEM followed by an 800 μm thick

induction gap. An upper induction-field limit around 3.8 kV/cm was reached before the onset of discharges. The same trend was observed for the 400 and 500 μm thick induction gaps, with field limits around 5.5 kV/cm. The limit on the electric field could be due to avalanche-photon feedback within the induction gap. This process involves UV photons (emitted, or not quenched by CF_4) from the gap-avalanche, impinging on the THGEM bottom electrode and releasing photoelectrons. Thinner induction gaps may sustain higher induction fields, possibly due to smaller avalanche development. Therefore, CH_4 should be a more adequate quencher in this detector configuration – this hypothesis will be covered in the next section.

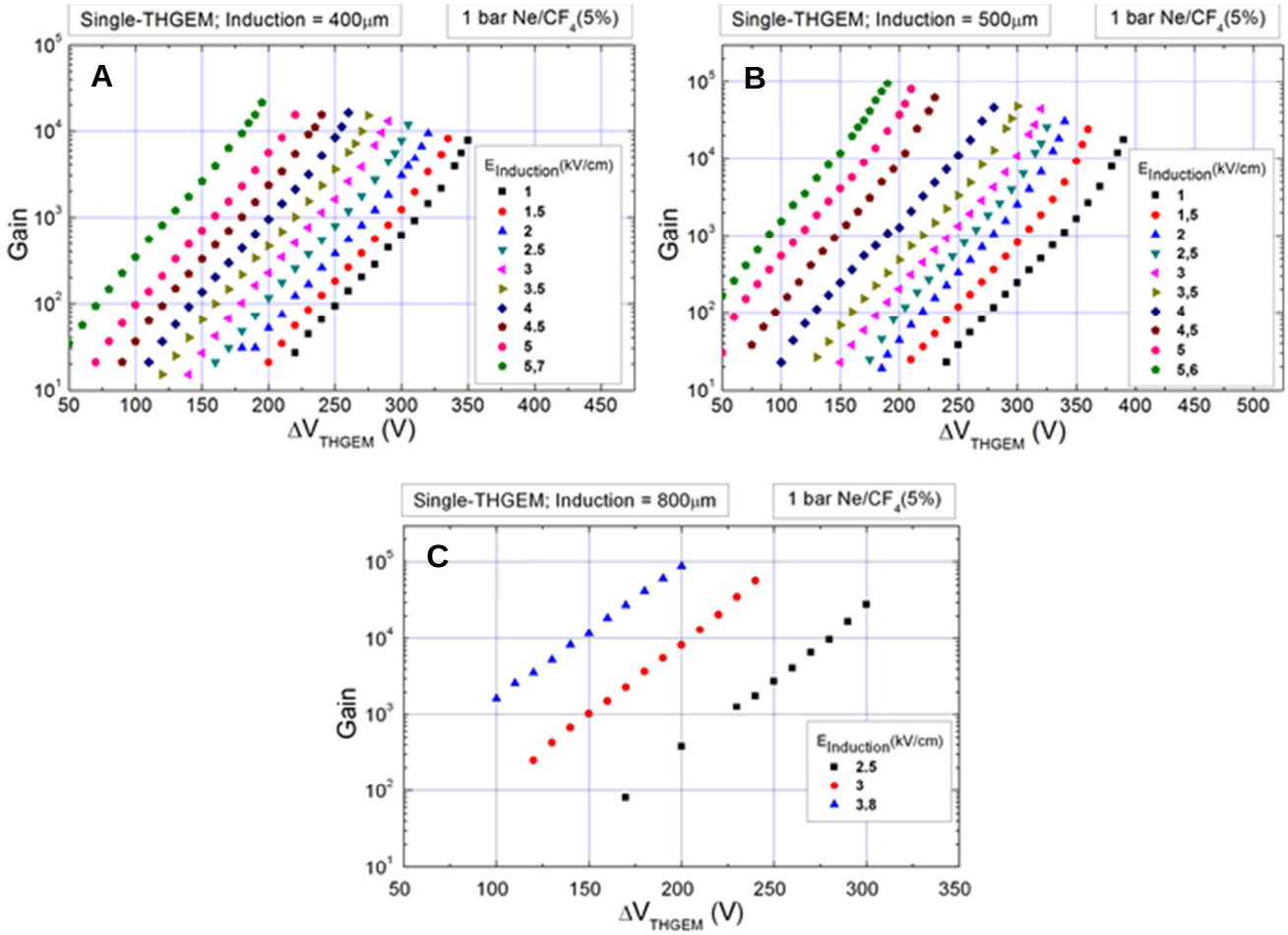

Figure 7.5 – Charge gain as a function of ΔV_{THGEM} for different induction fields of the THGEM coupled to induction gaps with thicknesses of: (A) 400 μm, (B) 500 μm and (C) 800 μm.

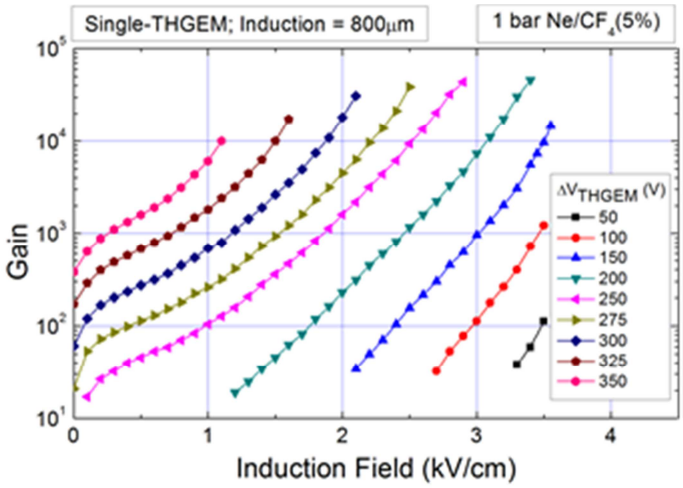

Figure 7.6 – Charge gain as a function of the induction field for different ΔV_{THGEM} bias and for 800 μm induction gap.

It can be seen from Figure 7.6 that for low induction fields (lower than ~1 kV/cm) there is a gradual increase of charge gain followed by a much steeper increase. This behavior is due, both, to an improved charge collection by the anode (higher electron extraction) and by the onset of gap multiplication. To reach the same gain value for increasing E_{Gap}, the required ΔV_{THGEM} was decreased. For example, for the E_{Gap} of ~1 kV/cm, the required ΔV_{THGEM} to reach gains of 10^4 was on the order of 350 V while for the E_{Gap} of 3.5 kV/cm it was only necessary to apply ΔV_{THGEM} of 150 V to reach the same gain values.

The transition from multiplication only inside the hole to multiplication also in the induction region is gradual which indicates that the avalanche region extends to outside of the hole into the induction region.

Figure 7.6 indicates a ~4 fold decrease in maximum gain for ΔV_{THGEM} increase from 200 V to 350 V. The maximum applied induction field was simultaneously reduced from ~3.5 kV to ~1.2 kV/cm, before the onset of occasional discharges. A fairly

constant maximum gain could be achieved for a wide range of ΔV_{THGEM}, between 200 and 300 V and corresponding induction fields between 3.5 and 2.1 kV/cm, respectively.

7.3.2 Energy resolution

Figure 7.7 depicts the energy resolution (%FWHM) for 5.9 keV X-rays as a function of the gain, for some values of the induction field, of a THGEM followed by an induction gap of 400 μm (Figure 7.7A), 500 μm (Figure 7.7B) and 800 μm (Figure 7.7C). After an initial fast decrease of the peak width with increasing gain, the energy resolution stabilized between ~25% and ~35%FWHM, degrading at higher gains, due to the onset of photon feedback. A trend observed is that low induction fields resulted in somewhat better energy resolution values, with a broader resolution plateau. The induction-field increase degraded the energy resolution, due to additional statistical fluctuations introduced by the gap multiplication process. In addition, the energy-resolution plateau is shortened and shifted towards higher gains. For the highest induction fields, the best energy resolutions ~30%FWHM were achieved for the 400 μm thick induction gap and ~35%FWHM for the larger gaps. The degradation of these energy resolutions occurred at gains above 1×10^4 with the 400 μm gap and above 6×10^4 for the larger ones, reaching at maximum gains values of 40-45%FWHM.

For comparison, the energy resolution obtained in a Single–THGEM [**49**] was ~25%FWHM for gains above 10^2, degrading to ~30%FWHM for gains above 2×10^3 and reaching roughly 40%FWHM close to a gain of 5×10^3. In the present configuration, a gain of 2×10^3 yielded energy resolutions of ~27%, 25% and 27%FWHM for multiplication gaps of 400, 500 and 800 μm, respectively.

The Double–THGEM setup in [**49**] yielded the best energy resolution of 25%FWHM at a gain of a few times 10^4. With the 400 μm induction gap this charge gain value was only reached for relatively high induction fields (5.7 kV/cm) with degraded energy resolution (~45%FWHM) – due to the high amplification in the induction region – while for the other investigated induction gaps lower induction field was required to reach the same gain but with some noticeable energy resolution degradation.

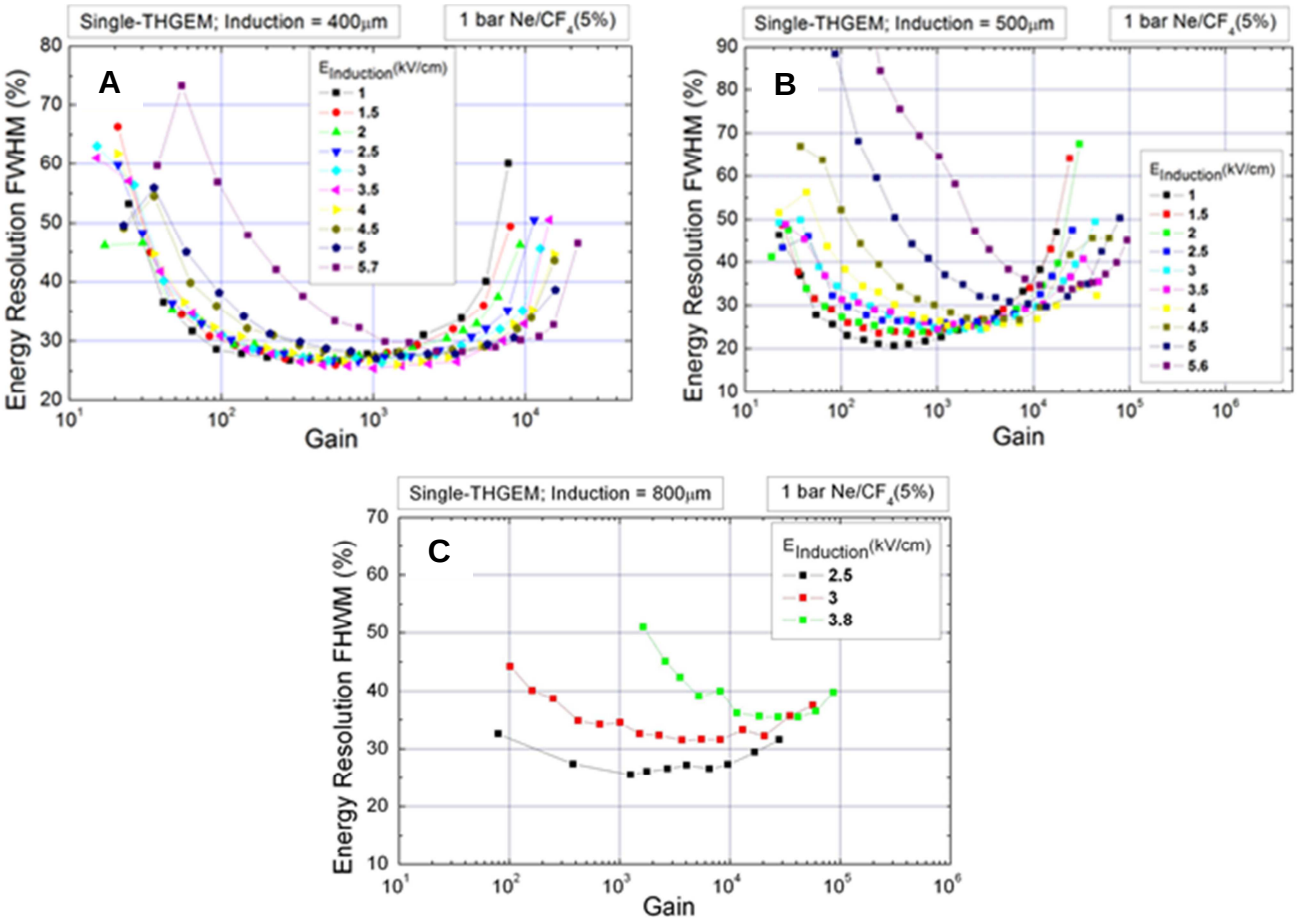

Figure 7.7 – Energy resolution of 5,9 keV X-rays as a function of charge gain for different values of induction fields applied across gaps of 400 μm (A), 500 μm (B) and 800 μm (C).

7.4 Methane mixtures with neon and argon

The results obtained for the THGEM coupled to a submillimetric induction gap operating in Ne-CF_4 mixtures have revealed the presence of photon-induced feedback effects, as VUV photons are produced in the electron avalanches on CF_4. This imposes a limitation for the maximum gains that could be achieved in the THGEM and/or in the

induction gap in those mixtures. As CH_4 does not scintillate in the VUV or UV range and CH_4 is an effective VUV quencher, the photon-feedback effect is reduced in Ne-CH_4 mixtures and, therefore, higher gains may be possible to be obtained in these mixtures. On the other hand, Ar-based mixtures are preferable over Ne-based ones for the detection of MIPs (minimum ionizing particles), since they present higher ionization yields and lower electron diffusion. However, the higher voltages needed to be applied to the THGEM are a drawback, a factor that can be, nevertheless, minimized coupling the THGEM to a submillimetric induction gap and using the charge multiplication in the induction gap to obtain high gains while applying lower voltages to the THGEM. To explore these ideas, we have investigated the operation of the THGEM coupled to a submillimetric induction gaps in Ne/CH_4(95:5) and Ar/CH_4(80:20) gas mixtures.

7.4.1 Charge gain characteristics

In Figure 7.8A and Figure 7.8B the avalanche charge gains that can be achieved with a THGEM coupled to a 0.5 mm and 0.8 mm induction gaps are presented, as a function of the THGEM voltage for different electric fields applied to the induction gap. In Figure 7.9A and Figure 7.9B the charge avalanche gain are depicted as a function of the electric field applied to the 0.5 mm thick induction gap for several values of voltage differences applied to the THGEM electrodes.

As can be seen, the presence of high electric fields in the induction gap allows achieving higher gains using lower applied voltages to the THGEM, almost a factor of ten higher when compared to the gains achieved for the typical electric field values usually applied to the induction gap, at a cost of a slightly higher overall voltage applied to the THGEM+induction region. Charge gains well above 10^5 are possible to be

achieved in Ne-5%CH_4. These gains can be almost one order of magnitude higher than those achieved in Ne-5%CF4 mixtures.

A remarkable fact is that Ar-20% CH_4 reaches gains that are only a factor of two lower than those obtained in Ne-5% CH_4. Nevertheless, the total voltage applied in Ar-20% CH_4 is about 1500 V, while for Ne-5% CH_4 it is still below 400 V. While for Ne-5% CH_4 mixture the effect of photon feedback seems to be present at higher voltages and, therefore a higher content of CH_4 may be used to further reduce the photon feedback, this effect is not present in the case of Ar-20% CH_4. For the Ar-CH_4 mixture it is possible to set induction fields as high as 16 kV/cm without having photon-feedback effects, due to the strong quenching effect of the 20% CH_4 content and to the high ionization threshold of this mixture.

The results also show that, for the studied mixtures, it is possible to achieve almost the same gains with the smaller induction gap thicknesses. This may present an advantage for the R&D that is being carried out to develop a thin element for the DHCAL calorimeter, since the induction gap can be reduced from 1 to 0.5 mm without sacrificing the gain that is possible to achieve, while also using lower applied voltages.

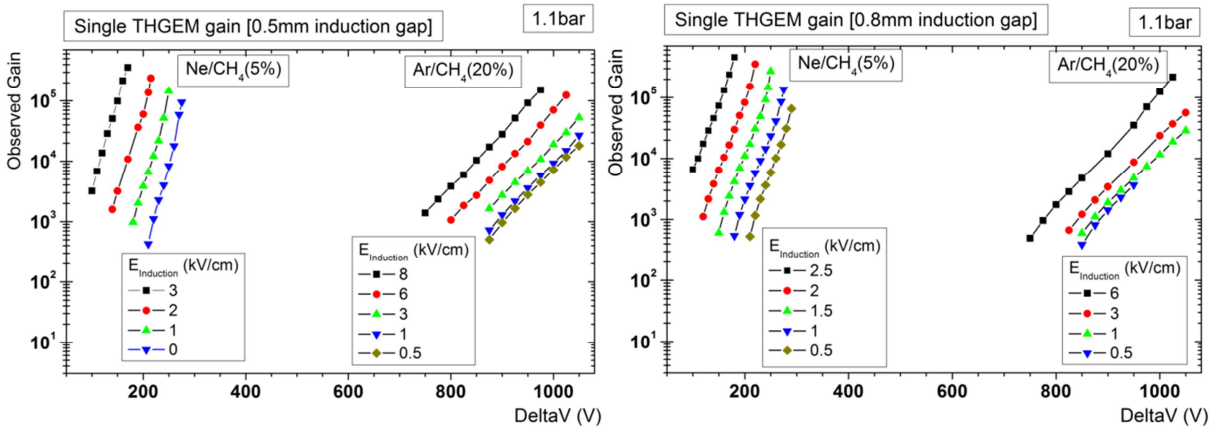

Figure 7.8 – Observed gain in $Ne/CH_4(5\%)$ and in $Ar/CH_4(20\%)$ with a single-stage THGEM coupled to a 0.5 mm induction gap (a) and 0.8 mm induction gap (b), as a function of the voltage difference applied to the THGEM electrodes for several values of induction field.

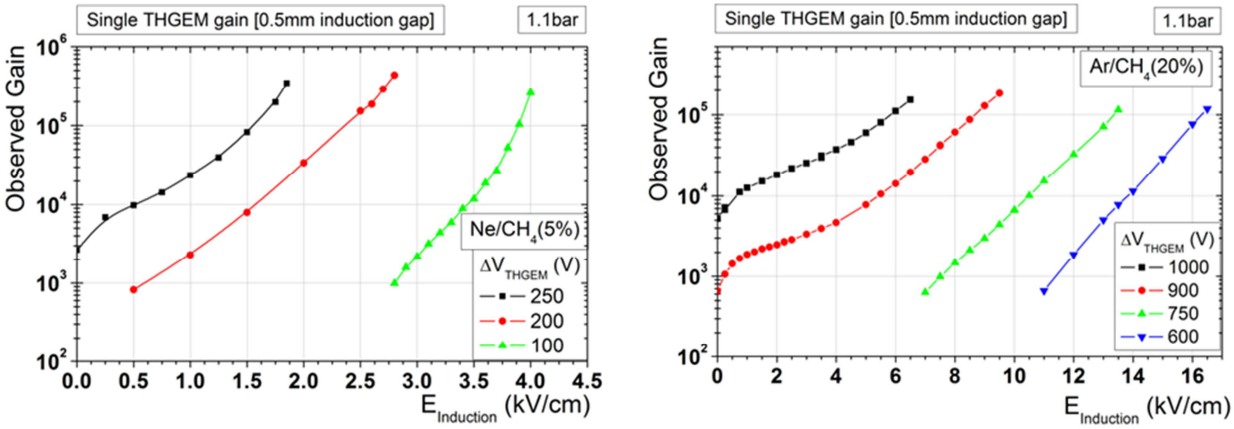

Figure 7.9 – Observed gain in $Ne/CH_4(95:5)$ and in $Ar/CH_4(80:20)$ with a single-stage THGEM coupled to a 0.5 mm induction gap, as a function of the induction field for several values voltage applied to the THGEM electrode.

7.4.2 Energy Resolution

Figure 7.10A and Figure 7.10B depict the energy resolution for 5.9 keV X-rays obtained with the THGEM coupled to 0.5 mm and 0.8 mm induction gaps, respectively, as a function of the THGEM voltage and for different electric fields applied to the induction gap. For Ne-5% CH_4 mixture it is noticeable a fast degradation of the energy resolution for the higher voltages between the THGEM electrodes, being this effect is more pronounced for the 0.8 mm induction gap.

In Figure 7.11 the energy resolutions obtained for 5.9 keV X-rays are depicted as a function of the gain, for the different electric field applied to the 0.5 mm thick induction gap. We note that while for Ne-5% CH_4 the threshold for charge multiplication is around 0.5 kV/cm, for pure Ar this value is about 3 kV/cm/bar and, therefore, for Ar-20% CH_4 mixture a significant charge multiplication is not achieved in the induction gap, even for the higher fields applied to this region. This results from the fact that there is not a large dependence of the achieved energy resolution on the electric field and justifies the absence of photon feedback effects. While the degradation of the energy resolution in Ne-CH_4 is due to the onset of the photon-feedback processes and to the much larger intensity of the electric field inside the holes, which results in the loss of some of the avalanche electrons to the THGEM bottom electrode, for the Ar-CH_4 mixture only the latter effect is present. As can be seen from Figure 7.11 there are no significant differences in the energy resolution achieved in both mixtures.

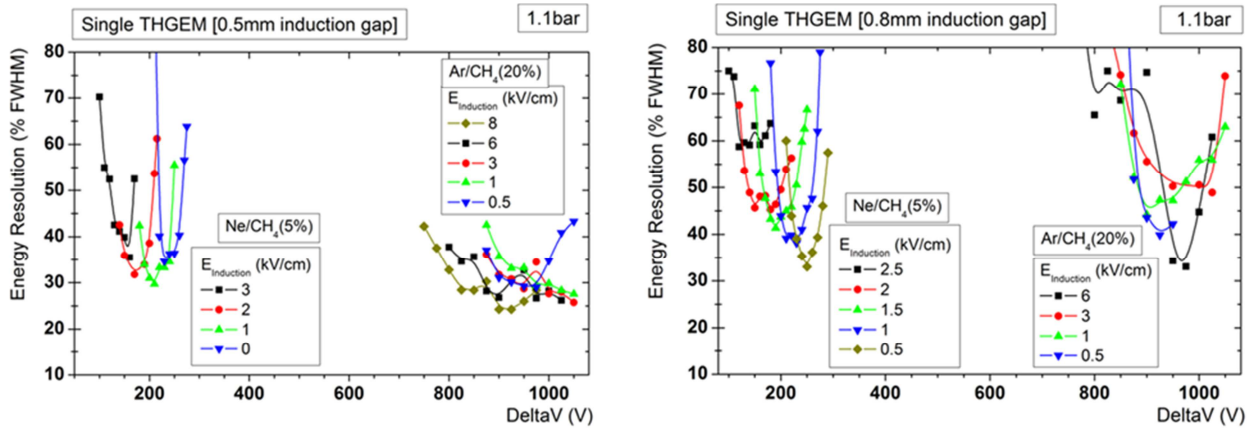

Figure 7.10 – Energy resolution (as % of FWHM) as a function of voltage difference across a THGEM electrode for 5.9 keV X-rays obtained with a single-stage THGEM coupled to a 0.5 mm induction gap (a) and 0.8 mm induction gap (b), in Ne/CH_4(5%) and in Ar/CH_4(20%), for several values of induction field.

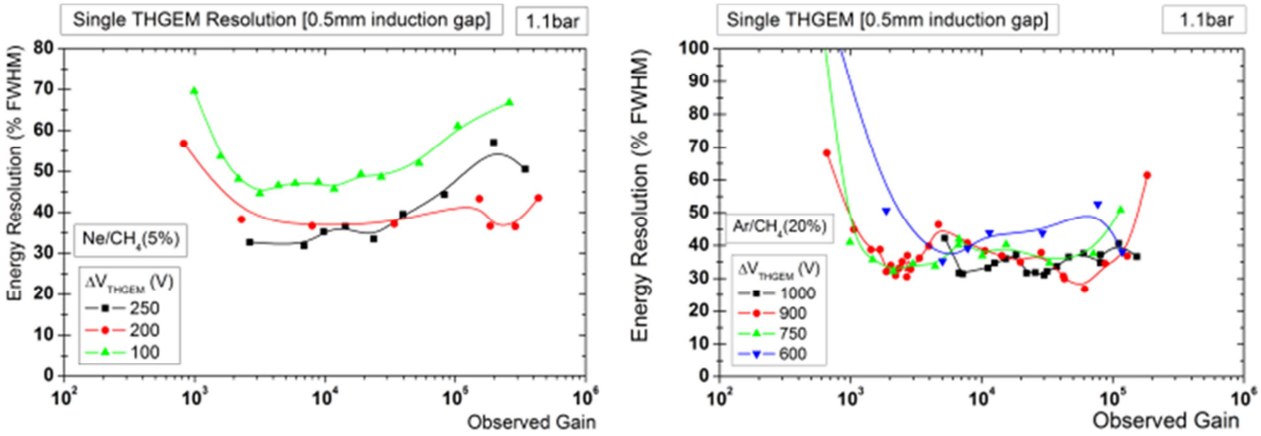

Figure 7.11 – Energy resolution (as % of FWHM) as a function of the observed gain for 5.9 keV X-rays obtained with a single-stage THGEM coupled to a 0.5 mm induction gap in Ne/CH_4(5%) and in Ar/CH_4(20%), for several voltages applied across the THGEM. The induction field was gradually increased for a set voltage across the THGEM.

7.5 Discussion

The characteristics of THGEM based detectors operated with additional multiplication in a submillimeter (400, 500 or 800 μm) induction gap were investigated in Ne/CF_4 (95:5). The charge gain and energy resolution were determined with 5.9 keV X-rays, as function of the applied bias to the THGEM and the induction gap.

Maximum gains of 10^5, similar to those obtained with a standard double-THGEM configuration operated in the same gas mixture, can be reached for induction gaps between 500 and 800 μm. The maximum respective applied gap-fields decreased from ~5.5 to ~3.8 kV/cm. The maximum gain limitation is due to poor VUV avalanche-photon quenching by CF_4, which also scintillates in the VUV. At higher inductions fields, gain-limiting photon-feedback effects occurs as the electron avalanche extends into the induction gap.

It was shown that, contrary to what was observed in the Ne-CF_4 mixtures, the Ne-CH_4 mixtures, having a more effective UV quenching, allowed achieving higher charge gains in stable operating conditions. Moreover, in Ne-CH_4 mixtures, with a 0.5 mm thick induction gap it is possible to achieve similar charge gains to those achieved in the 0.8 mm thick induction gaps. Therefore, it is possible to implement an effective reduction of the thickness of the thin elements to be developed for the calorimeter for the ILC, based on THGEMs. Using a submillimetric induction gap coupled to a THGEM operating in Ar-CH_4 mixtures, it is possible to achieve gains that are only a factor 2 lower than those achieved with Ne-CH_4 mixtures. This is very important for improving the SNR in the detection of MIPs as in Ar-based mixtures present higher ionization yields and lower electron diffusion coefficients, when compared to Ne-based

ones. Again, this is an important issue for the R&D research of thin elements for the future ILC.

We have shown that it is possible to conceive a relatively thin electron multiplier capable of reaching high gains. Further investigations are required to evaluate the performance of such thin detector elements with different gases and over larger areas. Compared to a regular THGEM followed with an induction-collection gap yielding fast electron signals, one has to investigate effects due to slower avalanche-ion components on the signals due to the transit of the positive ions across the gap. The latter may affect high-rate applications. The present concept may be evaluated as an alternative sampling element for Digital Hadron Calorimeter under development for ILC [**93**], where the detector thickness plays an important role. The possibility to reach high gains in this detector concept, reducing the gains on each of the two elements, will allow the use of low biasing voltages, below the respective maximum limits, thus minimizing the discharge probability.

The electric field profile has been computed for several electrostatic conditions in the 400 mm and 800 mm induction regions using Ansys 3D finite element simulation software. The simulations provided a valuable tool to determine the electric field strength on the several regions of the detector. They show that the full development of the charge avalanche of the THGEM extends into the induction gap for more than 200 mm even for induction electric fields well below the charge multiplication threshold, extending deeper inside the gap as the induction electric field increases. In each of the experimental measurements a clear decrease of the THGEM operation voltages was observed for increasing values of applied induction field accompanied by a significant increase of the charge gain, being more significant for larger induction gaps.

Chapter 8 – Helium mixtures with molecular gases

8.1 Introduction

He-based mixtures may present a good alternative to Ne-based mixtures for the potential higher gains [**30**], with lower applied voltages, similar photoelectron extraction efficiency and lower costs. The THGEM operation in Ne-CH_4 and -CF_4 mixtures have been extensively investigated [**94**] [**63**] [**30**] [**27**] [**95**] [**49**] [**50**], but the studies of He-based mixtures for THGEMs have not yet been done. To the best of our knowledge, only [**30**] have presented a single test with such mixture, referring to its potential advantages.

In this work we present experimental measurements on the collection efficiencies of photoelectrons emitted by CsI photocathodes operating in He-based mixtures and investigate the charge gain characteristics of THGEMs operating in He-based mixtures. The obtained results are compared with those obtained for Ne-based mixtures and a discussion on the potential use of He-based for future cryogenic applications will be presented. Main interest of these studies is related with the development of gas photomultipliers (GPM) for high-energy physics applications as an alternative to Ne-based mixtures, namely RICH detectors, e.g. [**63**] [**69**] [**96**], as well as for cryogenic applications, e.g. [**30**] [**95**].

In this experimental work we used a single THGEM produced from G-10 with 0.4 mm thickness and with a 0.02 mm copper clad on both sides. It had a hexagonal pattern of holes 0.3 mm in diameter, with a pitch of 1mm over an active area of 20 mm x 20 mm; the holes had a 0.05 mm wide chemically etched rims.

The THGEM was assembled in the experimental system described in detail in [JINST 8 P06004]. The detector was assembled inside a cylindrical stainless steel vessel evacuated down to 10^{-5}mbar prior to gas filling. The THGEM and the drift stainless-steel mesh (50 μm thick wires and with 500 μm pitch) and the copper induction plane were assembled on Teflon mountings. The drift and induction regions were 6 mm, and 2.3 mm respectively, as shown in Figure 8.1. The chamber was closed after gas filling and gas purity was maintained by circulation via convection through SAES St707 non-evaporable getters, heated to ~120ºC.

8.2 Charge gain measurements

In Figure 8.1 the experimental setup used for the effective gain determination is depicted. Charge-gain measurements were obtained with a Single-THGEM detector operating in these gas mixtures using a UV lamp for the extraction of photo-electrons. A 1000Å CsI photocathode was deposited on a gold plated THGEM for photo-electron conversion. Photoelectrons were extracted from the CsI film by incident 185 nm VUV photons emitted by an Oriel Hg(Ar) VUV lamp and are focused into the THGEM holes, due to the strong electric field present in vicinity of the holes.

Charge-gains in excess of 10^5 were obtained for gas mixtures containing percentages of quencher higher than 20%.

The THGEM gain was obtained from the ratio between the photocurrent extracted from the photocathode to the mesh without gas multiplication (as measured with the setup represented in Figure 8.5) and the current measured in the induction electrode after multiplication in the THGEM's holes (using the setup represented in Figure 8.1).

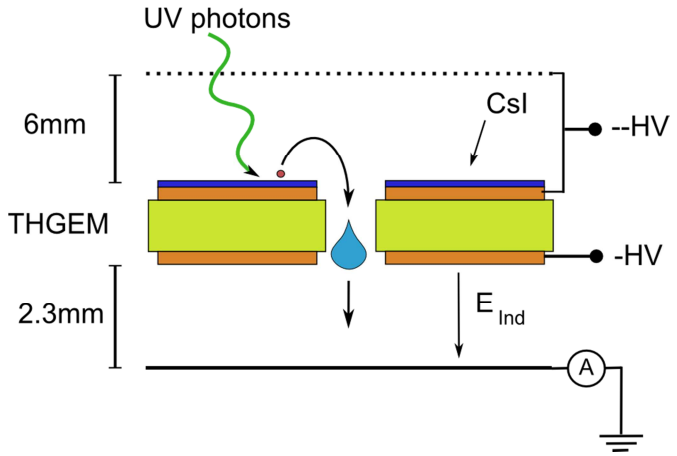

Figure 8.1 – Schematic of the experimental setups used for effective gain determination, highlighting applied bias, the CsI photocathode and the THGEM used.

In Figure 8.2 the obtained gain curves, measured in current mode, are represented for a Single-THGEM + CsI photocathode deposited on its top electrode, operated under different He/CF_4 mixtures. The effective gain is represented as a function of the voltage difference applied to the THGEM electrodes. In Figure 8.3 the results obtained with He/CH_4 mixtures are presented.

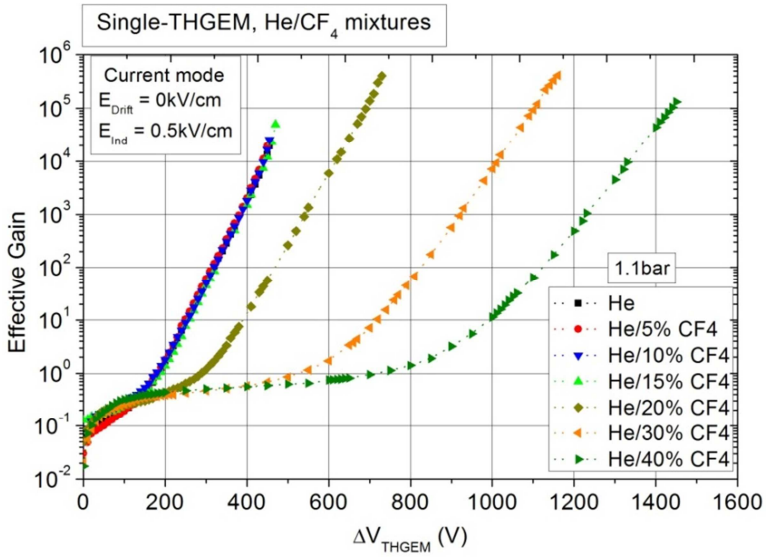

Figure 8.2 – Single-THGEM gain curves for several He/CF_4 mixtures, measured in current mode for photoelectrons emitted from a CsI photocathode coating the THGEM top electrode, illuminated by VUV photons peaking at 185 nm from a Hg(Ar) UV lamp.

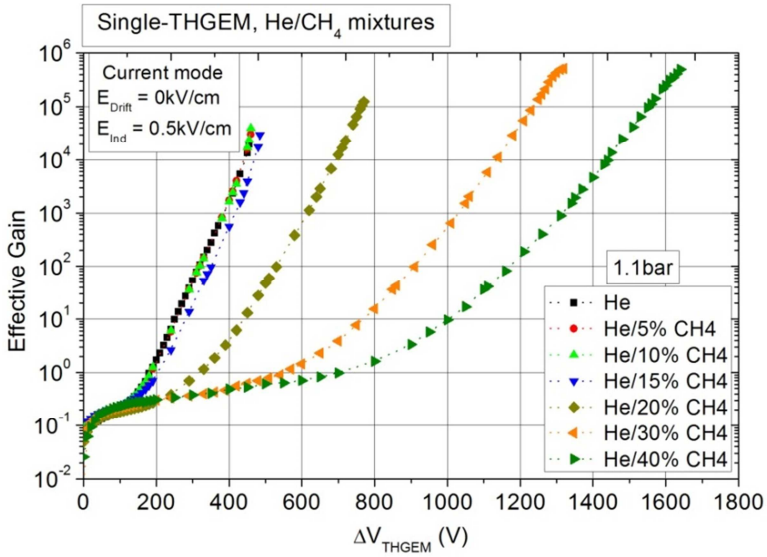

Figure 8.3 – Single-THGEM gain curves for several He/CF_4 mixtures, measured in current mode for photoelectrons emitted from a CsI photocathode coating the THGEM top electrode, illuminated by VUV photons peaking at 185 nm from a Hg(Ar) UV lamp.

As seen from Figure 8.2 and Figure 8.3, both types of gas mixtures allow reaching very high charge-gains, well above 10^5. Similar gains are obtained in both types of He-based mixtures but higher content of CH_4 and higher voltages are necessary: maximum gains are obtained for CF_4 content around the 20-30% while for CH_4 the content must be above 30%. This trend and the achieved gains are similar to those obtained in [**94**] [**63**] for THGEMs with similar parameters; the differences in the maximum applied voltages needed in the different cases may result from different levels of gas purity, as demonstrated in [**94**] and [**49**]. On the other hand, when compared to Ar-based mixtures [**94**] [**63**] [**96**] [**69**], He-based mixtures allow to achieve similar gains but needing lower voltages applied to the THGEM. Previous works [**94**] [**96**] [**69**] have shown that the maximum gains achieved in pulse mode, resulting from interactions of X-rays with energies in the keV range, are lower than those achieved in current mode, by a factor that can be up to one order of magnitude.

8.3 Photoelectron-extraction efficiency

Since few years, we have carried out an extensive program for the studied on the collection efficiencies of photoelectrons emitted by CsI photocathodes operating in gaseous atmospheres, noble gases and Ne-based mixtures. Compared to vacuum operation, the emitted photoelectrons may collide with the gas molecules and return to the photocathode. The effective quantum efficiency is, thus, reduced when the photocathode is operated inside a gas atmosphere. Therefore, the photoelectron collection efficiency is an important parameter to consider when deciding about the suitability of a gas. In Figure 8.4 the electron scattering cross sections in He, CF_4 and CH_4 as taken from various authors is shown, highlighting the elastic momentum transfer

as well as the inelastic momentum transfers, due to dissociative and electronic excitations, ionizations and vibrational excitations [**97**]. As can be seen, inelastic collisions of electrons with CF_4 and CH_4 molecules, due to the vibrational states of the molecules become important for electron energies above 0.1eV, decreasing the probability of photoelectron backscattering to the photocathode in He -CF_4 and -CH_4 mixtures, when compared to a pure He atmosphere. Helium presents higher elastic scattering cross sections when compared to Ne (e.g. see [**65**]), indicating that He-based mixtures may need higher concentrations of molecular additives to achieve the same photoelectron collection efficiencies.

The photoelectron collection efficiencies present high values in molecular gases, around 90%, since the photoelectron loses almost all its energy in non-elastic collisions with the molecule, transferring energy to rotational and vibrational states of the molecule, and will not have enough energy to overcome the electric field and return to the photocathode, upon a collision. On the other hand, for the monoatomic molecules of the noble gases only elastic collisions are allowed and the photoelectron will retain its energy to get back to the photocathode, upon a collision, resulting in poorer photoelectron collection efficiency, Therefore, the addition of a molecular gas will increase the photoelectron collection efficiency in the noble gas.

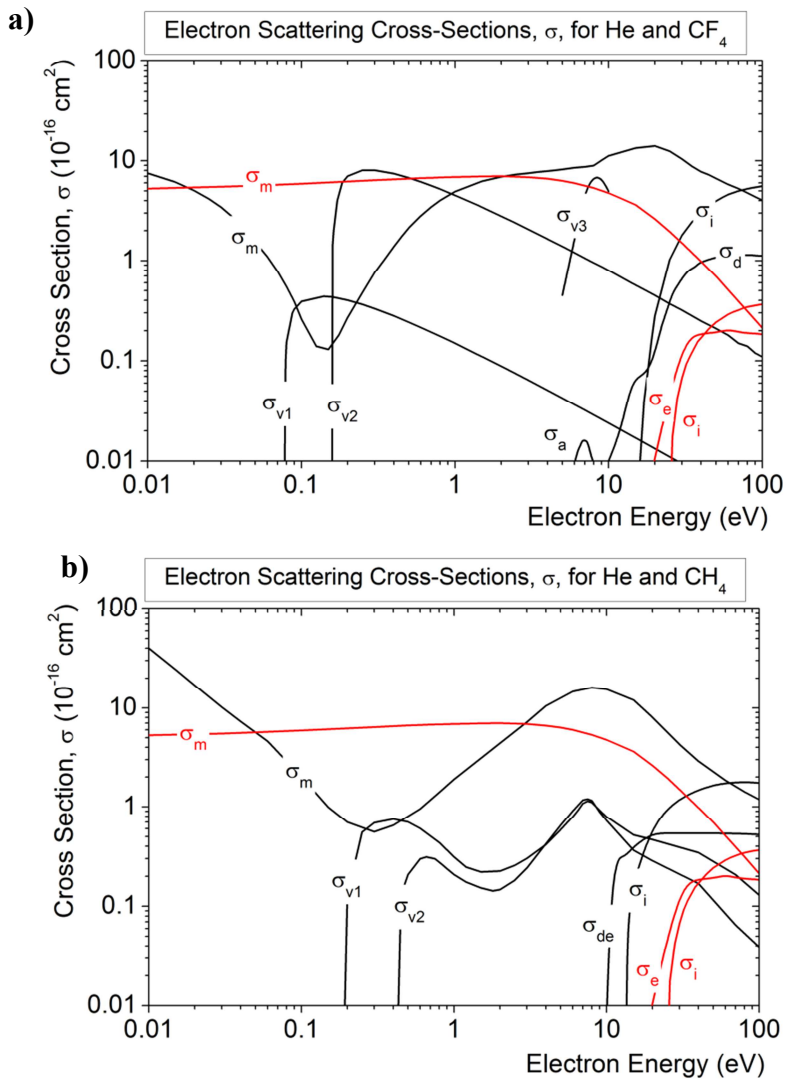

Figure 8.4 – Electron scattering cross-sections in a) He and CF_4 and b) He and CH_4, from various authors: elastic momentum transfer (σ_m), rotational excitation (σ_{rot}), vibrational excitation (σ_v), neutral dissociation (σ_d) dissociative excitation (σ_{de}) electronic excitation (σ_e), and ionization (σ_i).

This task presents the experimental efforts made for the measurements obtained for UV-induced photo-electron extraction efficiency from a CsI photocathode into He with CF_4 and CH_4 gas mixtures, when irradiated by VUV photons around 185 nm.

In Figure 8.5 the experimental setup used for extraction efficiency determination is represented. Photoelectrons were extracted from the CsI film by incident 185 nm VUV photons emitted by an Oriel Hg(Ar) VUV lamp and are collected in the mesh placed above the photocathode. The photoelectron currents were measured operating the photocathode in vacuum and in the gas for the different He-CF_4 and He-CH_4 as a function of the electric field applied in the region above the photocathode.

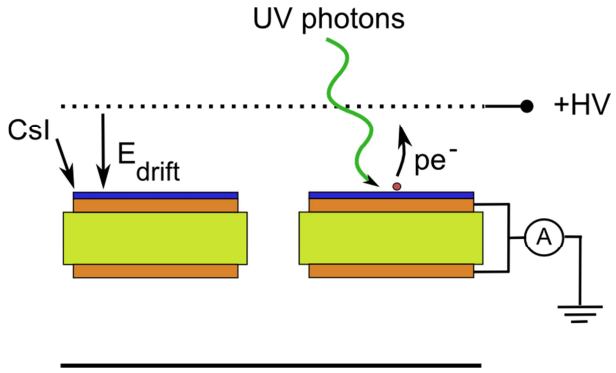

Figure 8.5 – Schematic of the experimental setups used for extraction efficiency determination.

In Figure 8.6 the measured photoelectron extraction efficiency from CsI into He and CF_4 mixtures are presented as a function of the electric field above the photocathode. In Figure 8.7 similar results are presented for He and CH_4 mixtures. The photoelectron extraction efficiency was obtained from the measured photoelectron currents in gas were normalized to the vacuum photoelectron current, i.e. the ratio of I_{gas}/I_{vacuum}.

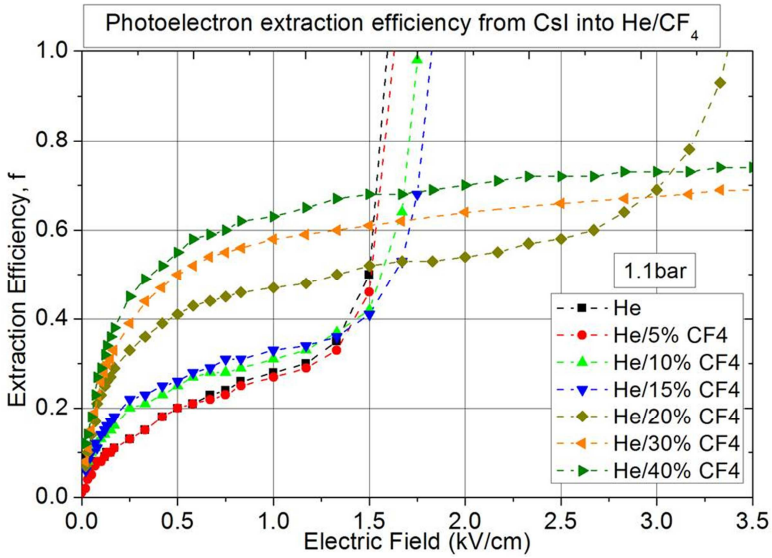

Figure 8.6 – Photoelectron extraction efficiency from CsI into several He and CF_4 gas mixtures as a function of the applied electric field in the region above the photocathode. UV photons peaking at 185 nm from a Hg(Ar) VUV lamp were used.

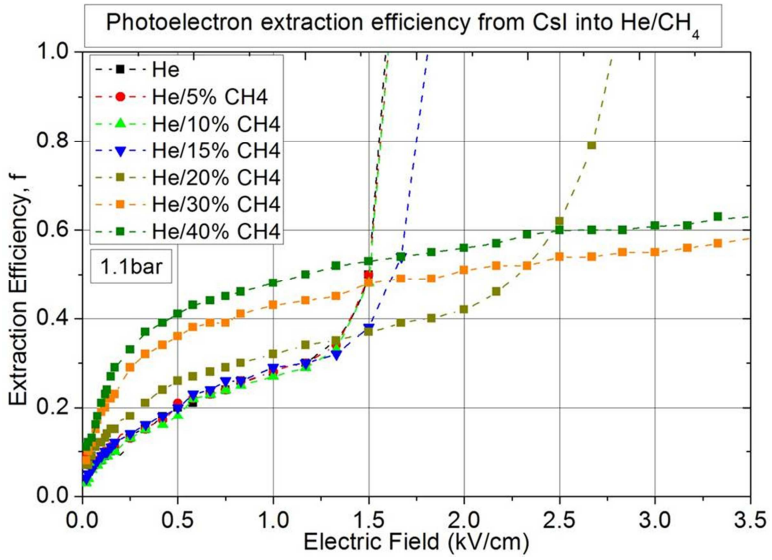

Figure 8.7 – Photoelectron extraction efficiency from CsI into several He and CH_4 gas mixtures as a function of the applied electric field. UV photons peaking at 185 nm from a Hg(Ar) VUV lamp were used.

As shown from Figure 8.6 and Figure 8.7, the addition of CF_4 to He is more effective than the addition of CH_4, in terms of the reduction of photoelectron backscattering, the same behavior as that found in Ne-based mixtures [**65**] [**94**] [**63**]. This is due to the fact that CF_4 presents lower energy thresholds for the vibrational excitations, resulting in the onset of inelastic collisions at lower photoelectron energies. However, more important is the fact that He-based mixtures present lower photoelectron extraction efficiencies than the Ne-base mixtures with the same molecular additive content. This is a consequence of the higher cross section presented by He for electron impact elastic collisions when compared to Ne. While for He-30%CH_4 mixture the photoelectron extraction efficiency is below 50% for electric fields lower than 2 kV/cm, in Ne-20%CH_4 it is already above 70% for electric fields above 1 kV/cm [**65**] [**94**].

8.4 Discussion

In this work a Single-THGEM detector was operated in He/CF_4 and He/CH_4 mixtures reaching effective charge-gains well above 10^5, measured in current mode. These gains are similar to those obtained with Ne/CF_4 and Ne/CH_4 in current mode and with THGEMs having similar geometric parameters. Both types of gas mixtures (He and Ne) allow reaching very high charge-gains, applying relatively low voltages when compared to Ar mixtures.

The maximal achievable charge-gains for photo-electrons in He/CF_4(20%) and He/CF_4(30%) gas mixtures, close to 10^6, are comparable to the maximal achievable charge-gains in [**63**], for Ne/CF_4 mixtures. On the other hand, the maximal charge-gains achievable in He/CH_4 30% and 40% gas mixtures, which are similar to the charge-gains reached in He/CF_4(20%) and He/CF_4(30%), are one order of magnitude higher than the

ones reached in the above work for Ne/CH_4 mixtures. Both types of gas mixtures (He and Ne) allow reaching very high charge-gains, well above 10^5 applying relatively low voltages, when compared to Ar mixtures.

The results obtained for the photo-electron extraction efficiency show that in He/CF_4 mixtures this parameter is high, reaching ~70% for a 2 kV/cm electric field on the surface of the photocathode and for He/40% CF_4. This value is lower than that of ~85%, obtained for the Ne/CF_4 mixtures. For He/CH_4 gas mixtures the photo-electron extraction efficiency is roughly 55%, while in Ne gas mixtures with CF_4 and CH_4, the photo-electron extraction efficiency can reach values above 80%. Therefore, in terms of photon detection there seems to be no advantage of He-based gas mixtures over Ne-based ones.

The well-known higher permeability of He through different materials, particularly through fused silica (a typical VUV transparent material used in GPM and vacuum PMT windows) when compared to that of other noble gases is, however, significantly lower in cryogenic temperatures as shown by the permeation rate, *K*, given in units of cm^3 of gas (N.T.P.) per second per cm^2 per mm thickness of material per unit pressure difference as a function of 1/T, represented in Figure 8.8 [**98**].

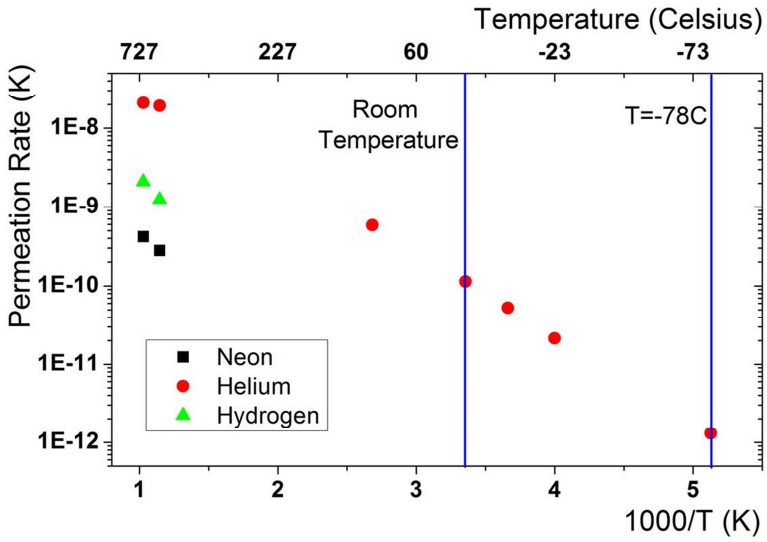

Figure 8.8 – Permeation rate, *K*, of helium, neon and hydrogen through fused silica at various temperatures.

This feature, combined with the promising results previously shown, opens the possibility of using He-based gas mixtures in cryogenic VUV gas photomultipliers.

Chapter 9 – Conclusions and future work

This thesis reports on important advancements regarding the development and testing of a large–area gaseous photomultiplier based on THGEMs operating close to liquid xenon temperature, integrated with pixel readout for event position identification. It was demonstrated the detection of both primary and secondary scintillation signals from a dual-phase LXe TPC with a large-area cryogenic gaseous photomultiplier. The detector configuration studied, employing a UV-transparent window and a reflective CsI photocathode deposited on the first amplification stage of a triple-THGEM detector, could potentially be suitable for photosensors located above the xenon vapor phase in such TPCs. A key observation in this respect was the GPM's ability to stably record signals over a very broad dynamic range: at a gain of ~10^5 the detector recorded both single photons and large S2 signals comprising thousands of photoelectrons, with a discharge probability of the order of 10^{-6}. The GPM's energy resolution for alpha particle S2 signals (~9% RMS) was shown to be equivalent to that of the XENON100 dual-phase detector equipped with PMTs, for the same number of ionization electrons (~8000). The RMS time resolution, derived from S1 signals, was demonstrated to be on the nanosecond scale for ~200 photoelectron signals.

Future work involves the determination of the photoelectron extraction efficiency of the CsI photocathode and the determination of its quantum efficiency in-situ at cryogenic temperatures. Since the current GPM design does not allow for such

measurements while inside WILiX, a major re-design was recently begun in order to install inside the GPM chamber an optical system. This optical system will involve an external UV-light source transmitting, through a solarization resistant optical fiber, a collimated light beam shinning on the CsI photocathode. The light intensity will be monitored via a UV photodiode and a UV beam splitter. This system will allow the measurement of the photocurrent from the CsI normalized to the light intensity.

Moreover, the contribution to the background radiation from the materials used in the THGEMs is still to be determined. Isotopes of thorium, uranium and potassium, mainly ^{232}Th, ^{238}U and ^{40}K may be present as impurities in the materials currently used in the THGEM manufacturing (glass fiber, copper and gold) and the total radioactivity of these will be determined in order to assess their applicability in current and future large scale low-background rare-event experiments.

Two particular challenges must be overcome to make GPMs a viable solution for future rare event experiments: (1) they must be made of radiopure materials, with radioactivity per unit area comparable to that of PMTs; (2) for pixilated GPMs, large-scale, radiopure cryogenic readout electronics should be developed. The first challenge can be addressed by replacing FR4 with low-radioactivity substrates such as Kapton (Cirlex), PTFE, or PEEK. Since these have intrinsic ^{238}U, ^{232}Th and ^{40}K radioactivity levels on the order of 10^{-5} – 10^{-3} mBq/cm^2 for ~0.5 mm thick plates (based on screening campaigns such as [**99**] [**100**] [**101**], their total radioactivity should be at most on the mBq scale in a 150×150 mm^2 GPM module with cascaded THGEM electrodes. Other candidate materials are glass–fiber laminate materials where the typical glass fibers are replaced by pure (>99.9%) silica grade fabrics, like Astroquartz®.

While care must be taken not to introduce external radioactivity during the production process of the electrodes, one should note that Cu-clad PTFE and Kapton sheets have typical radiopurity of the same order of magnitude as the bare materials

[**101**] [**102**]. Additional GPM structural materials, such as the window and metal case, can also be expected to have low radioactive content (in particular – high quality quartz has similar radiopurity as PTFE [**99**]). As for the readout electronics, both issues (cryogenic operation and radiopurity) are engineering-wise solvable.

As a final note, THGEM-based GPMs are currently being developed for recording primary scintillation in single-phase LXe detectors for neutron and gamma imaging [**103**] [**104**]. They may also be used in conjunction with Liquid Hole-Multipliers (LHMs), developed in parallel in Prof. Amos Breskin group, as potential sensors for large-scale single-phase TPCs [**67**] [**105**] [**106**].

References

[1] H. M. Araujo, V. Y. Chepel, M. I. Lopes, J. van der Marel, R. F. Marques, A. J. P. L. Policarpo, "Study of bialkali photocathodes below room temperature in the UV/VUV region," *IEEE Transactions on Nuclear Science*, vol. 45, no. 3, pp. 542-549, Jun 1998.

[2] M. Suyama, K. Nakamura, "Recent progress of photocathodes for PMTs," in *Proceedings of the International Workshop on New Photon Detectors*, Matsumoto, Japan, 2009.

[3] E. Aprile, M. Beck, K. Bokeloh, R. Budnik, B. Choi, H. A. Contreras, K.-L. Giboni, L. W. Goetzke, R. F. Lang, K. E. Lim, A. J. Melgarejo Fernandez, G. Plante, A. Rizzo, P. Shagin, C. Weinheimer, "Measurement of the Quantum Efficiency of Hamamatsu R8520 Photomultipliers at Liquid Xenon Temperature," *JINST 7 P10005*, July 2012.

[4] D. S. Akerib, X. Bai, E. Bernard, A. Bernstein, A. Bradley, D. Byram, S.B. Cahn, M.C. Carmona-Benitez, D. Carr, J.J. Chapman, Y-D. Chan, K. Clark, T. Coffey, L. deViveiros, M. Dragowsky, E. Druszkiewicz, B. Edwards, C. H. Faham, S. Fiorucci et al, "An Ultra-Low Background PMT for Liquid Xenon Detectors," *Nuclear Instruments and Methods in Physics Research Section A*, vol. 703, pp. 1-6, March 2013.

[5] K. Lung, K. Arisaka, A. Bargetzi, P. Beltrame, A. Cahill, T. Genma, C. Ghag, D. Gordon, J. Sainz, A. Teymourian, Y. Yoshizawa, "Characterization of the Hamamatsu R11410-10 3-Inch Photomultiplier Tube for Liquid Xenon Dark

Matter Direct Detection Experiments," *Nuclear Instruments and Methods in Physics Research Section A*, vol. 696, p. 32, 2012.

[6] D. Renke, E. Lorenz, "Advances in solid state photon detectors," *JINST 4 P04004*, 2009.

[7] N. Otte, "The Silicon Photomultiplier - A new device for High Energy Physics, Astroparticle Physics, Industrial and Medical Applications," in *Proceedings of the International Symposium on Detector Development for Particle, Astroparticle and Synchrotron Radiation Experiments (SNIC 2006)*, Menlo Park, California, 2006.

[8] S. Catalanotti, A. G. Cocco, G. Covone, M. D Incecco, G. Fiorillo, G. Korga, B. Rossi, S. Walker, "Performance of a SensL-30035-16P Silicon Photomultiplier array at liquid argon temperature," *JINST 10 P08013*, 2015.

[9] A. Fukasawaa, K. Arisakab, H. Wangb, M. Suyamaa, "QUPID, a single photon sensor for extremely low radioactivity," *Nuclear Instruments and Methods in Physics Research Section A*, vol. 623, no. 1, pp. 270-272, November 2010.

[10] A. Teymourian, D. Aharoni, L. Baudis, P. Beltrame, E. Brown, D. Cline, A.D. Ferella, A. Fukasawa, C.W. Lam, T. Lim, K. Lung, Y. Meng, S. Muramatsu, E. Pantic, M. Suyama, H. Wang, K. Arisaka, "Characterization of the QUartz Photon Intensifying Detector (QUPID) for Noble Liquid Detectors," *Nuclear Instruments and Methods in Physics Research Section A*, vol. 654, pp. 184 - 195, May 2011.

[11] A. Braem, M. Davenport, D. di Bari, A. Di Mauro, D. Elia, B. Goret, P. Martinengo, E. Nappi, G. Paic, J.C. Santiard, S. Stucchi, G. Tomasicchio, T.D. Williams for the ALICE collaboration F. Piuz, "Final tests of the CsI-based ring imaging detector for the ALICE experiment," *Nuclear Instruments and Methods in Physics Research A* , no. 433, pp. 178 - 189, 1999.

[12] G. Charpak, R. Bouclier, T. Bressani, J. Favier, Č. Zupančič, "The use of multiwire proportional counters to select and localize charged particles," *Nuclear Instruments and Methods*, vol. 62, pp. 262 - 268, July 1968.

[13] G. Charpak, P. Fonte, V. Peskov, F. Sauli, D. Scigocki, D. Stuart, "Investigation of operation of a parallel-plate avalanche chamber with a CsI photocathode under high gain conditions," *Nuclear Instruments and Methods in Physics Research A*, vol. 307, pp. 63 - 68, 1991.

[14] P. Fonte, T. Francke, N. Pavlopoulos, V. Peskov, I. Rodionov, "Novel single photon detectors for UV imaging," *Nuclear Instruments and Methods in Physics Research A*, vol. 553, pp. 30 - 34, 2005.

[15] R. Chechik, A. Breskin, "Advances in Gaseous Photomultipliers," *Nuclear Instruments and Methods in Physics Research A*, no. 595, pp. 116-127, 2008.

[16] F. Sauli, "GEM: A new concept for electron amplification in gas detectors," *Nuclear Instruments and Methods in Physics Research A*, vol. 386, pp. 531 - 534, 1997.

[17] F. Sauli, "Imaging with the gas electron multiplier," *Nuclear Instruments and Methods in Physics Research Section A*, vol. 580, no. 2, pp. 971 - 973, October 2007.

[18] R. Chechik, A. Breskin, C. Shalem, D. Mormann, "Thick GEM-like hole multipliers: Properties and possible applications," *Nuclear Instruments and Methods in Physics Research Section A,* vol. 535, no. 1 - 2, pp. 303 - 308, December 2004.

[19] M. Cortesi, R. Alon, R. Chechik, A. Breskin, D. Vartsky, V. Dangendorf, "Investigations of a THGEM-based imaging detector," *Journal of*

Instrumentation, vol. 2, September 2007.

[20] J. F. C. A. Veloso, J. M. F. dos Santos, C. A. N. Conde, "A proposed new microstructure for gas radiation detectors: The microhole and strip plate," *Review of Scientific Instruments*, vol. 71, pp. 2371 - 2376, June 2000.

[21] H. Natal da Luz, A. L. Gouvêa, J. A. Mir, J. M. F. dos Santos, J. F. C. A. Veloso, "The 2D-Micro Hole & Strip Plate in CF4 atmosphere aiming neutron imaging," *Journal of Instrumentation*, vol. 4, December 2009.

[22] F. D. Amaro; C. Santos; J. F. C. A. Veloso; A. Breskin; R. Chechik; J. M. F. dos Santos, "The Thick-COBRA: a new gaseous electron multiplier for radiation detectors," *Journal of Instrumentation*, vol. 5, Ocotober 2010.

[23] T. Boutboul, A. Buzulutskov, R. Chechik, G. Garty, E. Shefer, B.K. Singh A. Breskin, "Advances in gas avalanche photomultipliers," *Nuclear Instruments and Methods in Physics Research section A*, no. 442, pp. 58 - 67, 2000.

[24] A. Bondar, A. Buzulutskov, A. Dolgov, A. Grebenuk, E. Shemyakina, a. Sokolov, D. Akimov, A. Breskin, D. Thers, "Two-phase Cryogenic Avalanche Detectors with THGEM and hybrid THGEM/GEM multipliers operated in Ar and Ar+ N2," *Journal of Instrumentation*, vol. 8, February 2013.

[25] B. Lopez Paredes, C. D. R. Azevedo, S. Paganis, A. L. M. Silva, N. J. C. Spooner, J. F. C. A. Veloso, "Cryogenic Gaseous Photomultiplier for Position Reconstruction of Liquid Argon Scintillation Light," *Journal of Instrumentation*, vol. 10, July 2015.

[26] Wenqing Xie, Yidong Fu, Yulan Li, Jin Li, Yuanjing Li, Qian Yue, "Cryogenic THGEM–GPM for the readout of scintillation light from liquid argon," *Nuclear Instruments and Methods in Physics Research Section A: Accelerators,*

Spectrometers, Detectors and Associated Equipment, vol. 774, pp. 120 - 126, February 2015.

[27] V. Peskov, M. Cortesi, R. Budnik, R. Chechik, S. Duval, D. Thers, A. E. C. Coimbra, J. M. F. dos Santos, J. A. M. Lopes, C. D. R. Azevedo, J. F. C. A. Veloso A. Breskin, "CsI-THGEM gaseous photomultipliers for RICH and noble-liquid detectors," in *Proceedings of the 7th International Workshop on Ring Imaging Cherenkov Detectors*, Cassis, Provence, France, 2011, pp. 117 - 120.

[28] A. Bondar, A. Buzulutskov, A. Grebenuk, D. Pavlyuchenko, R. Snopkov, Y. Tikhonov, "First results of the two-phase argon avalanche detector performance with CsI photocathode," *Nuclear Instruments and Methods in Physics Research Section A*, vol. 581, no. 1 - 2, pp. 241 - 245, October 2007.

[29] S. Duval, A. Breskin, R. Budnik, W. T. Chen, H Carduner, M. Cortesi, J. P. Cussonneau, J. Donnard, J. Lamblin, P. Le Ray, E. Morteau, T. Oger, J. S. Stutzmann, D. Thers, "On the operation of a micropattern gaseous UV-photomultiplier in liquid-Xenon," *Journal of Instrumentation*, vol. 6, April 2011.

[30] L. Arazi, A. Breskin, R. Budnik, W-T Chen, H. Carduner, A. E. C. Coimbra, M. Cortesi, R. Kaner, J-P Cussonneau, J. Donnard, J. Lamblin, O. Lemaire, P. Le Ray, J. A.M. Lopes, A-F Mohamad Hadi, E. Morteau, T. Oger, J. M. F. dos Santos et al S. Duval, "Hybrid Multi Micropattern Gaseous Photomultiplier for detection of liquid-xenon scintillation," *Nuclear Instruments and Methods in Physics Research Section A*, vol. 695, pp. 163 - 167, December 2012.

[31] U. Asaf, I. T. Steinberger, "Photoconductivity and electron transport parameters in liquid and solid xenon," *Physical Review B*, vol. 10, no. 10, pp. 4464 - 4468, November 1974.

[32] M. J. Berger, J. S. Coursey, M. A. Zucker, J. Chang. National Institute of Standards and Technology - ESTAR, PSTAR, and ASTAR. [Online]. http://www.nist.gov/pml/data/star/index.cfm

[33] M. J. Berger, J. H. Hubbell, S. M. Seltzer, J. Chang, J. S. Coursey, R. Sukumar, D. S. Zucker, K. Olsen. National Institute of Standards and Technology - XCOM: Photon Cross Sections Database. [Online]. http://www.nist.gov/pml/data/xcom/

[34] P. Rinard, "Neutron Interaction with Matter," in *Passive Nondestructive Assay of Nuclear Materials*, N. Ensslin, H. Smith Jr. D. Reilly, Ed.: Nuclear Regulatory Commission, NUREG/CR-5550, 1991, ch. 12, p. 357.

[35] Evaluated Nuclear Data File (ENDF) - National Nuclear Data Center. [Online]. https://www-nds.iaea.org/exfor/endf.htm

[36] R. L. Platzman, "Total ionization in gases by high-energy particles: An appraisal of our understanding," *International Journal of Applied Radiation and Isotopes*, vol. 10, no. 2 - 3, pp. 116 - 127, 1961.

[37] E. Shibamura, "Drift velocities of electrons, saturation characteristics of ionization and W-values for conversion electrons in liquid argon, liquid argon-gas mixtures and liquid xenon," *Nuclear Instruments and Methods in Physics Research Section A*, vol. 131, pp. 249 - 258, 1975.

[38] T. Takahashi, S. Konno, T. Hamada, M. Miyajima, S. Kubota, A. Nakamoto, A. Hitachi, E. Shibamura, T. Doke, "Average energy expended per ion pair in liquid xenon," *Physical Review A*, vol. 12, no. 5, p. 1771, November 1975.

[39] Joshua Jortner, Lothar Meyer, Stuart A. Rice, E. G. Wilson, "Localized Excitations in Condensed Ne, Ar, Kr and Xe," *Journal of Chemical Physics*, vol. 42, no. 12, p. 4250, 1964.

[40] N. Schwentner, E-E Koch, J Jortner, *Electronic Excitations in Condensed Rare Gases*.: Springer-Verlag Berlin and Heidelberg GmbH & Co. K, 1985.

[41] S. Kubota, M. Hishida, J. Raun, "Evidence for a triplet state of the self-trapped exciton states in liquid argon, krypton and xenon," *Journal of Physics C: Solid State Physics*, vol. 11, no. 12, p. 2645, 1978.

[42] A. Hitachi, T. Takahashi, N. Funayama, K. Masuda, J. Kikuchi, T. Doke, "Effect of ionization density on the time dependence of luminescence from liquid argon and xenon," *Physical Review B*, vol. 27, p. 5279, May 1983.

[43] E. Aprile, C.E. Dahl, L. DeViveiros, R. Gaitskell, K.L. Giboni, J. Kwong, P. Majewski, K. Ni, T. Shutt, M. Yamashita, "Simultaneous Measurement of Ionization and Scintillation from Nuclear Recoils in Liquid Xenon as Target for a Dark Matter Experiment," *Physical Review Letters*, vol. 97, January 2006.

[44] K. Yoshino, U. Sowada, W. F. Schmidt, "Effect of molecular solutes on the electron drift velocity in liquid Ar, Kr, and Xe," *Physical Review A*, vol. 14, no. 1, p. 438, July 1976.

[45] P. Benetti, A. Bettini, E. Calligarich, F. Casagrande, P. Casoli, C. Castagnoli, P. Cennini, S. Centro, S. Cittolin, D. Cline C. De Vecchi, R. Dolfini, L. Fortson, A. Gigli Berzolari, G. Mannocchi, F. Mauri, L. Mazzone, C. Montanari, S. Otwinowski et al, "A simple and effective purifier for liquid xenon," *Nuclear Instruments and Methods in Physics Research Section A*, vol. 329, no. 1 - 2, pp. 361 - 364, May 1993.

[46] L. S. Miller, S. Howe, W. E. Spear, "Charge Transport in Solid and Liquid Ar, Kr, and Xe," *Physical Review Letters*, vol. 166, no. 3, pp. 871 - 878, February 1968.

[47] M. H. Cohen, J. Lekner, "Theory of Hot Electrons in Gases, Liquids, and Solids,"

Physical Review Letters, vol. 158, no. 2, p. 305, June 1967.

[48] E. Aprile, T. Doke, "Liquid xenon detectors for particle physics and astrophysics," *Reviews of Modern Physics*, vol. 82, no. 3, p. 2053, July 2010.

[49] A. E. C. Coimbra, A. Breskin, J. M. F. dos Santos, "THGEM operation in high pressure Ne/CF4," in *Proceedings of the 2nd International Conference on Micro Pattern Gaseous Detectors*, vol. 7, Kobe, Japan, February 2012, p. C02062.

[50] A. E. C. Coimbra, A. S. Conceição, J. A. Mir, A. Rubin, M. Pitt, A. Breskin, C. A. O. Henriques, J. M. F. dos Santos, "First results with THGEM followed by submillimetric multiplying gap," *Journal of Instrumentation*, no. P06004, June 2013.

[51] V. Peskov, D. Scigocki G. Charpak, "Study of BaF2 calorimeters in future hadron colliders," in *Proceedings of the 8th workshop of the INFN-ELOISATRON project on perspectives for new detectores in future supercolliders*, Erice, Italy, 1989.

[52] CERN RD26 Collaboration, H. Berger, P. Besson, P. Bourgeois, A. Braem, A. Breskin, A. F. Buzulutskov, R. Chechik, E. G. Chesi, C. Coluzza, R. F. Marques, J. Friese, A. R. Gillman, H. A. Gustafsson, V. Hejny, J. Homolka, W. Kühn, A. Ljubicic et al, "Recent results on the properties of CsI photocathodes," in *Proceedings of the Sixth Pisa Meeting on Advanced Detectors*, Pisa, Italy, 1995, pp. 411 - 415.

[53] CERN RD26 Collaboration, J. Almeida, A. Amadon, P. Besson, P. Bourgeois, A. Braem, A. Breskin, A. Buzulutskov, R. Chechik, C. Coluzza, A. DiMauro, J. Friese, J. Homolka, F. Iacovella, A. Ljubicic, G. Margaritondo, Ph. Miné, E. Nappi, T. dell'Orto et al, "Review of the development of cesium iodide photocathodes for application to large RICH detectors," in *Proceedings of the 7th*

International Wire Chamber Conference, Vienna, Austria, 1995, pp. 332 - 336.

[54] ALICE HMPID Group Collaboration, A. Braem, M. Davenport, A. Di Mauro, B. Goret, G. Paic, F. Piuz, J. Raynaud, J. C. Santiard, S. Stucchi, T. D, Williams, N. Colonna, D. Di Bari, D. Elia, R. Fini, L. Galantucci, B. Ghidini, A. Grimaldi, E. Monno et al, "A progress report on the development of the CsI-RICH detector for the ALICE experiment at LHC," *Nuclear Instruments and Methods in Physics Research A* , vol. 409, pp. 385 - 389, 1998.

[55] R. T. Poole, J. G. Jenkin, J. Liesegang, R. C. G. Leckey, "Electronic band structure of the alkali halides. I: Experimental parameters," *Physical Review B*, vol. 11, no. 12, pp. 5179 - 5189, June 1975.

[56] A. Buzulutskov, A. Breskin, R. Chechik, "Photoemission through thin dielectric coating films," *Journal of Applied Physics* , vol. 81, no. 1, p. 466, 1997.

[57] R. Triloki, Nikita Gupta, Nabeel F.A. Jammal, B.K. Singh, "Photoemission and optical constant measurements of a Cesium Iodide thin film photocathode," *Nuclear Instruments and Methods in Physics Research Section A*, vol. 787, pp. 161 - 165, 2014.

[58] W. E. Spicer, "Photoemissive, Photoconductive, and Optical Absorption Studies of Alkali-Antimony Compounds," *Physical Review*, vol. 112, no. 1, pp. 114 - 122, October 1958.

[59] W. E. Spicer, A. Herrera-Gomez, "Modern theory and applications of photocathodes," in *Proceedings of the International Society for Optical Engineering (SPIE) Symposium on Optics, Imaging and Instrumentation*, San Diego, October 1993, pp. 18 - 35.

[60] C. N. Berglund, W. E. Spicer, "Photoemission Studies of Copper and Silver:

Theory," *Physical Review Letters*, vol. 136, no. 4A, pp. A1030 - A1044, November 1964.

[61] A. Buzulutskov, A. Breskin, R. Chechik, "Heat enhancement of the photoyield from CsI, NaI and CuI photocathodes," *Nuclear Instruments and Methods in Physics Research A*, vol. 366, no. 2, pp. 410 - 412, December 1995.

[62] A. S. Tremsin, O. H. W. Siegmund, "Heat enhancement of radiation resistivity of evaporated CsI, KI and KBr photocathodes," *Nuclear Instruments and Methods in Physics Research Section A*, vol. 442, no. 1 - 3, pp. 337 - 341, March 2000.

[63] C. D. R. Azevedo, M. Cortesi, A. V. Lyashenko, A. Breskin, R. Chechik, J. Miyamoto, V. Peskov, J. Escada, J. F. C. A. Veloso, J. M. F. dos Santos, "Towards THGEM UV-photon detectors for RICH: on single-photon detection efficiency in Ne/CH4 and Ne/CF4," in *Proceedings of the 1st International Conference on Micro-Pattern Gaseous Detectors, Kolympari, Crete, Greece*, vol. 5, Crete, January 2010, p. P01002.

[64] MAXWELL 3D, ANSOFT Co, Pittsburgh, PA, USA.

[65] J. Escada, L. C. C. Coelho, T. H. V. T. Dias, J. A. M. Lopes, J. M. F. dos Santos, A. Breskin, "Measurements of photoelectron extraction efficiency from CsI into mixtures of Ne with CH4, CF4, CO2 and N2," *Journal of Instrumentation*, vol. 4, no. P 11025, November 2009.

[66] L. C. C. Coelho, J. A. M. Lopes, J. Escada, T. H. V. T. Dias, J.M.F. dos Santos, "Photoelectron transmission efficiency in Ar-CH4 and Xe-CH4 mixtures: Experimental results," *Nuclear Instruments and Methods in Physics Research Section A*, vol. 607, no. 3, pp. 587 - 590, August 2009.

[67] L. Arazi, A. E. C. Coimbra, R. Itay, H. Landsman, L. Levinson, M. L. Rappaport,

D. Vartsky, A. Breskin, "First observation of liquid-xenon proportional electroluminescence in THGEM holes," in *Proceedings of the 3rd International Conference on Micro Pattern Gaseous Detectors (MPGD2013)*, vol. 8, Zaragoça, Spain, December 2013, p. C12004.

[68] M. Alexeev, R. Birsa, F. Bradamante, A. Bressan, M. Chiosso, P. Ciliberti, S. Dalla Torre, O. Denisov, V. Duic, A. Ferrero, M. Finger, M. Finger Jr, H. Fischer, M. Giorgi, B. Gobbo, F.H. Heinsius, F. Herrmann, K. Königsmann, D. Kramer, L. Lauser et al, "Progress towards a THGEM-based detector of single photons," *Nuclear Instruments and Methods in Physics Research Section A*, vol. 639, no. 1, pp. 130 - 133, May 2011.

[69] M. Alexeev, M. Alfonsi, R. Birsa, F. Bradamante, A. Bressan, M. Chiosso, P. Ciliberti, G. Croci, M. L. Colantoni, S. Dalla Torre, O. Denisov, S. Duarte Pinto, V. Duic, A. Ferrero, M. Finger, M. Finger Jr, H. Fischer, G. Giacomini, M. Giorgi et al, "Development of THGEM-based photon detectors for Cherenkov Imaging Counters," *Journal of Instrumentation*, vol. 5, no. P03009, March 2010.

[70] E. M. Gushchin, A. A. Kruglov, I. M. Obodovskii, "Electron dynamics in condensed argon and xenon," *Journal of Experimental and Theoretical Physics*, vol. 55, no. 4, p. 650, April 1982.

[71] M. Blatnik, K. Dehmelt, A. Deshpande, D. Dixit, N. Feege, T. K. Hemmick, B. Lewis, M. L. Purschke, W. Roh, F. Torales-Acosta, T. Videbaek, S. Zajac, "Performance of a Quintuple-GEM Based RICH Detector Prototype," *Instrumentation and Detectors*, no. arXiv:1501.03530v2, January 2015.

[72] V. Chepel, H. Araújo, "Liquid noble gas detectors for low energy particle physics," *Journal of Instrumentation*, vol. 8, no. R04001, April 2013.

[73] The XENON100 dark matter experiment, E. Aprile, K. Arisaka, F. Arneodo, A. Askin, L. Baudis, A. Behrens, E. Brown, J. M. R. Cardoso, B. Choi, D. Cline, S. Fattori, A. D. Ferella, K. L. Giboni, A. Kish, C. W. Lam, R. F. Lang, K. E. Lim et al, "The XENON100 dark matter experiment," *Astroparticle Physics*, vol. 35, no. 9, pp. 573 - 590, April 2012.

[74] A. Breskin, "CsI UV photocathodes: history and mystery," *Nuclear Instruments and Methods in Physics Research Section A*, vol. 371, no. 1 – 2, pp. 116-136, March 1996.

[75] Y. Assran, A. Sharma, "Transport Properties of operational gas mixtures used at LHC," no. arXiv:1110.6761v1, October 2011.

[76] LUX Collaboration: D.S. Akerib, H.M. Araujo, X. Bai, A.J. Bailey, J. Balajthy, S. Bedikian, E. Bernard, A. Bernstein, A. Bolozdynya, A. Bradley, D. Byram, S.B. Cahn, M.C. Carmona-Benitez, C. Chan, J.J. Chapman, A.A. Chiller, C. Chiller, K. Clark et al, "First results from the LUX dark matter experiment at the Sanford Underground Research Facility," *Physical Review Letters*, vol. 112, no. 9, March 2014.

[77] A. Kish for the XENON and DARWIN consortium Collaborations, "Direct Dark Matter Detection with the XENON and DARWIN experiments," in *Proceedings of the 3rd International Conference on Technology and Instrumentation in Particle Physics (TIPP 2014)*, Amsterdam, Netherlands, 2014.

[78] L. Baudis (for the DARWIN consortium), "DARWIN dark matter WIMP search with noble liquids," in *Proceedings of the 12th International Conference on Topics in Astroparticle and Undergroung Physics*, vol. 375, Munich, Germany, 2011.

[79] L. Baudis, DARWIN: project overview, 2013, 6th DARWIN meeting, Naples, December, 2013.

[80] Peter F. Sorensen, A Position-Sensitive Liquid Xenon Time-Projection Chamber for Direct Detection of Dark Matter: The XENON10 Experiment, 2008, Ph.D. Thesis.

[81] V. Peskov E. Nappi, *Imaging gaseous detectors and their applications*, 1st ed.: Wiley-VCH, 2013.

[82] D. B. Carr, R. J. Littlefield, W. L. Nicholson, J. S. Littlefield, "Scatterplot Matrix Techniques for Large N," *Journal of the American Statistical Association*, vol. 82, no. 398, pp. 424 - 436, June 1987.

[83] G. Cervelli, M. French, J. Fulcher, G. Hall, L. Jones, L.K. Lim, G. Marseguerra, P. Moreira, Q. Morrissey, A. Neviani, E. Noah M. Raymond, "The CMS tracker APV25 0.25-mu-m CMOS readout chip," in *Proceedings of the Nuclear Science Symposium Conference Record*, Lyon, France, 2000, pp. 130 - 134.

[84] S. Martoiu, H. Muller, A. Tarazona, J. Toledo, "Development of the scalable readout system for micro-pattern gas detectors and other applications," in *Proceedings of the Topical Workshop on Electronics for Particle Physics 2012*, Oxford, United Kingdom, March 2013, p. C03015.

[85] M. J. French, L. L. Jones, Q. Morrissey, A. Neviani, R. Turchetta, J. Fulcher, G. Hall, E. Noah, M. Raymond, G. Cervelli, P. Moreira, G. Marseguerra, "Design and results from the APV25, a deep sub-micron CMOS front-end chip for the CMS tracker," in *Proceedings of the 4th International Symposium on Development and Conference*, Hiroshima, Japan, 2001, pp. 359 - 365.

[86] J.A. Mir, R. Stephenson, N.J. Rhodes, E.M. Schooneveld, J.F.C.A. Veloso, J.M.F.

Dos Santos, "Short induction gap gas electron multiplier (GEM) for X-ray spectroscopy," *Nuclear Instruments and Methods in Physics Research A*, no. 573, pp. 179 - 182, November 2007.

[87] J.A. Mir, R. Stephenson, N.J. Rhodes, E.M. Schooneveld, H. Natal da Luz, J.F.C.A. Veloso, J.M.F. Dos Santos, C.D.R. Azevedo, "Further studies on the gain properties of a Gas Electron Multiplier with a Micro-Induction Gap Amplifying Structure (GEM-MIGAS) aimed at low-energy X-ray detection," *Nuclear Instruments and Methods in Physics Research A* , no. 580, pp. 1372 - 1377, 2007.

[88] A.S. Conceição, J.M. Maia, J.A. Mir, L.M.P. Fernandes, J.M.F. dos Santos, "GEM-MIGAS electron multiplier operation in Argon-Methane mixtures," *IEEE Transactions on Nuclear Science*, vol. 56, no. 5, pp. 2874 - 2879, October 2009.

[89] ANSYS simulation software. [Online]. www.ansys.com

[90] Pitt, M., Private communication, Weizmann Institute of Science.

[91] A. S. Conceicão, J. M. Maia, J. A. Mir, L. M. P. Fernandes, J. M. F. dos Santos, "GEM-MIGAS Electron Multiplier Operation in Argon-Methane Mixtures," *IEEE Transactions on Nuclear Science*, vol. 56, no. 5, pp. 2874 - 2879, October 2009.

[92] A. Breskin, R. Alon, M. Cortesi, R. Chechik, J. Miyamoto, V. Dangendorf, J. Maia, J. M. F. Dos Santos, "A concise review on THGEM detectors," *Nuclear Instruments and Methods in Physics Research Section A*, vol. 598, no. 1, pp. 107 - 111, 2009.

[93] L. Arazi, A. Breskin, R. Chechik, M. Cortesi, M. Pitt, A. Rubin, H. Natal da Luz, J. M. F. dos Santos, C. D. R. Azevedo, D. S. Covita, C. A. B. Oliveira, J. F. C. A. Veloso, M. Breidenbach, D. Freytag, G. Haller, R. Herbst, S. Park, A. White, J. Yu et al, "THGEM-based detectors for sampling elements in DHCAL: laboratory and

beam evaluation," in *Proceedings of the 2nd International Conference on Micro-pattern gaseous detectors (MPGD 2011) - JINST 7 C05011*, Kobe, Japan, 2012.

[94] M. Cortesi, V. Peskov, G. Bartesaghi, J. Miyamoto, S. Cohen, R. Chechik, J.M. Maia, J. M. F. dos Santos, G. Gambarini, V. Dangendorf, A. Breskin, "THGEM operation in Ne and Ne/CH4," *Journal of Instrumentation*, vol. 8, no. 8, p. 08001, 2009.

[95] A. Breskin, M. Cortesi, R. Alon, J. Miyamoto, V. Peskov, G. Bartesaghi, R. Chechik, V. Dangendorf, J. M. Maia, J. M. F. dos Santos, "The THGEM: A thick robust gaseous electron multiplier for radiation detectors," in *Proceedings of the 1st International Conference on Technology and Instrumentation in Particle Physics*, Tsukuba, Japan, 2010, pp. 132 - 134.

[96] M. Alexeev, R. Birsa, F. Bradamante, A. Bressan, M. Chiosso, P. Ciliberti, G. Croci, M.L. Colantoni, S. Dalla Torre, S. Duarte Pinto, O. Denisov, V. Diaz, A. Ferrero, M. Finger, M. Finger Jr., H. Fischer, G. Giacomini, M. Giorgi, B. Gobbo et al, "THGEM based photon detector for Cherenkov imaging applications," in *Proceedings of the 11th Pisa Meeting on Advanced Detectors*, La Biodola, Isola d'Elba, Italy, 2010, pp. 396 – 397.

[97] IST-Lisbon and Bordage database - retrieved on September 7, 2014. [Online]. www.lxcat.net

[98] F. J. Norton, "Helium diffusion through glass," *Journal of the American Ceramic Society*, vol. 36, no. 3, pp. 90 - 96, March 1953.

[99] D. S. Leonard, P. Grinberg, P. Weber, E. Baussan, Z. Djurcic, G. Keefer, A. Piepke, A. Pocar, J.-L. Vuilleumier, J.-M. Vuilleumier, D. Akimov, A. Bellerive, M. Bowcock, M. Breidenbach, A. Burenkov, R. Conley, W. Craddock, M.

Danilov, R. DeVoe et al, "Systematic study of trace radioactive impurities in candidate construction materials for EXO-200," *Nuclear Instruments and Methods in Physics Research Section A*, vol. 591, no. 3, pp. 490 - 509, July 2008.

[100] XENON100 Collaboration: E. Aprile, K. Arisaka, F. Arneodo, A. Askin, L. Baudis, A. Behrens, K. Bokeloh, E. Brown, J. M. R. Cardoso, B. Choi, D. Cline, S. Fattori, A. D. Ferella, K. L. Giboni, A. Kish, C. W. Lam, J. Lamblin, R. F. Lang, K. E. Lim et al, "Material screening and selection for XENON100," *Astroparticle Physics*, vol. 35, no. 2, pp. 43 - 19, March 2011.

[101] V. Alvarez, I. Bandac, A. Bettini, F. I. G. M. Borges, S. Carcel, J. Castel, S. Cebrian, A. Cervera, C. A. N. Conde, T. Dafni, T. H. V. T. Dias, J. Diaz, M. Egorov, R. Esteve, P. Evtoukhovitch, L. M. P. Fernandes, P. Ferrario, A. L. Ferreira et al, "Radiopurity control in the NEXT-100 double beta decay experiment: procedures and initial measurements," *Journal of Instrumentation*, vol. 8, no. T01002, January 2013.

[102] S. Cebrián, T. Dafni, E. Ferrer-Ribas, J. Galán, I. Giomataris, H. Gómez, F.J. Iguaz, I.G. Irastorza, G. Luzón, R. de Oliveira, A. Rodríguez, L. Seguí, A. Tomás, J. A. Villar, "Radiopurity of Micromegas readout planes," *Astroparticle Physics*, vol. 34, no. 6, pp. 354 - 359, January 2011.

[103] A. Breskin, I. Israelashvili, M. Cortesi, L. Arazi, S. Shchemelinin, R. Chechik, V. Dangendorf, B. Bromberger, D. Vartsky, "A novel liquid-Xenon detector concept for combined fast-neutrons and gamma imaging and spectroscopy," *Journal of Instrumentation*, vol. 7, no. C06008, June 2012.

[104] I. Israelashvili, M. Cortesi, D. Vartsky, L. Arazi, D. Bar, E. N. Caspi, A. Breskin, "A Comprehensive Simulation Study of a Liquid-Xe Detector for Contraband

Detection," *Journal of Instrumentation*, vol. 10, no. P03030, December 2015.

[105] A. Breskin, "Liquid Hole-Multipliers: A potential concept for large single-phase noble-liquid TPCs of rare events," in *Proceedings of the 6th Symposium on Large TPCs for Low Energy Rare Event Detection*, Paris, France, 2013.

[106] L. Arazi, E. Erdal, A. E. C. Coimbra, M. L. Rappaport, D. Vartsky, V. Chepel, A. Breskin, "Liquid Hole Multipliers: bubble-assisted electroluminescence in liquid xenon," *Journal of Instrumentation*, vol. 10, no. 8, p. P08015, May 2015.